

Universiteit
Leiden
The Netherlands

Temperature and pressure effects on the electrochemical CO2 reduction

Vos, R.E.

Citation
Vos, R. E. (2025, February 5). *Temperature and pressure effects on the electrochemical CO2 reduction*. Retrieved from https://hdl.handle.net/1887/4179004

Version:	Publisher's Version
License:	Licence agreement concerning inclusion of doctoral thesis in the Institutional Repository of the University of Leiden
Downloaded from:	https://hdl.handle.net/1887/4179004

Note: To cite this publication please use the final published version (if applicable).

A

Supporting Information to Chapter 2

The effect of temperature on the cation-promoted electrochemical CO_2 reduction on gold

A.1 Standard equilibrium potential

The standard equilibrium potential of CO_2 reduction towards CO has a temperature dependence itself. Using equations A.1a and A.1b, and the thermodynamic data tabulated in Table A.1, we can calculate the equilibrium potential at different temperatures. Table A.2 shows that the equilibrium potential shifts towards more negative potentials with increasing temperature, although the shift is relatively small.

$$\Delta G = -nFE \qquad (A.1a)$$

$$\Delta G = \Delta H - T\Delta S \qquad (A.1b)$$

$$CO_2 + 2\,e^- + 2H^+ \rightarrow CO + H_2O \qquad (A.2a)$$

$$H_2 \rightarrow 2\,e^- + 2H^+ \qquad (A.2b)$$

Table A.1 The tabulated enthalpies and entropies for species involved in the CO2 reduction towards CO

	ΔH (kJ/mol)	ΔS (J/mol)
CO2	-393.509	213.74
CO	-110.525	197.674
H2O	-285.8	69.9
H2	0	130.7

Assuming the entropy and enthalpy are constants in this temperature range, the standard equilibrium potentials can be obtained at different temperatures as seen in Table A.2.

Table A.2 Equilibrium potential versus RHE of CO2RR towards CO with temperature

T (°C)	$E^0(V)$
25	-0.104
30	-0.106
35	-0.108
40	-0.110
45	-0.112
50	-0.114
55	-0.116
60	-0.118
65	-0.120

A.2 Exchange current density determination

Figure A.1 is an example of a Tafel plot used to determine the exchange current density by extrapolation.

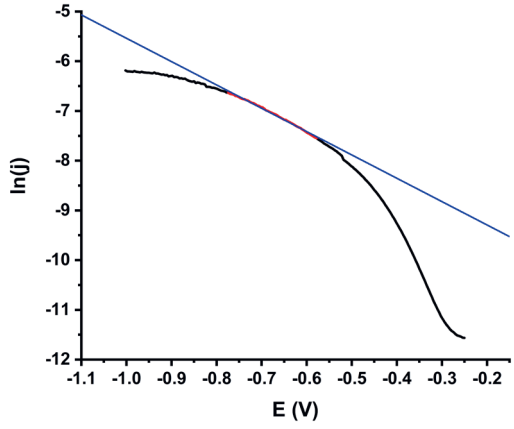


Figure A.1 Determination of the exchange current density using an extrapolation in the Tafel plot of the partial current density for CO formation

A.3 Plateau in activity of CO formation

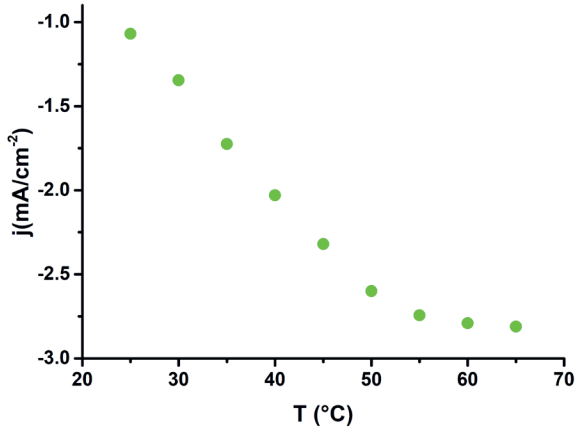


Figure A.2 The partial current density of CO2RR towards CO formation at -0.7V vs RHE plotted against temperature in 0.1M $NaHCO_3$ to illustrate the plateau in the activity starting around 55 ^{0}C.

A.4 SHE scale

When pH dependent studies have been performed on CO2RR, it has been argued before that the partial current densities of CO should be plotted on an SHE scale as this reaction is pH independent [1,2]. Because in our experiments the RHE and the SHE scale are not exactly similar, we have plotted our data on a SHE scale as well (Figure A.3). This shows that there is no qualitative difference between the SHE and RHE scale in the temperature range used in this study. Moreover, for the quantitative data obtained in the kinetic analysis later in this study, the differences are minor. So, we decided to show our data on a RHE scale in this study as this was the reference scale used to measure and requires no further operations.

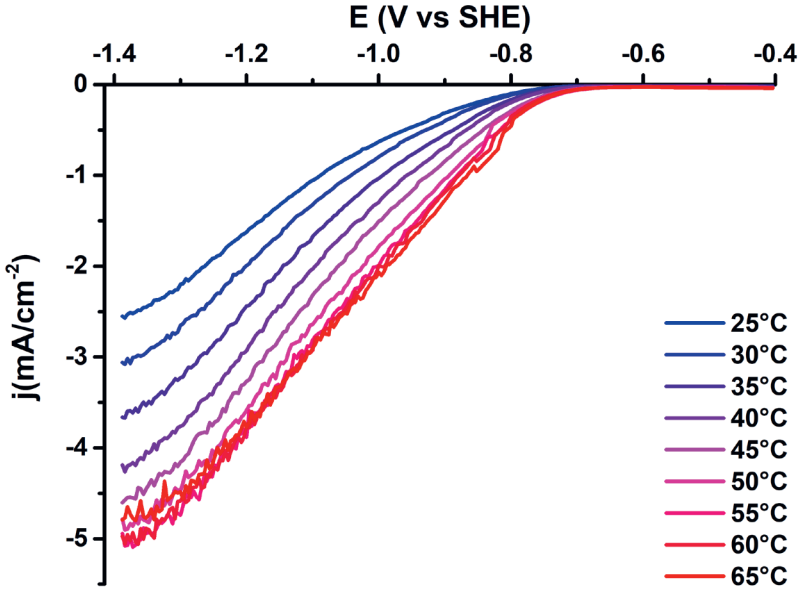


Figure A.3 The partial current density for CO formation in 0.1M $NaHCO_3$ on a gold RRDE at 2500 rpm and 20 mV/s at different temperatures plotted on a SHE scale

A.5 Temperature dependent variables

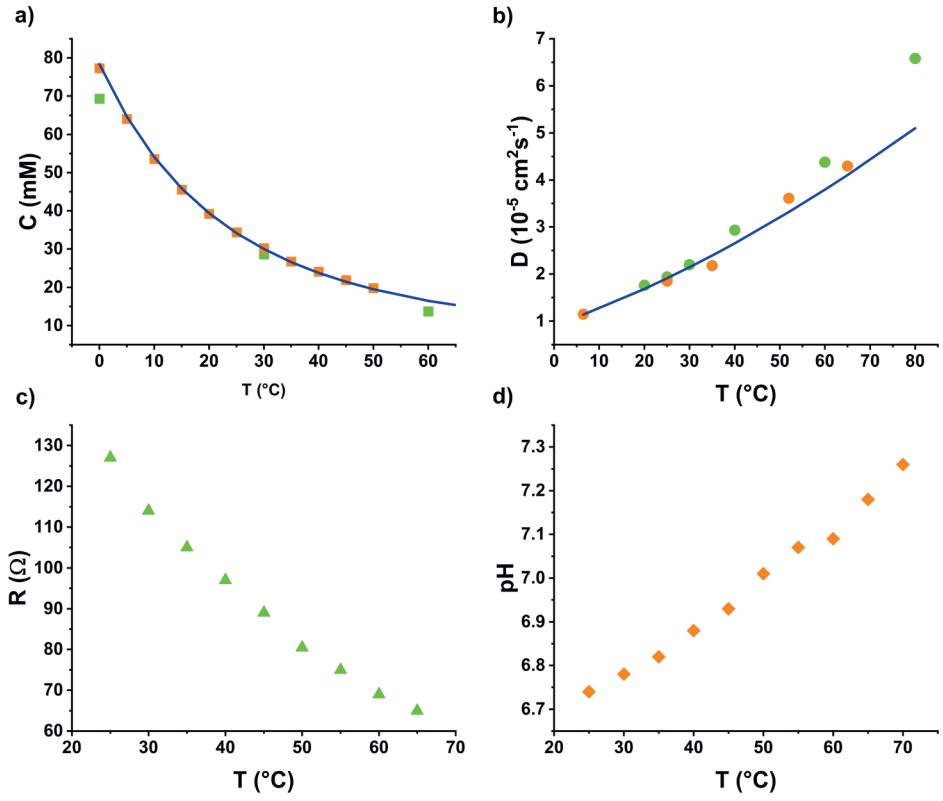


Figure A.4 Different parameters which change with temperature, (some values originate from literature); a) the CO_2 concentration in water (orange[3], green[4], blue[5]), b) the diffusion coefficient of CO_2 in water (orange[6], green[7], blue[8]), c) the resistance of 0.1M $NaHCO_3$, d) the pH of 0.1M CO2 saturated $NaHCO_3$

A.6 Partial pressure experiments

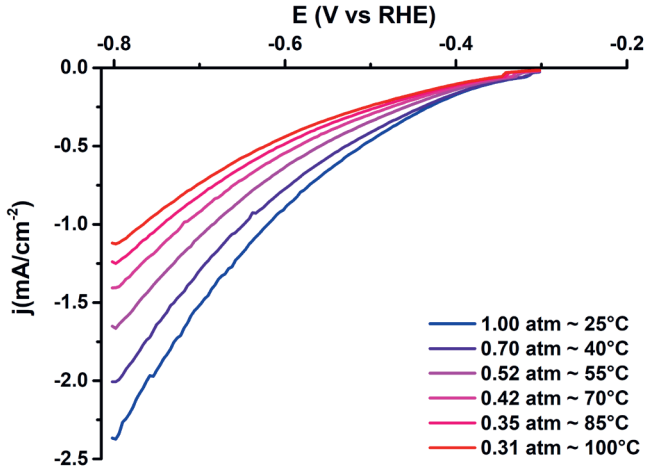


Figure A.5 The partial current density for CO formation at different partial pressures of CO_2 (and the equivalent temperature with 1 atm of CO_2) on a gold RRDE at 2500 rpm and 20 mV/s in 0.1 M $NaHCO_3$.

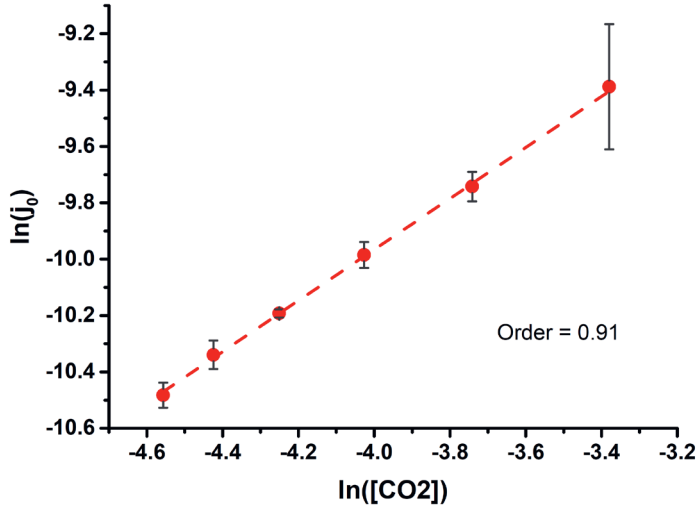


Figure A.6 The ln of the exchange current density at different concentrations of CO_2 to determine the reaction order of CO_2

A.7 Limiting current densities and Koutecky Levich plot

Levich equation

$$j_L = 0.201nFD^{\frac{2}{3}}\omega^{\frac{1}{2}}\upsilon^{-\frac{1}{6}}C = B_L\omega^{\frac{1}{2}} \qquad (A.3)$$

Koutecky-Levich equation

$$\frac{1}{j_m} = \frac{1}{j_K} + \frac{1}{j_{MT}} = \frac{1}{j_K} + \frac{1}{B_L\omega^{0.5}} \qquad (A.4)$$

where j_L is the Levich current, n moles of electrons transferred, D is the diffusion coefficient, ω the angular rotation rate in rpm, υ the kinematic viscosity, C the concentration of the CO_2, B_L the Levich constant, j_m the measured partial current density j_K the kinetic current density and j_{MT} the mass transport current density

Table A.3 The limiting current densities at different temperatures and 2500 rpm calculated using the Levich equation [5,8]

J (mA/cm²)	T (K)	D (cm²/s)	v (cm²/s)	C (mmol/ml)
103.98	298.12	1.92E-05	8.90E-03	0.034
100.41	303.15	2.16E-05	8.00E-03	0.030
97.34	308.15	2.40E-05	7.24E-03	0.027
94.68	313.15	2.66E-05	6.60E-03	0.024
92.49	318.15	2.93E-05	6.03E-03	0.021
90.77	323.15	3.21E-05	5.50E-03	0.019
89.19	328.15	3.50E-05	5.11E-03	0.018
88.13	333.15	3.80E-05	4.70E-03	0.016
87.12	338.15	4.11E-05	4.41E-03	0.015

Table A.4 Kinetic current density and Levich constant from data of Figure A.4

T (K)	j_K (mA)	1/B ((s*rpm)$^{0.5}$/C)
298	1.9	3317
313	4.9	4354
328	10.6	5677

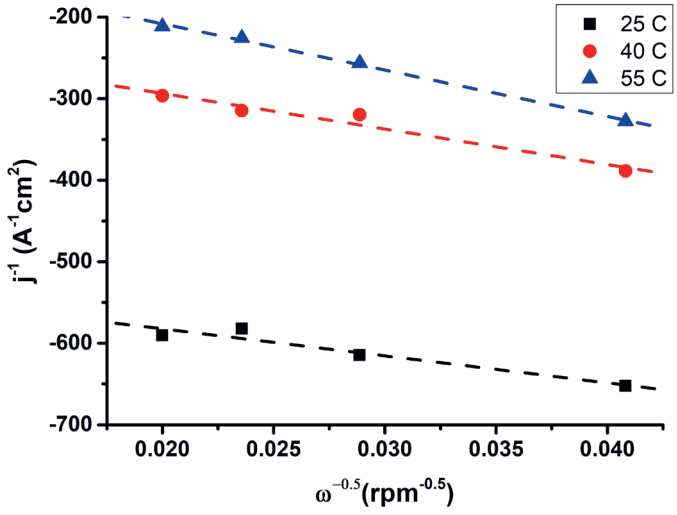


Figure A.7 Koutecky-Levich plot of CO2RR towards CO at -0.8V vs RHE

A.8 Hydrogen evolution reaction with increasing temperature

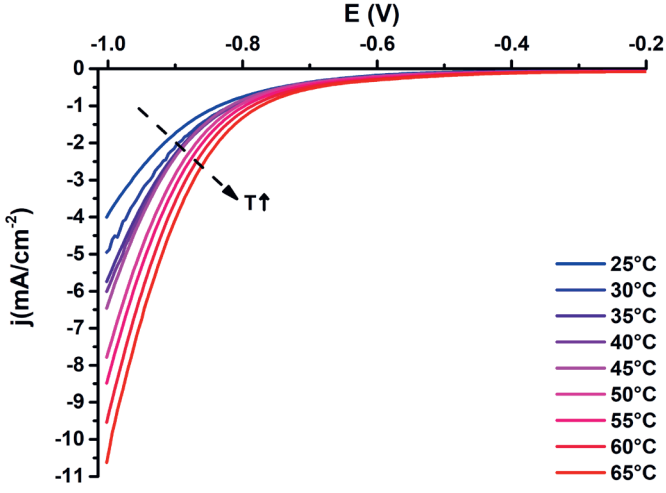


Figure A.8 The current density of HER in 0.1M Ar saturated $NaHCO_3$ on a gold RRDE at 2500 rpm and 20 mV/s

A.9 Qualitative effect of temperature on CO formation rates

Table A.5 The ratios between the partial current densities towards CO at different temperatures compared to the partial current density at 25 ^{0}C



	30 °C	35 °C	40 °C	45 °C	50 °C	55 °C	60 °C	65 °C
-0.4 V	1.18	1.71	1.97	3.36	3.44	3.89	3.16	3.34
-0.5 V	1.33	1.80	2.15	2.72	3.35	3.46	3.55	3.65
-0.6 V	1.24	1.64	1.99	2.35	2.77	2.92	3.11	3.06
-0.7 V	1.29	1.70	1.96	2.26	2.56	2.63	2.66	2.71
-0.8 V	1.26	1.56	1.82	2.06	2.22	2.32	2.24	2.26
-0.9 V	1.23	1.49	1.69	1.88	1.96	1.97	2.01	1.95
-1.0 V	1.23	1.48	1.65	1.81	1.86	1.95	1.95	1.82



A.10 Apparent activation energies

The Arrhenius equation can be used to determine the apparent activation energy.

$$k = Ae^{\frac{-E_a}{RT}} \qquad (A.5)$$

where k is the reaction rate constant, A is the pre-exponential factor, E_a is the activation energy, R is the gas constant and T the absolute temperature. Since the exchange current density depends on the reaction rate constant, the j_0 will also follow an Arrhenius relation. We can substitute equation A.6 in equation A.5 to get equation A.7a. This equation can be rewritten to equation A.7b to obtain the apparent activation energy.

$$j_0 = nFk^0C \qquad (A.6)$$

$$j_0 = nFCAe^{\frac{-E_a}{RT}} = A'e^{\frac{-E_a}{RT}} \qquad (A.7a)$$

$$\ln(j_0) = \ln(A') - \frac{E_a}{R} * \frac{1}{T} \qquad (A.7b)$$

where j_0 is the exchange current density, F the Faraday constant, k the reaction rate constant, n the number of electrons transferred, and C the concentration of CO_2. However, we need to correct for the temperature dependence of the CO_2 concentration:

$$j_0' = j_0 \frac{C_{25°C}}{C_T} \qquad (A.8)$$

where C_{25C} is the concentration of CO_2 at 25 ^{0}C and C_T the concentration of CO_2 at the temperature of the experiment. Instead of equation A.6, equation A.8 can now be substituted in equation A.5 to get equation A.9a. This equation can be rewritten to equation A.9b. Substituting equation A.8 back in equation A.9b and equation A.9c is obtained.

$$j_0' = A' e^{\frac{-E_a}{RT}} \qquad (A.9a)$$

$$\ln(j_0') = \ln(A') - \frac{E_a}{R} * \frac{1}{T} \qquad (A.9b)$$

$$\ln(j_0) + \ln\left(\frac{C_{25°C}}{C_T}\right) = \ln(A') - \frac{E_a}{R} * \frac{1}{T} \qquad (A.9c)$$

So, to correct for the changing concentration of CO_2 with temperature, we use the correction factor $\ln\left(\frac{C_{25°C}}{C_T}\right)$.

The standard equilibrium potential changes with temperature as can be seen in Table A.2. This change has been taken into account in the Arrhenius plot of Figure 2.5. For each temperature, the exchange current density has been calculated at the corresponding standard equilibrium potential according to Table A.2.

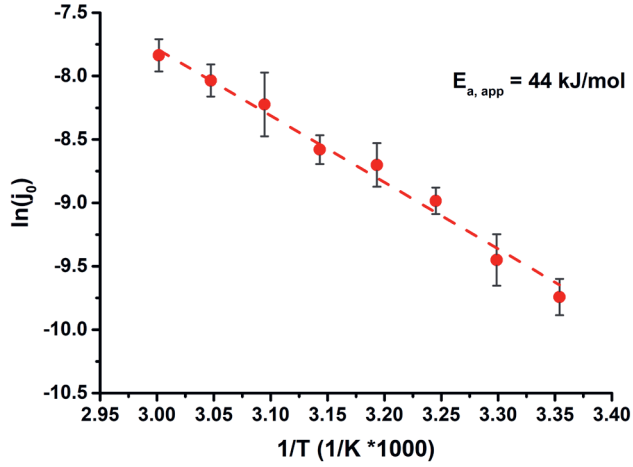


Figure A.9 Arrhenius plot of CO_2 reduction in 0.1M $NaHCO_3$ in the temperature range of 25-60 ^{0}C, not corrected for the changes in CO_2 concentration with temperature

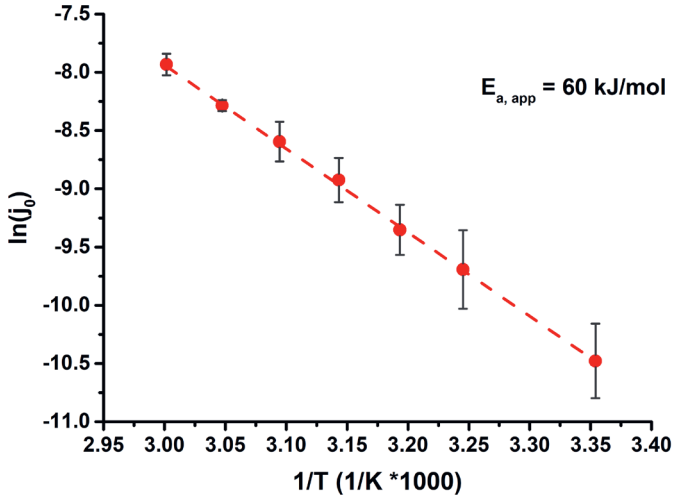


Figure A.10 Arrhenius plot of CO2RR towards CO formation in 0.1M $NaHCO_3$ using data from Figure 2.2, so at constant CO_2 concentration

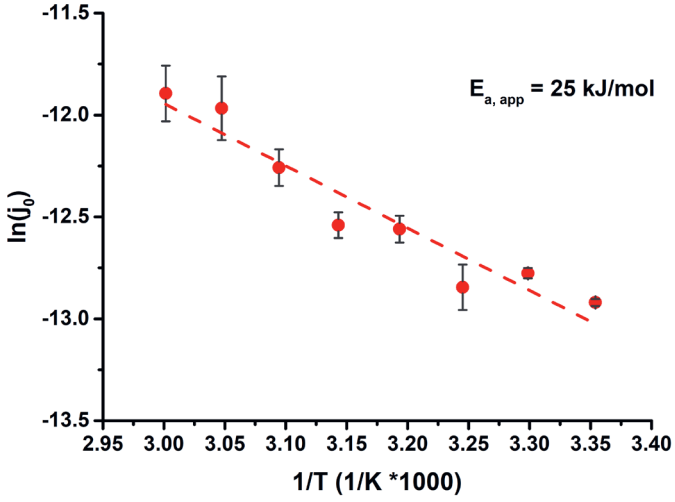


Figure A.11 Arrhenius plot of HER in Ar saturated 0.1M $NaHCO_3$

A.11 Transfer coefficient

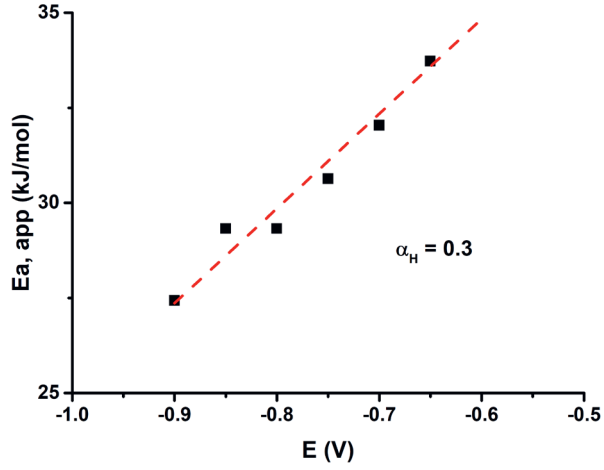


Figure A.12 The apparent activation energy of CO2 reduction towards CO formation in 0.5M NaHCO3 plotted against the applied potential

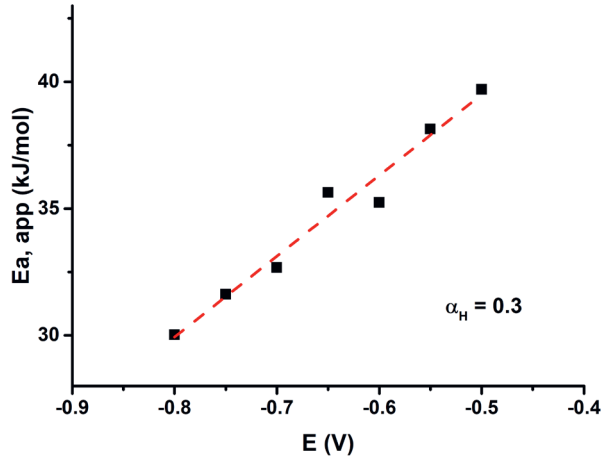


Figure A.12 The apparent activation energy of CO2 reduction towards CO formation in 0.1M CsHCO3 plotted against the applied potential

The entropic contribution to the transfer coefficient can be determined from the slope of the ln of the pre-exponential factors with potential [9].

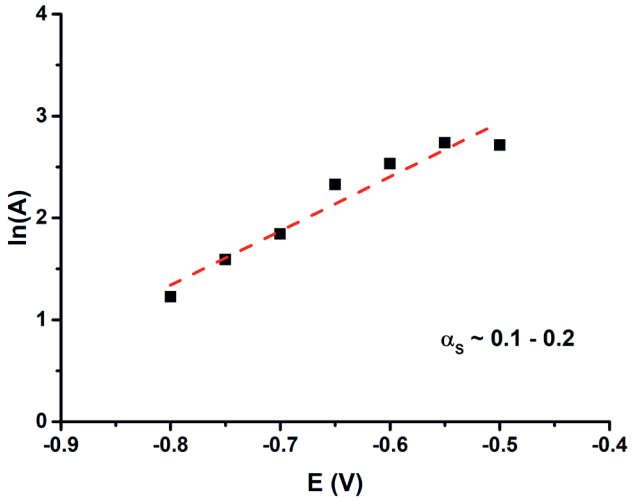


Figure A.14 The ln of the pre-exponential factor plotted against the applied potential for CO_2 reduction towards CO in 0.1M $NaHCO_3$

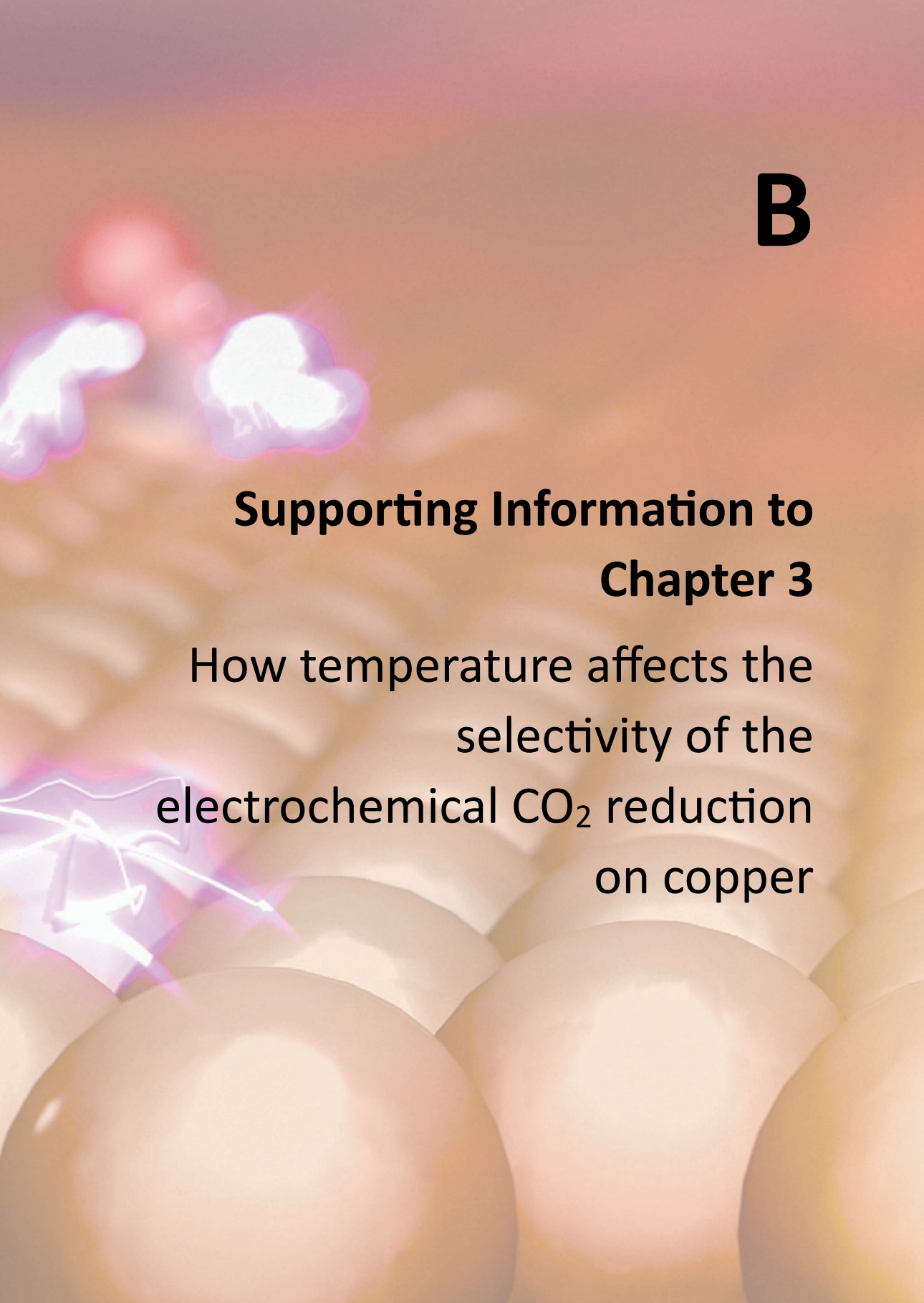
A.12 Cation volume occupation

Assuming 1.5M of K^+ at the surface [10], and an effective interfacial cation radius of 4.5 for K^+ [11], the volume these cations occupy is percent:

$$\left(1.5 * 6.022E23 * \frac{4}{3}\ \pi\ (6E-10)^3\ \right) / 10^{-3}\ * 100\% \ = 34\%$$

References

1. Resasco, J., Lum, Y., Clark, E., Zeledon, J. Z. & Bell, A. T. *ChemElectroChem* **5**, 1064–1072 (2018).
2. Ringe, S. *et al. Nature Communications* **11**, (2020).
3. Harned, H. S. & Davis Jr, R. *Journal of the American Chemical Society* **65**, 2030–2037 (1943).
4. Duan, Z. & Sun, R. *Chemical Geology* **193**, 257–271 (2003).
5. Plummer, L. N. & Busenberg, E. *Geochimica et Cosmochimica Acta* **46**, 1011–1040 (1982).
6. Unver, A. A. & Himmelblau, D. M. *Journal of Chemical and Engineering Data* **9**, 428–431 (1964).
7. Tamimi, A., Rinker, E. B. & Sandall, O. C. *Journal of Chemical and Engineering Data* **39**, 330–332 (1994).
8. Lu, W., Guo, H., Chou, I. M., Burruss, R. C. & Li, L. *Geochimica et Cosmochimica Acta* **115**, 183–204 (2013).
9. Gojković, S. L., Zečević, S. K. & Dražić, D. M. *Journal of Electroanalytical Chemistry* **399**, 127–133 (1995).
10. Weitzner, S. E. *et al. Journal of Physical Chemistry Letters* **11**, 4113–4118 (2020).
11. Ringe, S. *et al. Energy & Environmental Science* 17–25 (2019) doi:10.1039/c9ee01341e.



B

Supporting Information to Chapter 3

How temperature affects the selectivity of the electrochemical CO_2 reduction on copper

B.1 Photo and scheme of the H-cell and jacket

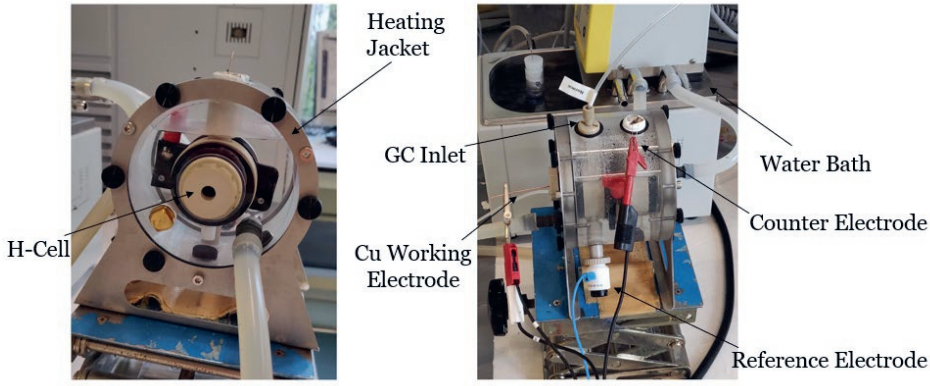


Figure B.1 Photos from the H-cell surrounded by the water jacket used to control the temperature

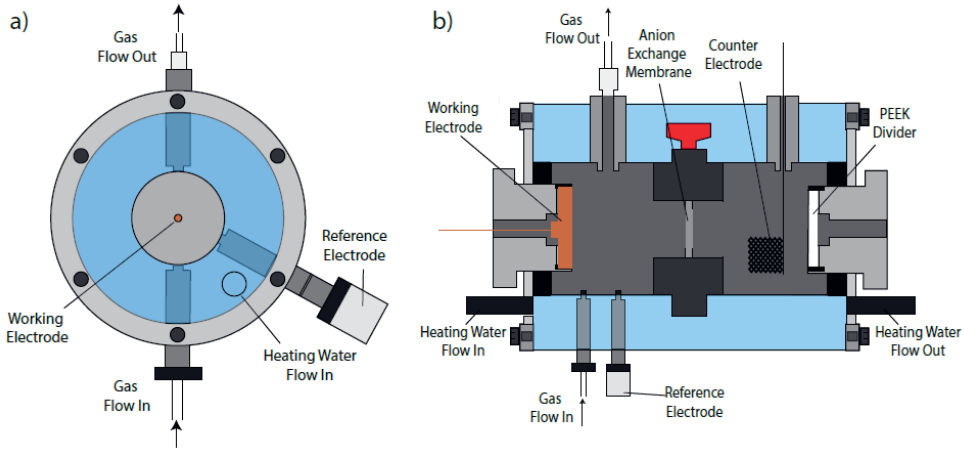


Figure B.2 Schematics of the H-cell surrounded by the water jacket used to control the temperature. a) Frontal-section of the cathodic chamber and (b) cross-section of the electrochemical H-cell with heating jacket

B.2 CO_2 reduction selectivity and activity at -1.1V vs. RHE

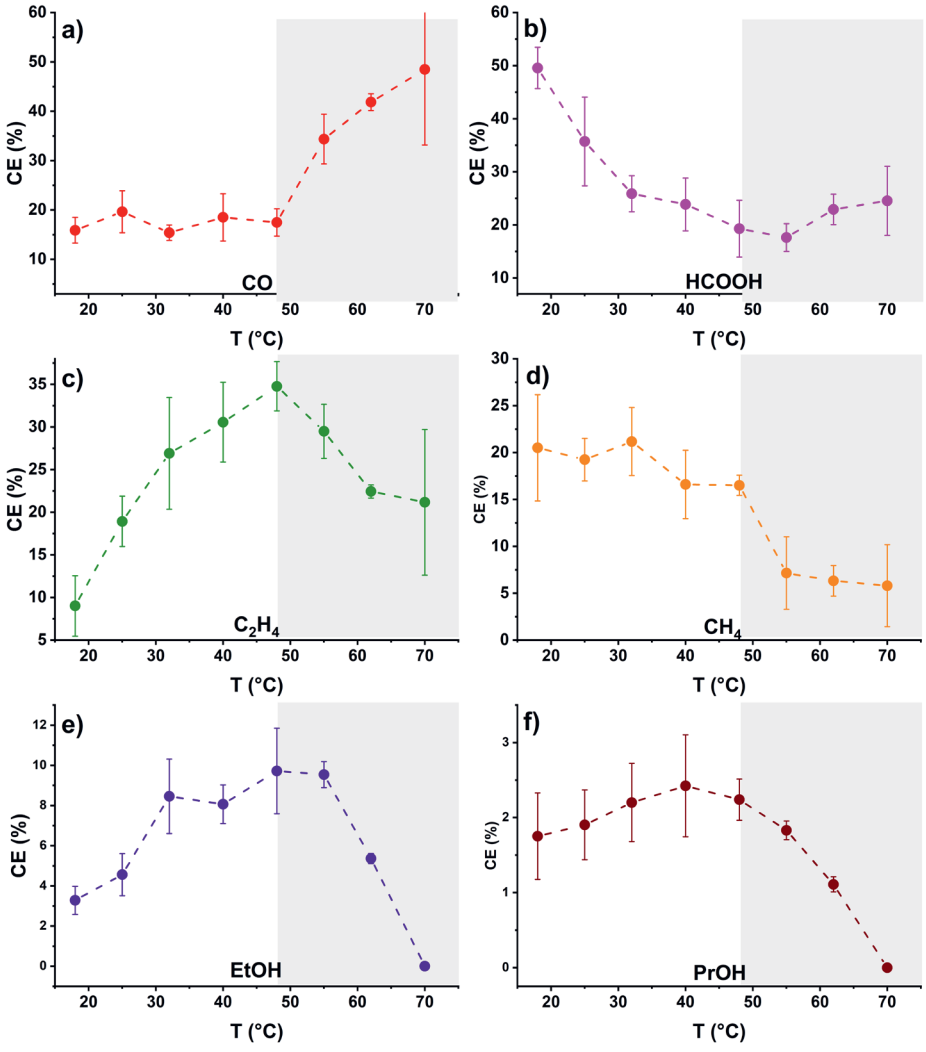


Figure B.3 Carbon Efficiency of CO2RR at different reaction temperatures in 0.1 M KHCO3 at -1.1 V vs. RHE for a) CO b) formic acid c) ethylene d) methane e) ethanol, and f) 1-propanol. The error bars are determined from at least 3 separate experiments. The gray background indicates the second regime and the dotted lines are a guide to the eye.

Table B.1 Faradaic and Carbon efficiency for CO2RR at different temperatures at -1.1V vs. RHE

-1.1 V	FE/CE (%)							
	18 °C	25 °C	32 °C	40 °C	48 °C	55 °C	62 °C	70 °C
H_2	29.4 / -	27 / -	28.7 / -	29.3 / -	41.0 / -	48.7 / -	62.3 / -	84.0 / -
CO	4.7 / 15.9	6.4 / 19.6	5.3 / 15.4	5.9 / 18.5	4.5 / 17.5	7.7 / 34.4	5.9 / 41.9	1.9 / 48.5
CH_4	21.5 / 20.5	17.9 / 19.3	20.1 / 21.2	18.1 / 16.6	13.5 / 16.5	6.6 / 7.2	4.2 / 6.3	1.2 / 5.8
C_2H	5.9 / 9.0	13.5 / 18.9	18.8 / 26.9	21.1 / 30.6	21.9 / 34.8	16.6 / 29.5	9.9 / 22.4	2.2 / 21.2
HCOOH	13.3 / 49.6	11.3 / 35.7	9.9 / 25.9	6.5 / 23.9	4.7 / 19.3	3.5 / 17.6	3.7 / 22.9	1.2 / 24.5
EtOH	2.6 / 3.3	4.1 / 4.6	6.4 / 8.5	7.2 / 8.1	6.9 / 9.7	4.4 / 9.5	2.6 / 5.4	0.6 / 0.1
PrOH	1.4 / 1.8	1.8 / 1.9	1.7 / 2.2	2.1 / 2.4	1.6 / 2.2	0.9 / 1.8	0.5 / 1.1	0.0 / 0.0

B.3 CO_2 reduction selectivity and activity at -0.95V vs. RHE

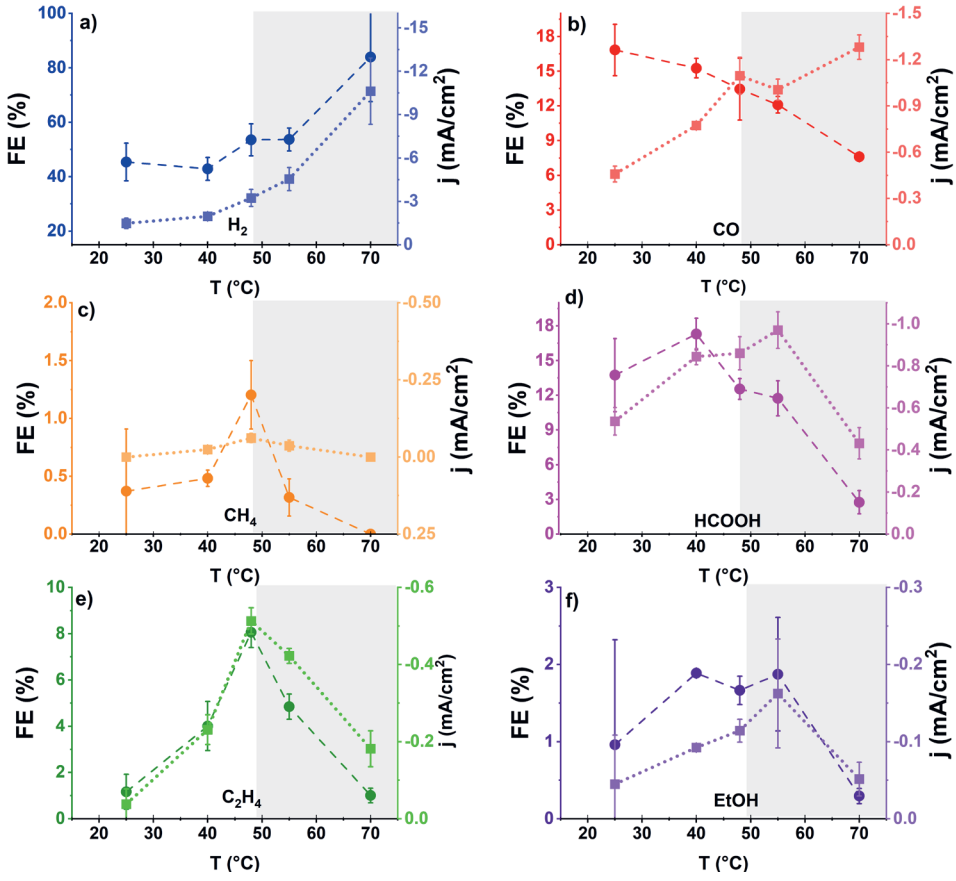


Figure B.4 Faradaic efficiency (in dark circles) and partial current density (in light squares) of CO2RR at different temperatures in 0.1M $KHCO_3$ at -0.95V vs. RHE for a) hydrogen b) CO c) methane d) formic acid e) ethylene f) ethanol g) 1-propanol. Dotted lines are a guide to the eye and error bars are determined from at least 3 measurements.

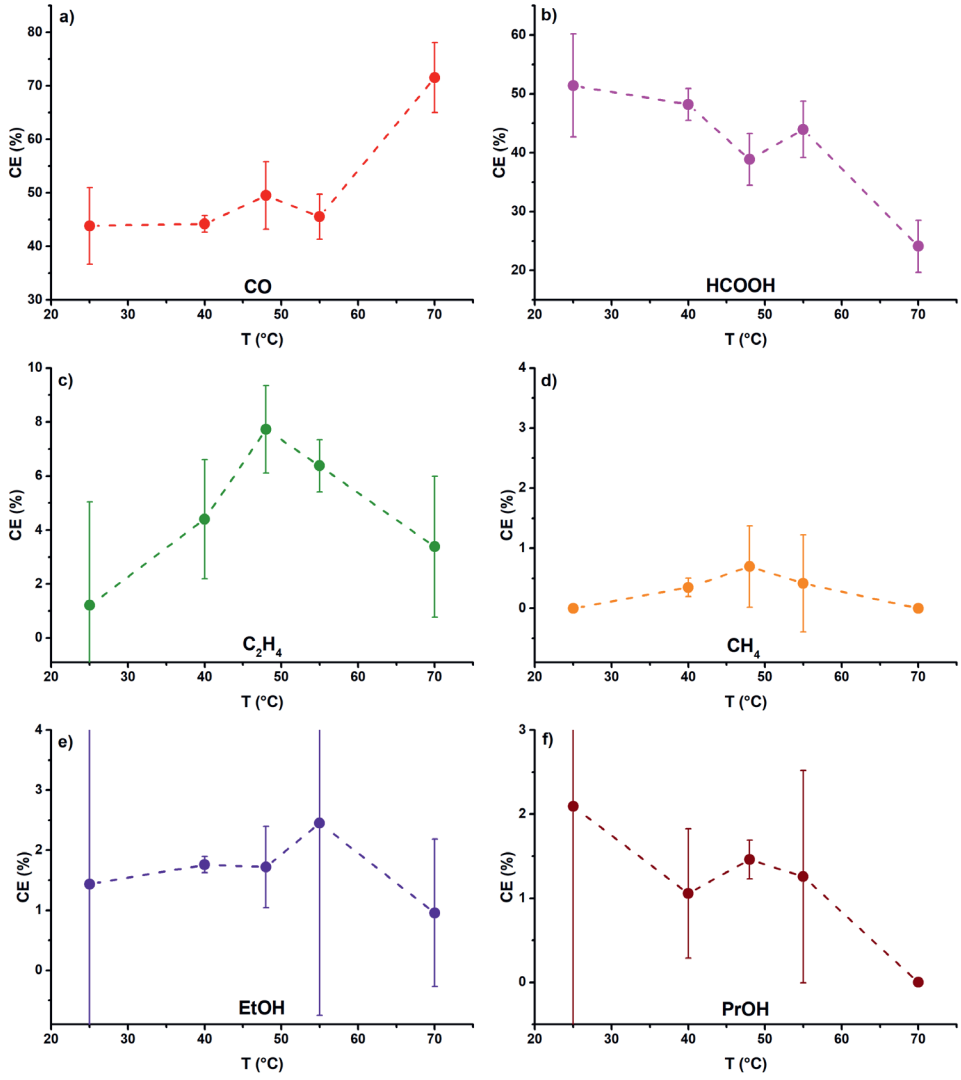


Figure B.5 Carbon efficiency of CO2RR at different temperatures in 0.1 M $KHCO_3$ at -0.95 V vs. RHE for a) formic acid b) CO c) ethylene d) methane e) ethanol f) 1-propanol. Dotted lines are a guide to the eye and error bars are determined from at least 3 measurements.

Table B.2 Faradaic and Carbon efficiency for CO2RR at different temperatures at -0.95V vs. RHE

-0.95 V	FE/CE (%)				
	25 °C	40 °C	48 °C	55 °C	70 °C
H_2	45.4 / -	42.9 / -	53.5 / -	53.7 / -	83.9 / -
CO	16.8 / 43.8	15.3 / 44.2	13.5 / 49.5	12.1 / 45.5	7.6 / 71.6
CH_4	0.4 / 0.1	0.5 / 0.3	1.2 / 0.7	0.3 / 0.4	0.0 / 0.0
C_2H	1.2 / 1.2	4.0 / 4.4	8.1 / 7.7	4.8 / 6.4	1.0 / 3.4
HCOOH	13.7 / 51.4	17.3 / 48.2	12.5 / 38.9	11.7 / 44.0	2.8 / 24.1
EtOH	1.0 / 1.4	1.9 / 1.8	1.7 / 1.7	1.9 / 2.5	0.3 / 1.0
PrOH	1.5 / 2.1	1.1 / 1.1	1.4 / 1.5	1.0 / 1.3	0.0 / 0.0

B.4 CO_2 reduction selectivity and activity at -0.7 V vs. RHE

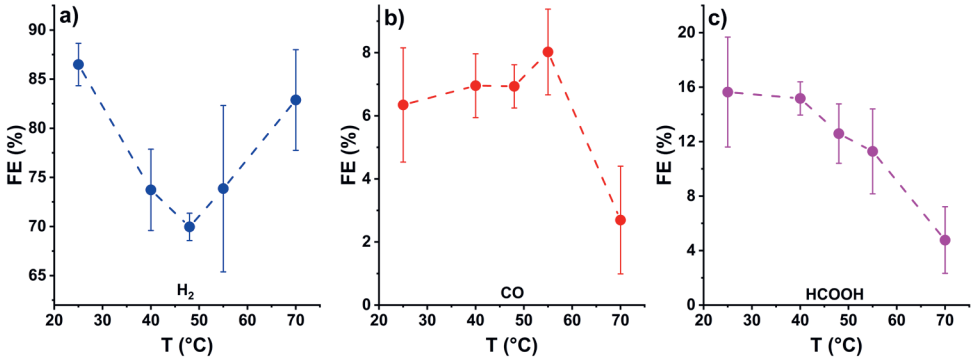


Figure B.6 Faradaic efficiency of CO2RR at different temperatures in 0.1 M $KHCO_3$ at -0.7 V vs. RHE for a) hydrogen b) CO c) formic acid

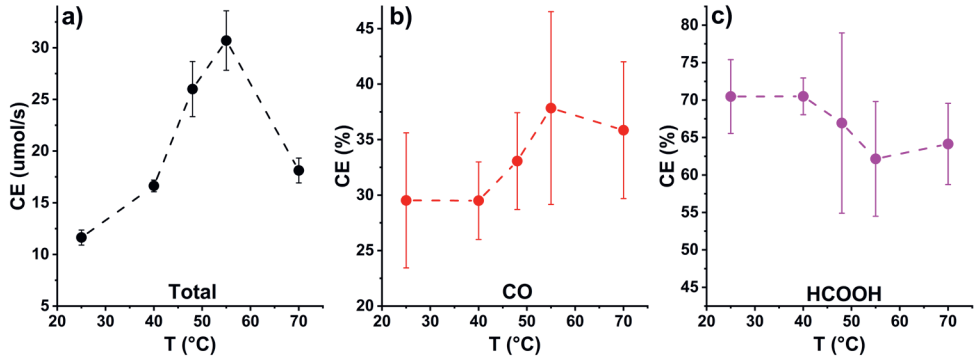


Figure B.7 a) Total consumption of CO_2 of CO2RR at different temperatures in 0.1 M $KHCO_3$ at -0.7 V vs. RHE and the carbon efficiency towards b) CO and c) HCOOH. Dotted lines are a guide to the eye and error bars are determined from at least 3 measurements.

Table B.3 Faradaic and Carbon efficiency for CO2RR at different temperatures at -0.7V vs. RHE

-0.70 V	FE/CE (%)				
	25 °C	40 °C	48 °C	55 °C	70 °C
H_2	86.5 / -	73.7 / -	70.0 / -	73.9 / -	82.9 / -
CO	6.3 / 29.5	7.0 / 29.5	6.9 / 33.1	8.0 / 37.8	2.7 / 35.9
HCOOH	15.6 / 70.5	15.2 / 70.5	12.6 / 66.9	11.3 / 62.2	4.8 / 64.1

B.5 Partial pressure experiments

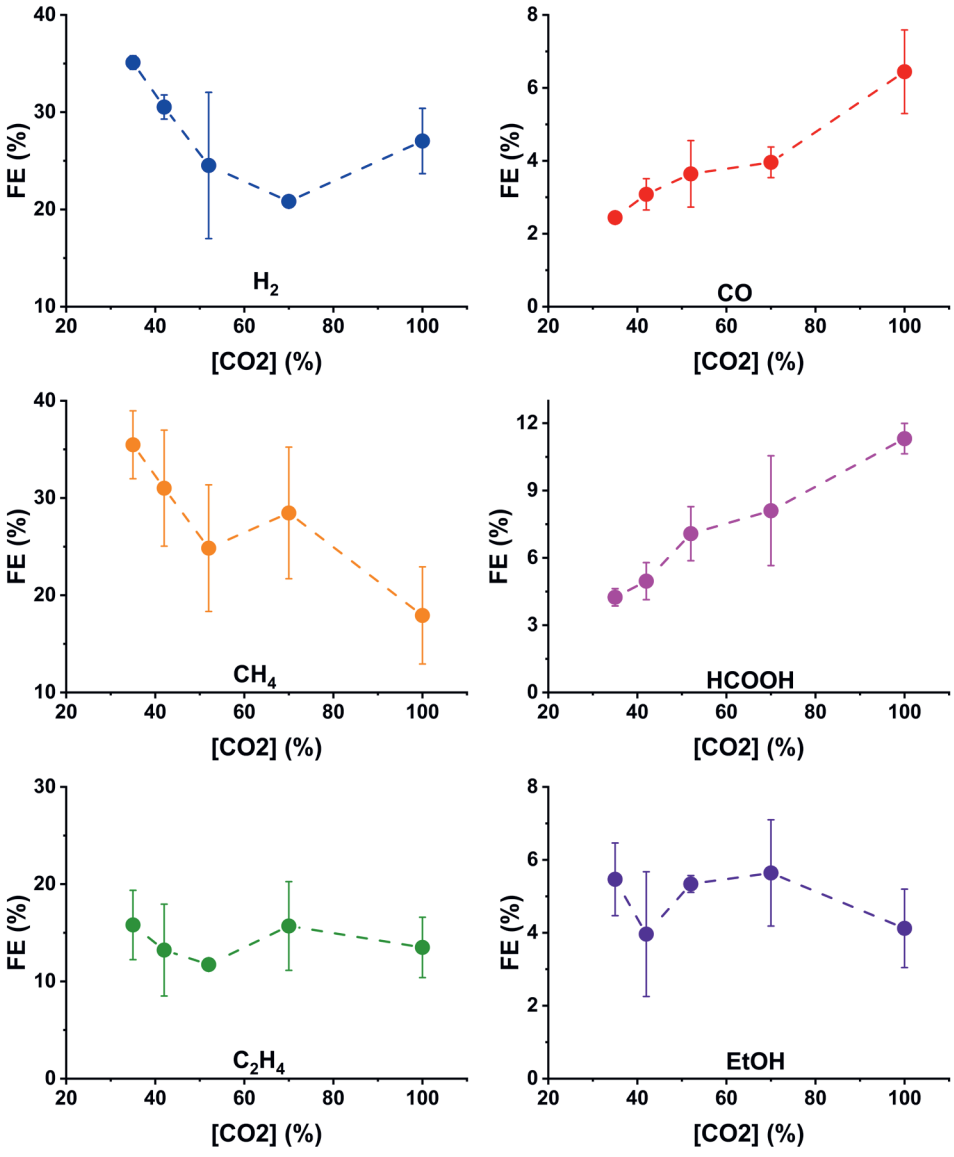


Figure B.8 Faradaic efficiency of CO2RR at different CO_2 bulk concentrations by changing the partial pressure in 0.1 M $KHCO_3$ at -1.1 V vs. RHE for a) hydrogen b) CO c) methane d) formic acid e) ethylene f) ethanol g) 1-propanol. Dotted lines are a guide to the eye and error bars are determined from at least 3 measurements.

Table B.4 Faradaic efficiency of CO2RR at different CO_2 bulk concentrations by changing the partial pressure in 0.1M $KHCO_3$ at -1.1V vs. RHE

Partial pressure	FE (%)				
[CO_2]	100 %	70 %	52 %	42 %	35 %
H_2	27.0	20.8	24.5	30.5	35.1
CO	6.4	4.0	3.6	3.1	2.4
CH_4	17.9	28.5	24.8	31.0	35.5
C_2H	13.5	15.7	11.7	13.2	15.8
HCOOH	11.3	8.1	7.1	5.0	4.2
EtOH	4.1	5.6	5.3	4.0	5.5
PrOH	1.8	1.8	1.2	1.2	1.3

Table B.5 Faradaic efficiency of CO2RR at different temperatures with constant CO_2 bulk concentrations by changing the partial pressure in 0.1M $KHCO_3$ at -1.1 V vs. RHE

[CO_2] constant	FE (%)			
	25 °C	40 °C	55 °C	70 °C
H_2	26.3	35.7	55.5	86.5
CO	3.3	4.9	5.5	1.8
CH_4	32.5	13.7	4.5	0.7
C_2H	13.7	17.0	16.6	1.7
HCOOH	6.5	5.8	5.0	1.3
EtOH	3.8	7.9	5.9	0.4
PrOH	1.2	1.7	1.4	0.0

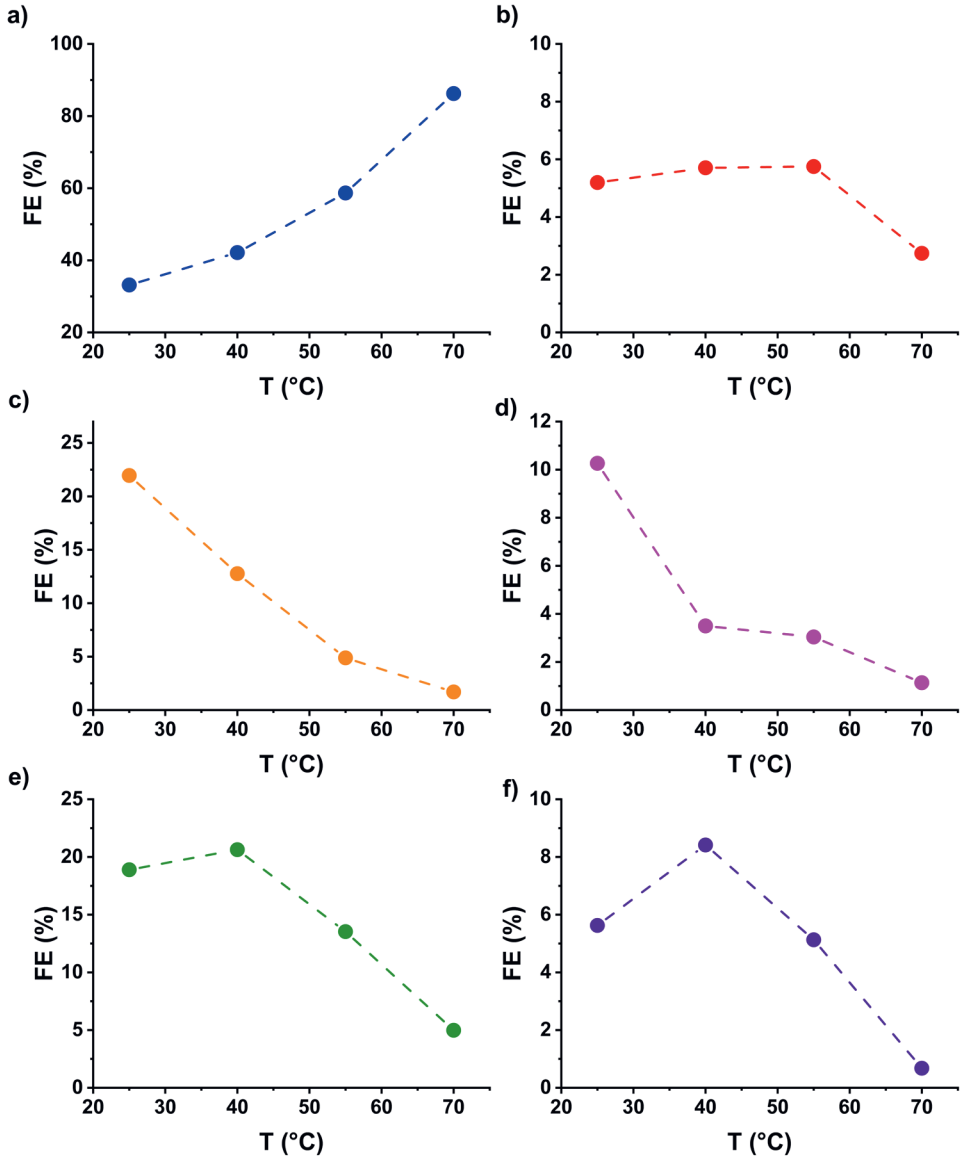


Figure B.9 Faradaic efficiency of CO2RR at different temperatures with constant CO_2 bulk concentrations by changing the partial pressure in 0.1 M $KHCO_3$ at -1.1 V vs. RHE a) hydrogen b) CO c) methane d) formic acid e) ethylene f) ethanol, and g) 1-propanol. Dotted lines are a guide to the eye and error bars are determined from at least 3 measurements.

B.6 Stirring experiments

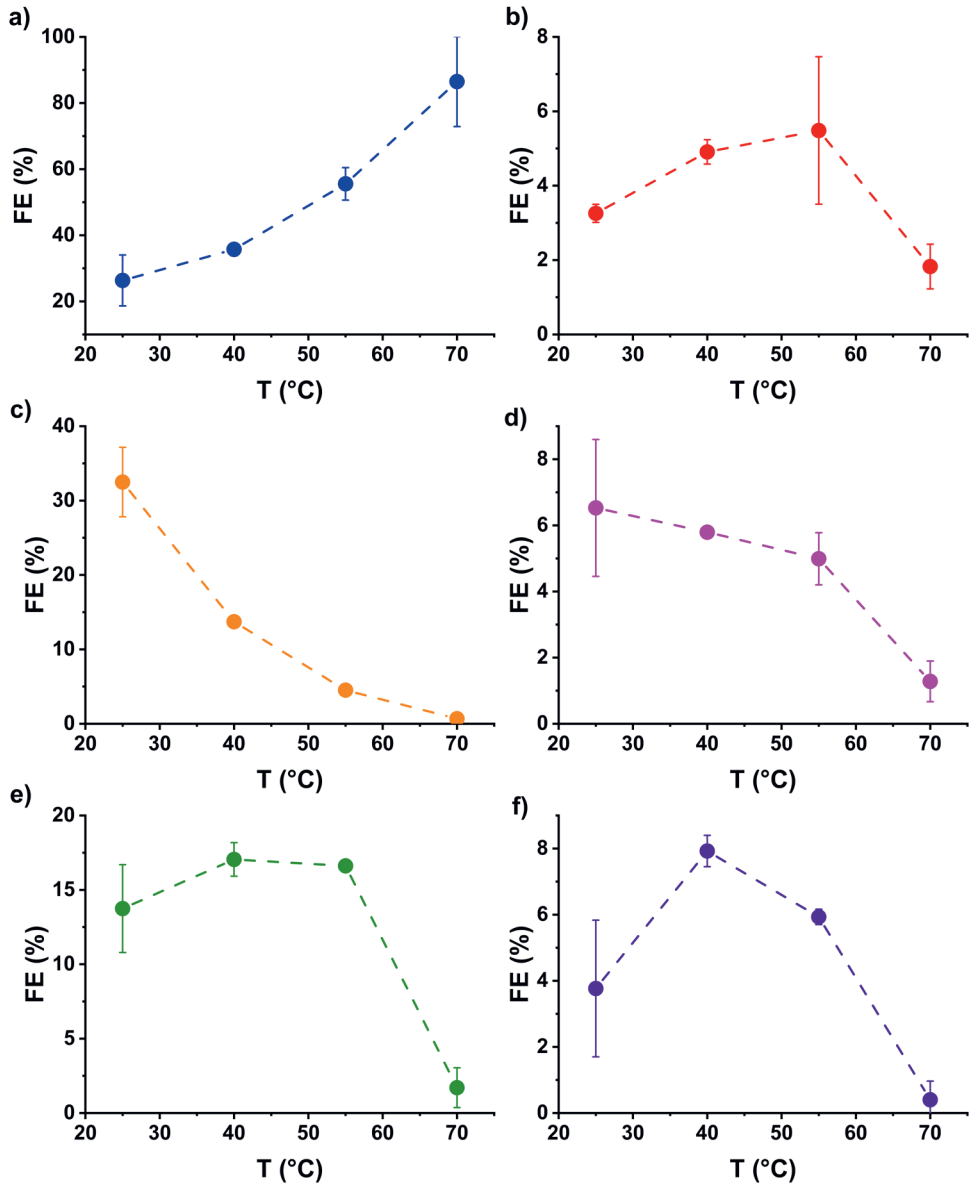


Figure B.10 Faradaic efficiency of CO2RR at different temperatures while stirring with a stirring bar at 1000 rpm in 0.1 M $KHCO_3$ at -1.1 V vs. RHE for a) hydrogen b) CO c) methane d) formic acid e) ethylene f) ethanol, and g) 1-propanol. Dotted lines are a guide to the eye and error bars are determined from at least 3 measurements.

Table B.6 Faradaic efficiency for CO2RR at different temperatures at -1.1V vs. RHE while stirring with at stirring bar at 1000 rpm

stirring		FE (%)		
	25 °C	40 °C	55 °C	70 °C
H_2	33.2	42.1	58.7	86.2
CO	5.2	5.7	5.8	2.7
CH_4	22.0	12.8	4.9	1.7
C_2H	18.9	20.6	13.5	5.0
HCOOH	10.3	3.5	3.0	1.1
EtOH	5.6	8.4	5.1	0.7
PrOH	3.4	2.6	1.2	0.0

B.7 Raman spectroscopy measurements

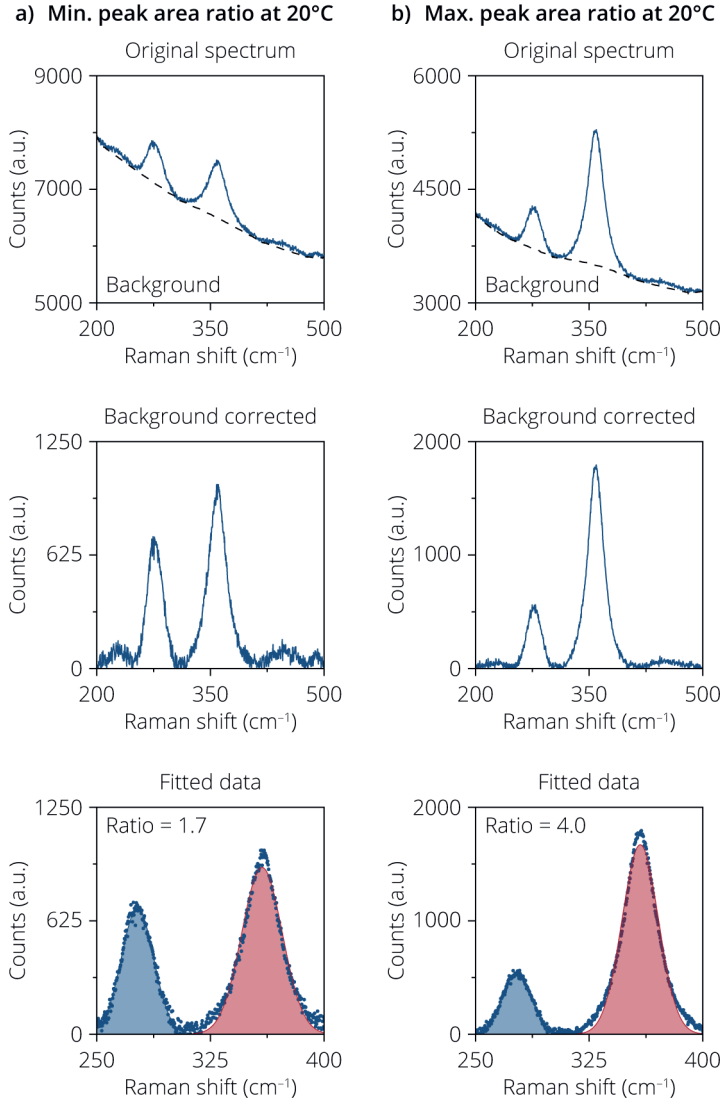


Figure B.11 Example of the data processing of the Raman data. Panel a) shows an example with small peak area ratios and b) with large peak area ratios. From top to bottom the Figure B.hows the original spectrum, the background corrected spectrum and then the data that is fitted with a Gaussian peak fitting procedure to calculate the area of the 280 cm^{-1} and 360 cm^{-1} peaks in blue and red, respectively.

Supporting Discussion: As mentioned in the experimental section, the obtained spectra were baseline corrected using the SNIP algorithm for background elimination. [1] After this background correction, a Gaussian fit was performed on the individual spectra to calculate the area of the 280 and 360 cm^{-1} features. The Raman shift window between 250 and 400 cm^{-1} was used for the fits, with a set boundary between the two peaks at 310 cm^{-1}. The ratio of the 360 and 280 cm^{-1} peaks areas was then used to determine the CO coverage qualitatively.

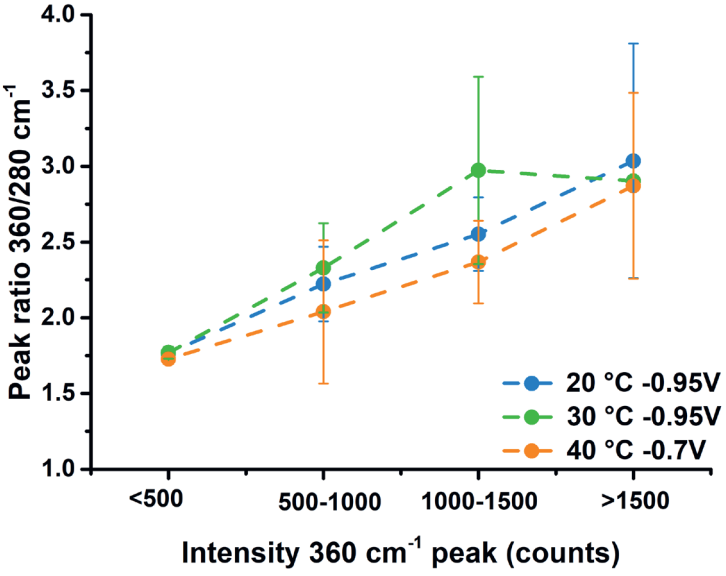


Figure B.12 The ratio between 360 and 280 cm^{-1} peak areas on Cu in 0.1 M $KHCO_3$ vs. the peak intensity of the 360 cm^{-1} peak, which is used as a proxy for the intensity of the Raman spectra. Three different conditions are shown to illustrate that this trend is not a coincidence. It can be seen that the ratio depends on the intensity of the peaks: at higher intensities the peak area ratio increases.

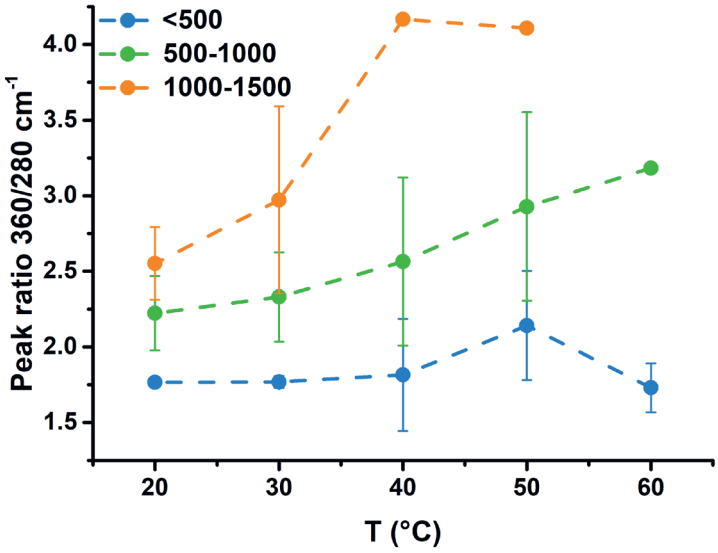


Figure B.13 The ratio between 360 and 280 cm^{-1} peak area on Cu in 0.1 M $KHCO_3$ vs. temperature at -0.95 V vs. RHE. It can be seen that the intensity of the Raman spectra, here indicated by the peak intensity of the 360 cm^{-1} peak, influences the peak ratio. The effect of temperature on the peak ratio and thus the CO coverage is more pronounced with more intense peaks.

Supporting discussion: In Figure 3b, the 280 and 360 cm^{-1} Raman features with the lowest intensities were not taken into account, because we observe that the peak area ratio also seems to depend on the intensity of these peaks, as can be seen in Figure B.12. When the spectra are more intense, as indicated by the peak height of the 360 cm^{-1} feature, the peak area ratio increases as well. This might be caused by the inhomogeneity of the copper surface or by the extent to which the different bands respond to the surface enhancement. Therefore, we isolate the effect of temperature on the peak area ratio by only comparing peak area ratios of spectra with similar intensity, as can be seen in Figure B.13. It can be seen that at all intensities, the CO coverage increases with temperature, although the trend becomes more pronounced when the peak area is larger. When all measured points are taken into account, the trends of Figure 3 are still observed, as can be seen in Figure B.14. However, at -0.7 V the trend is less pronounced due to the data point at 50 °C, as the measurements at this temperature contained many low intensity peaks with a lower ratio. At -0.95 V the entire trend is less pronounced as there are more low intensity peaks in general. Additionally, the peak position is potential

dependent due to the electrochemical Stark shift (Figures S15 and S16), but we find that this has negligible effect on the calculated peak ratios. From this analysis of the Raman spectra, we thus conclude an increasing trend in CO coverage with temperature, independently of the exact methods used to analyze the data.

The interfacial electric field that is generated at the electrode/electrolyte interface has implications for the energetics of the vibrational modes of the adsorbed intermediates. This is known as the vibrational Stark effect and has been researched for Raman spectroscopy during the CO2RR, where the adsorbed CO vibrations are known to show an electrochemical Stark shift due to the large dipole moment and sensitive interaction with the electrode surface. [2,3] Since the direction of the molecular vibration associated with the 280 cm^{-1} (assigned to the restricted rotation vibration of adsorbed CO) and 360 cm^{-1} (assigned to the Cu–Co stretching vibration) Raman bands with respect to the electric field is different, the expected Stark effect for these two vibrations should also be different. The molecular vibration associated with the 280 cm^{-1} Raman band is parallel to the electric field, while the molecular vibration associated with the 360 cm^{-1} Raman band is perpendicular to the electric field, hence a positive and negative Stark tuning is expected, respectively. Figure B.14 shows this positive and negative Stark tuning for the 280 and 360 cm^{-1} Raman bands, as they move in the opposite direction. These Raman spectroscopy measurements were conducted at the same applied potential and temperature, but at different locations at the Cu electrode surface. This indicates that there is an inhomogeneity in the experienced interfacial electric field per measurement spot, showing the necessity to perform these experiments at multiple measurements spots as has been done in this study.

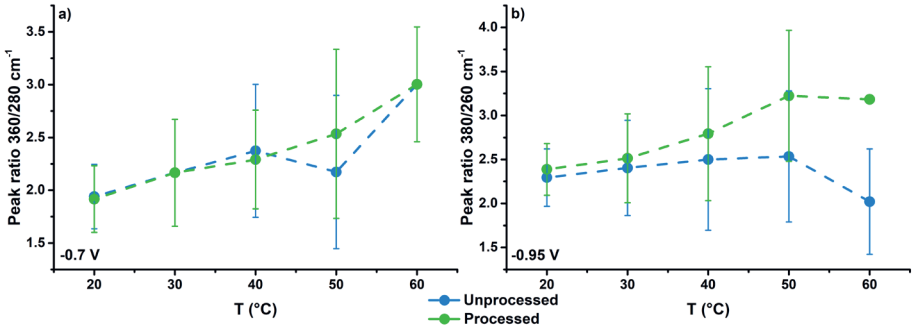


Figure B.14 The ratio between 360 and 280 cm^{-1} peak areas on Cu in 0.1 M $KHCO_3$ vs. different temperatures at a) -0.7 V and b) -0.95 V. The blue line shows the average when all measured data points are taken into account, the green line shows the average when the peaks with low intensity are not taken into account.

The previously mentioned Gaussian fits resulted in values for the peak maxima for both the 280 and 360 cm^{-1} peaks. These values are plotted in S15, showing their dependency on applied potential and temperature. The 280 cm^{-1} peak position seems to change little with applied potential (-0.7 V and -0.95 V vs. RHE, blue and orange lines, respectively). The 360 cm^{-1} peak position, however, shifts more drastically towards higher Raman shifts with higher applied potential. Both the 280 and 360 cm^{-1} peak position seem to shift towards lower Raman shift at the highest temperature measured, which might indicate a change in the interfacial potential at elevated temperatures.

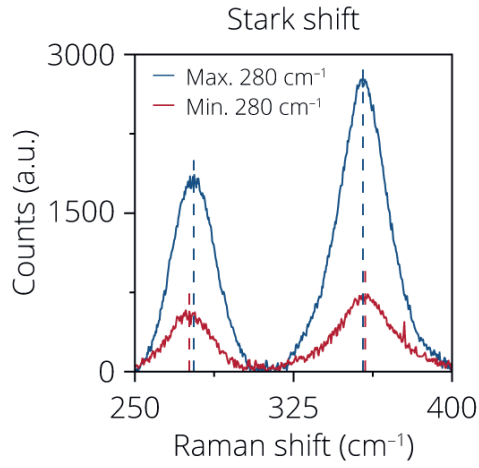


Figure B.15 Raman spectra to highlight the changing 280 and 360 cm^{-1} peak position at different measurement spots on the same Cu electrode. The spectra were both measured at 20 °C and -0.7 vs. RHE. The blue line shows the highest 280 cm^{-1} peak position, while the orange line shows the lowest 280 cm^{-1} peak position. The dashed lines indicate the peak maxima obtained from the Gaussian fitting procedure

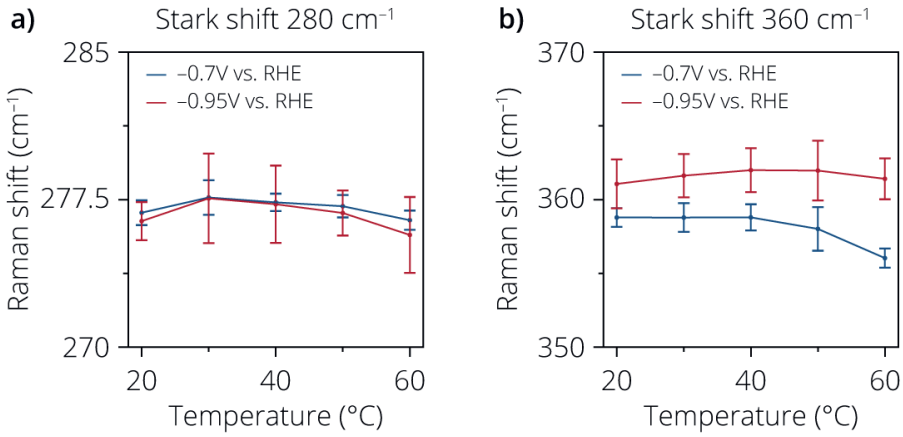


Figure B.16 Temperature- and potential-induced Stark tuning of the 280 cm^{-1} (left) and 360 cm^{-1} (right) peak maxima. The blue lines show the measurements at -0.7V vs. RHE, the orange lines at -0.95V vs. RHE. The data points are the average of 5–10 spots measured at every potential and temperature and the error bar shows the standard deviation of the peak positions of these spots.

The previously mentioned Gaussian fits resulted in values for the peak maxima for both the 280 and 360 cm^{-1} peaks. These values are plotted in S15, showing their dependency on applied potential and temperature. The 280 cm^{-1} peak position seems to change little with applied potential (-0.7 V and -0.95 V vs. RHE, blue and orange lines, respectively). The 360 cm^{-1} peak position, however, shifts more drastically towards higher Raman shifts with higher applied potential. Both the 280 and 360 cm^{-1} peak position seem to shift towards lower Raman shift at the highest temperature measured, which might indicate a change in the interfacial potential at elevated temperatures.

B.8 CO reduction experiments

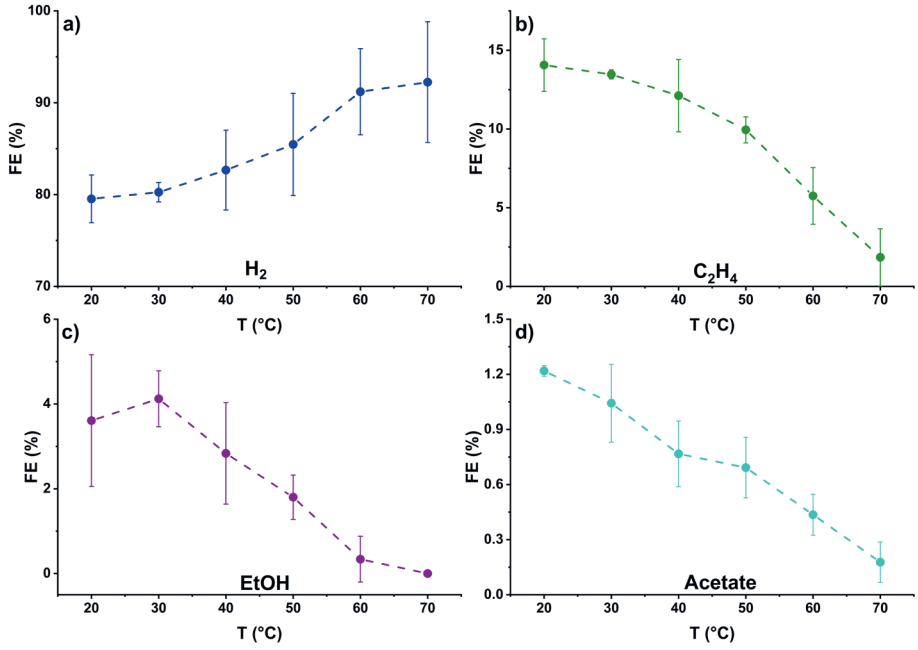


Figure B.17 Faradaic efficiency of CO reduction at different temperatures in 0.1 M KOH + 0.2 M K_2SO_4 at -0.7 V vs. RHE for a) hydrogen b) ethylene c) ethanol, and d) acetate. Dotted lines are a guide to the eye and error bars are determined from at least 3 measurements.

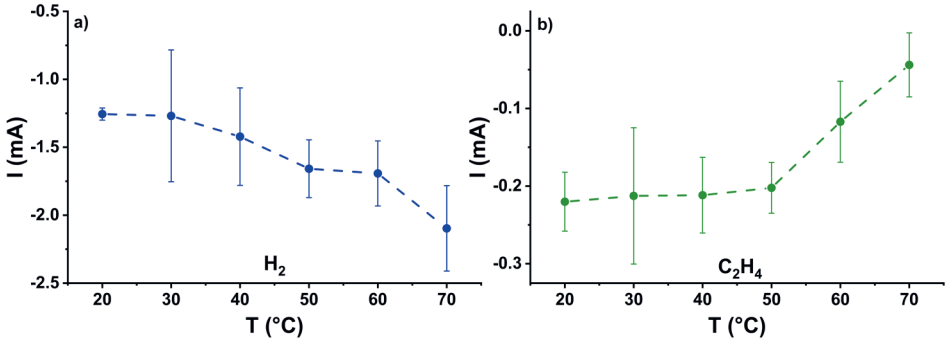


Figure B.18 Currents for CO reduction at different temperatures in 0.1 M KOH + 0.2 M K_2SO_4 at -0.7 V vs. RHE for a) hydrogen and b) ethylene. Dotted lines are a guide to the eye and error bars are determined from at least 3 measurements.

B.9 Activation Energy

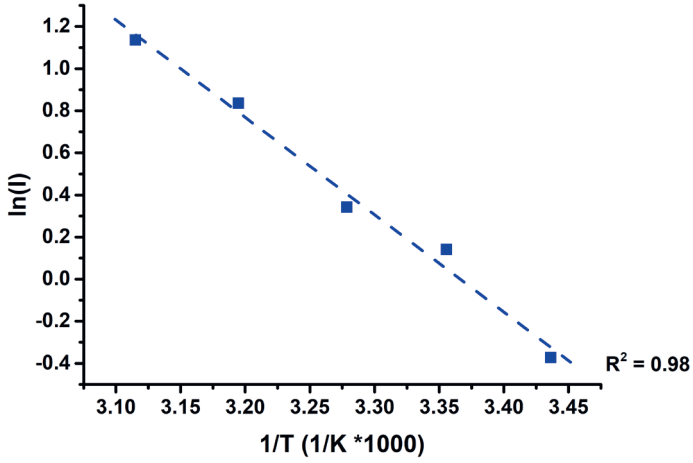


Figure B.19 Arrhenius plot of H_2 production during CO2RR at -1.1 V vs. RHE in -0.1 M $KHCO_3$. The striped line gives the trendline with the corresponding R^2 value to illustrate the linearity of the trendline.

Supporting discussion: We have shown previously that on a gold electrode, the (apparent) E_a for the CO2RR towards CO is higher than for the HER, which results in an increase in CO selectivity with increasing temperature. [4] However, Zong et al. [5] showed that on copper, the HER seems to have the highest apparent activation energy. We have tried to determine the apparent activation energy from our dataset as well, however this does not give straightforward results (Figure B.19 and S20). Ethylene and ethanol give semi-linear trends up to 48 °C. If the data point at 18 °C is not considered, they exhibit E_a of 27 ± 7 and 31 ± 8 kJ/mol, respectively, comparable to the results by Zong et al.. However, including the 18 °C data point, the E_a increases to 53 ± 16 and 50 ± 12 kJ/mol, respectively, showing that our data set is not sufficient to determine a reliable E_a. Unfortunately, the other products show non-linear trends. Only for HER we are able to determine a relatively accurate value (Figure B.19). Interestingly, the E_a for H_2 determined from our experiments is significantly lower than the value determined by Zong et al. (38 ± 2 kJ/mol vs. ~ 60 kJ/mol, respectively).

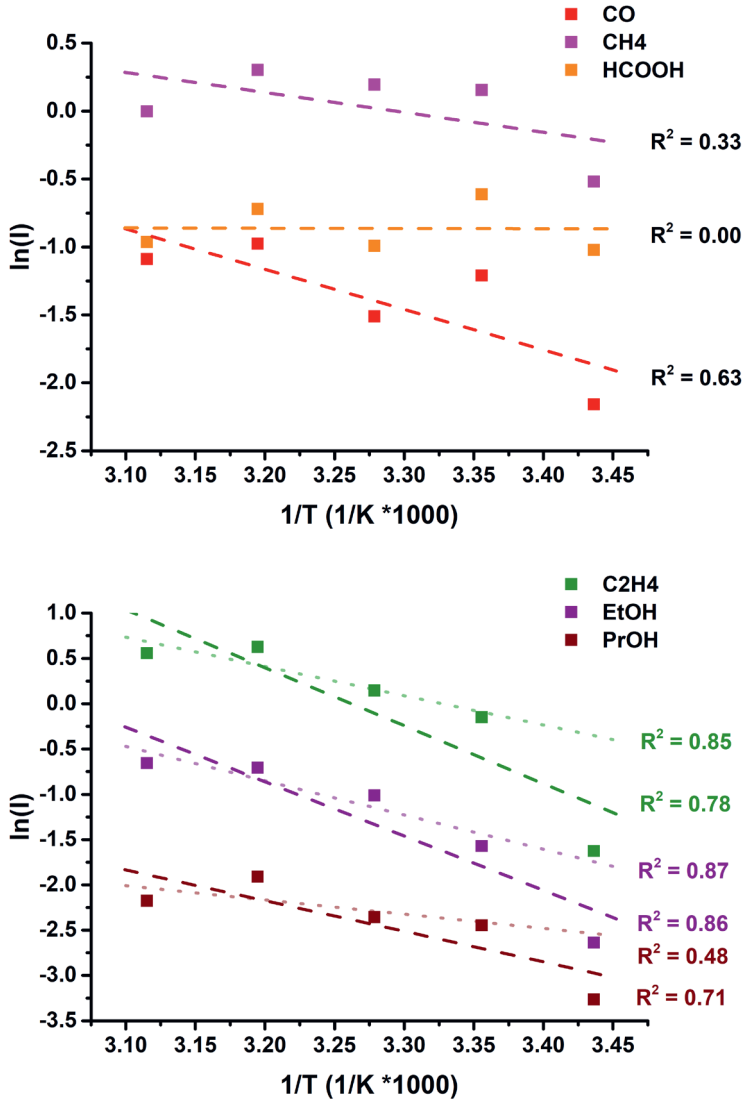


Figure B.20 Arrhenius plots of a) CO, methane, formic acid production and b) ethylene, ethanol and 1-propanol during CO2RR at -1.1 V vs. RHE in -0.1M $KHCO_3$. The striped lines gives the trendline with the corresponding R^2 value to illustrate the linearity of the trendline. The light doted lines for the C2+ products are the trendlines without the point at 18 °C. It can be seen that the slope changes significantly.

B.10 Pb UPD experiments

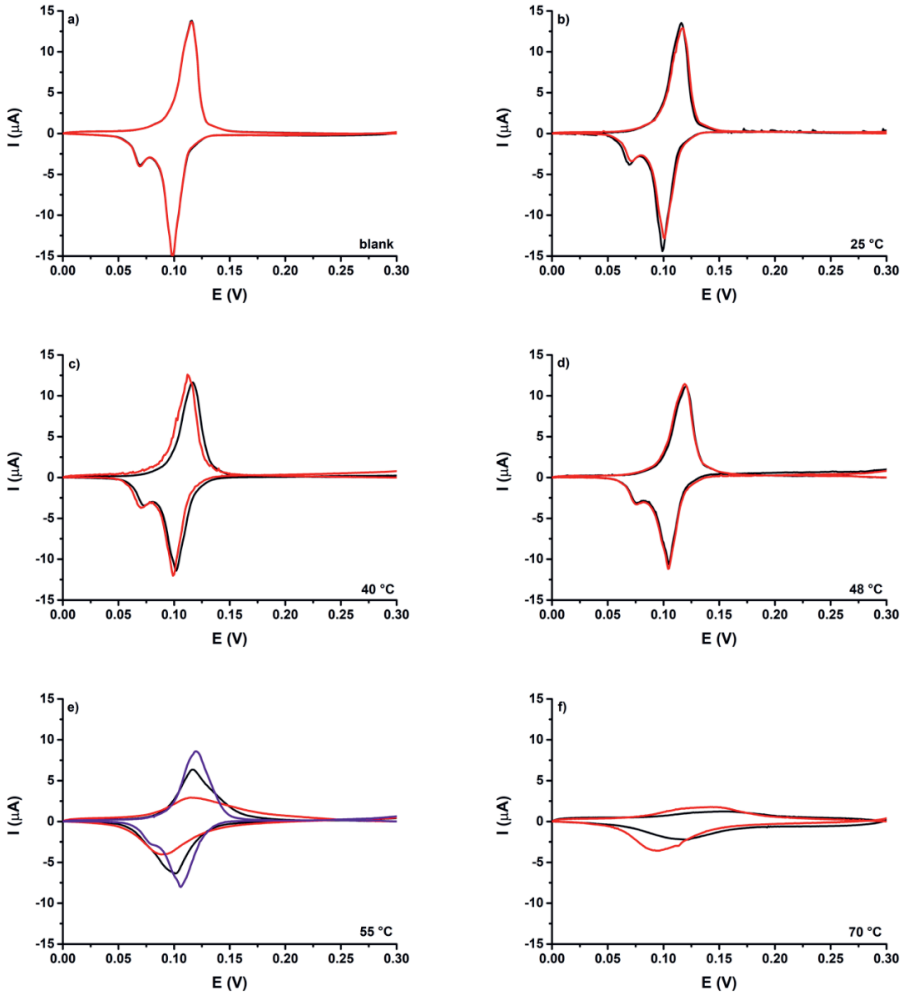


Figure B.21 Pb UPD CVs from 0.3 to 0.0 V vs. RHE at 5 mV/s in 0.1 M $NaClO_4$ + 1mM NaCl + 2 mM $PbClO_4$. A) blank CV after only polishing before CO2RR and after CO2RR for 20 min at -1.1V vs. RHE in 0.1M $KHCO_3$ at b) 25 °C c) 40 °C d) 48 °C e) 55°C f) 70 °C. The red, black and purple lines are separate experiments to illustrate reproducibility.

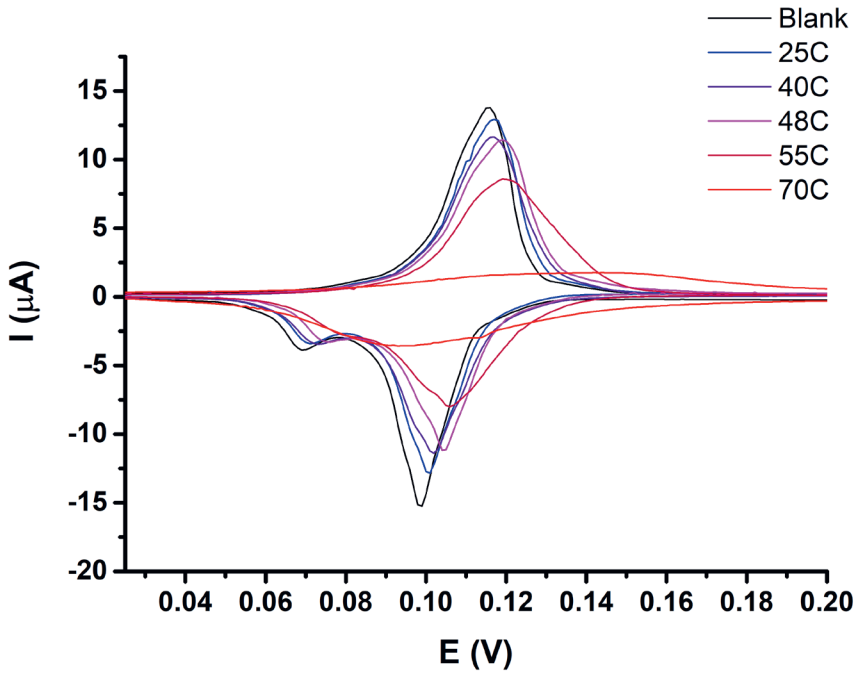


Figure B.22 Pb UPD CVs from 0.3 to 0.0 V vs. RHE at 5 mV/s in 0.1 M $NaClO_4$ + 1mM NaCl + 2 mM $PbClO_4$. The copper sample was first used for CO2RR for 20 min at -1.1V vs. RHE in 0.1 M $KHCO_3$ at different temperatures, while the blank is before CO2RR was performed.

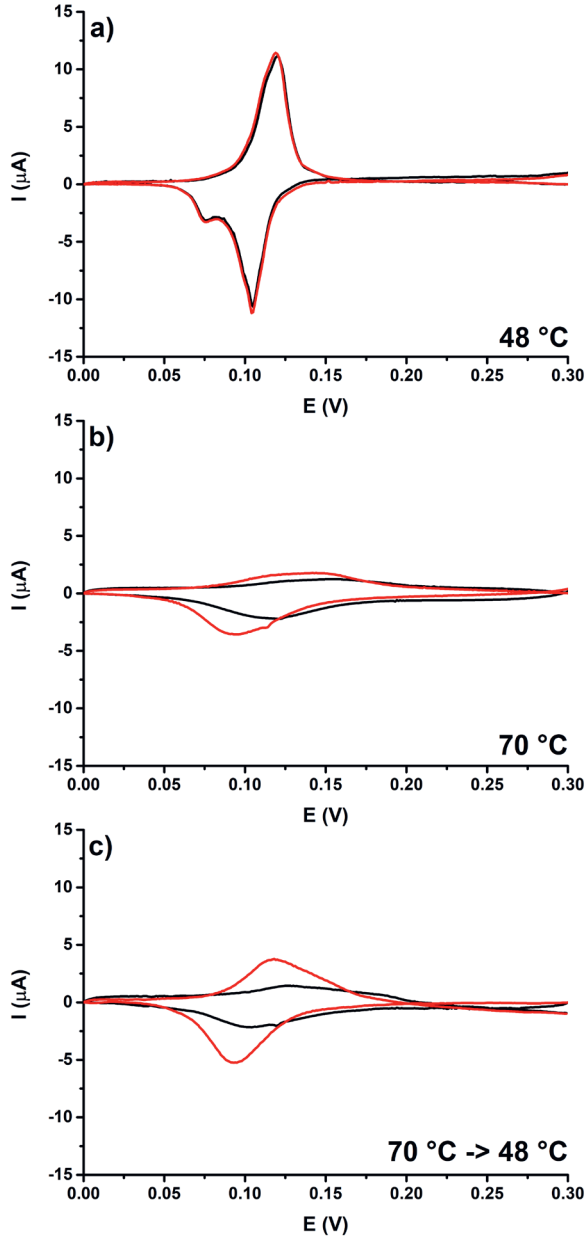


Figure B.23 Pb UPD CVs from 0.3 to 0.0 V vs. RHE at 5 mV/s in 0.1 M $NaClO_4$ + 1mM NaCl + 2 mM $PbClO_4$. a) after CO2RR for 20 min at -1.1V vs. RHE in 0.1M $KHCO_3$ at a) 48 ^{0}C b) 70 ^{0}C and c) 20 min at 70 °C and 30 min at 48 °C. The red and black line represent two different measurements.

B.11 SEM-EDX measurements

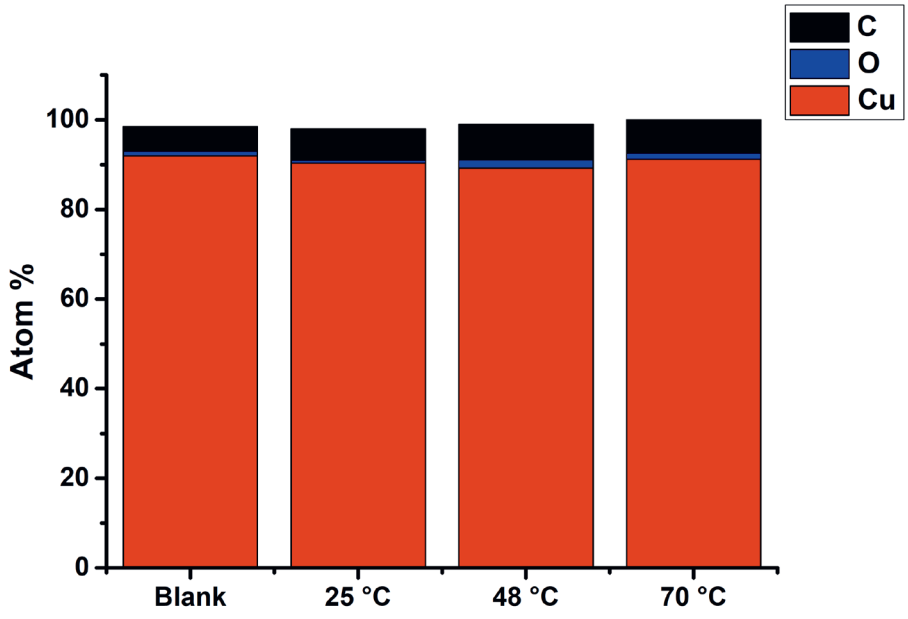
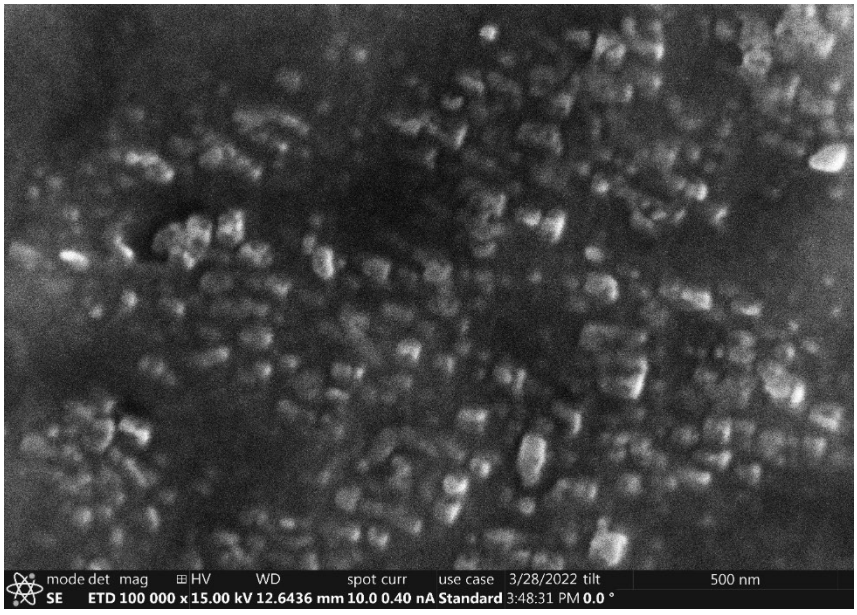
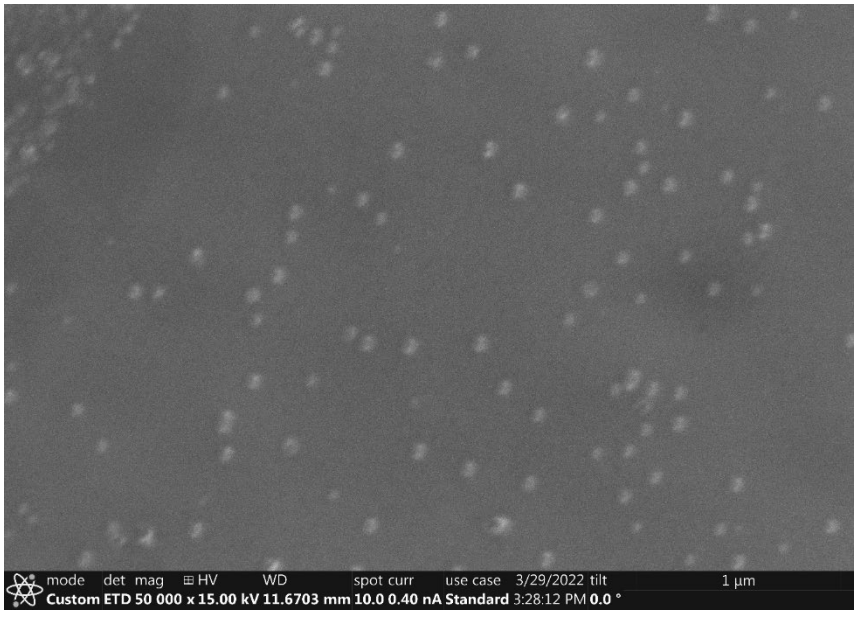


Figure B.24 Elemental composition measured using SEM-EDX of the copper surface after CO2RR at -1.1V at different temperatures and the blank before CO2RR


mode det mag HV WD spot curr use case 3/28/2022 tilt 500 nm
SE ETD 100 000 x 15.00 kV 12.6436 mm 10.0 0.40 nA Standard 3:48:31 PM 0.0 °


mode det mag HV WD spot curr use case 3/29/2022 tilt 1 µm
Custom ETD 50 000 x 15.00 kV 11.6703 mm 10.0 0.40 nA Standard 3:28:12 PM 0.0 °

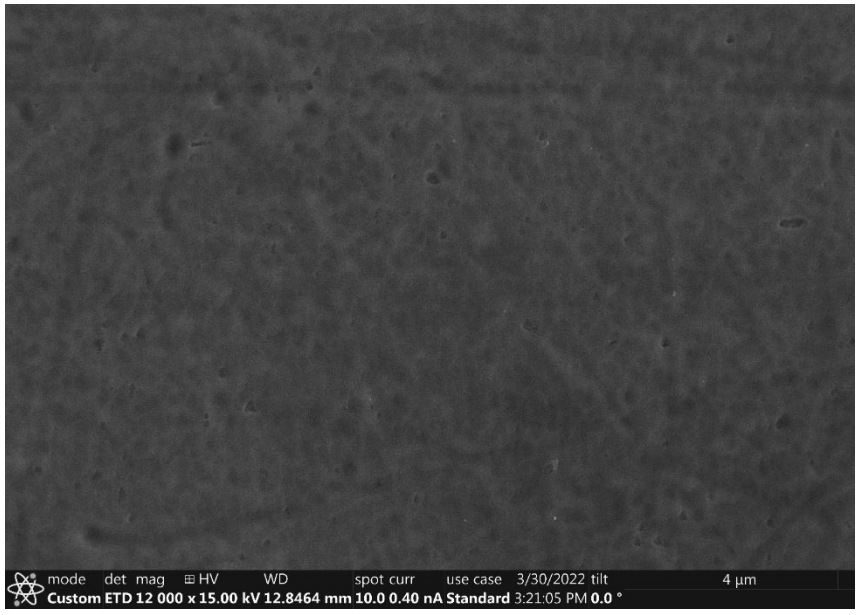


Figure B.25 SEM micrographs after CO2RR at -1.1V vs. RHE at a) 25 °C b) 48 °C c) 70 °C

B.12 Double layer capacitance measurements

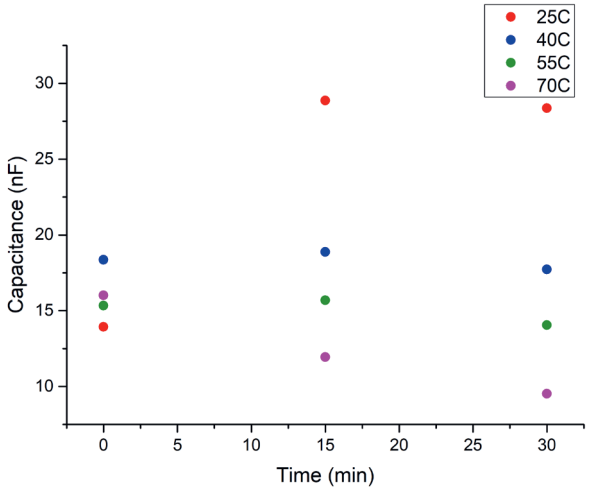


Figure B.26 Capacitance measured by double layer capacitance studies from CVs in the range -0.2 to 0.3 V vs. RHE at scan rates from 200 to 1400 mV/s before and after 15 and 30 min of CO2RR at different temperatures. The capacitance was determined at 0.0 V vs. RHE.

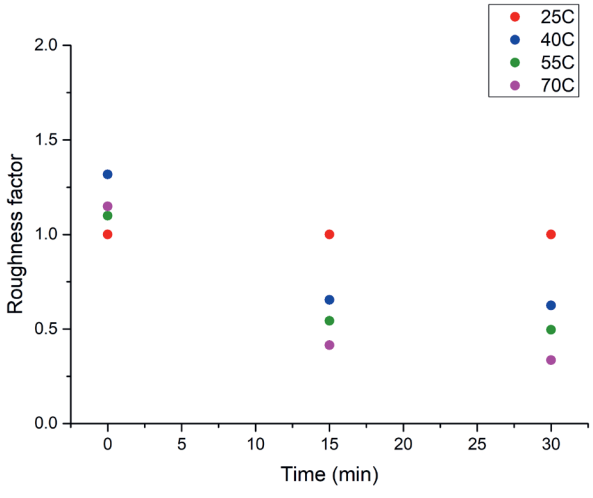


Figure B.27 Roughness factor determined from the data from Figure B.23 by setting the capacitance at 25 °C as 1 at every time interval and normalize the other values.

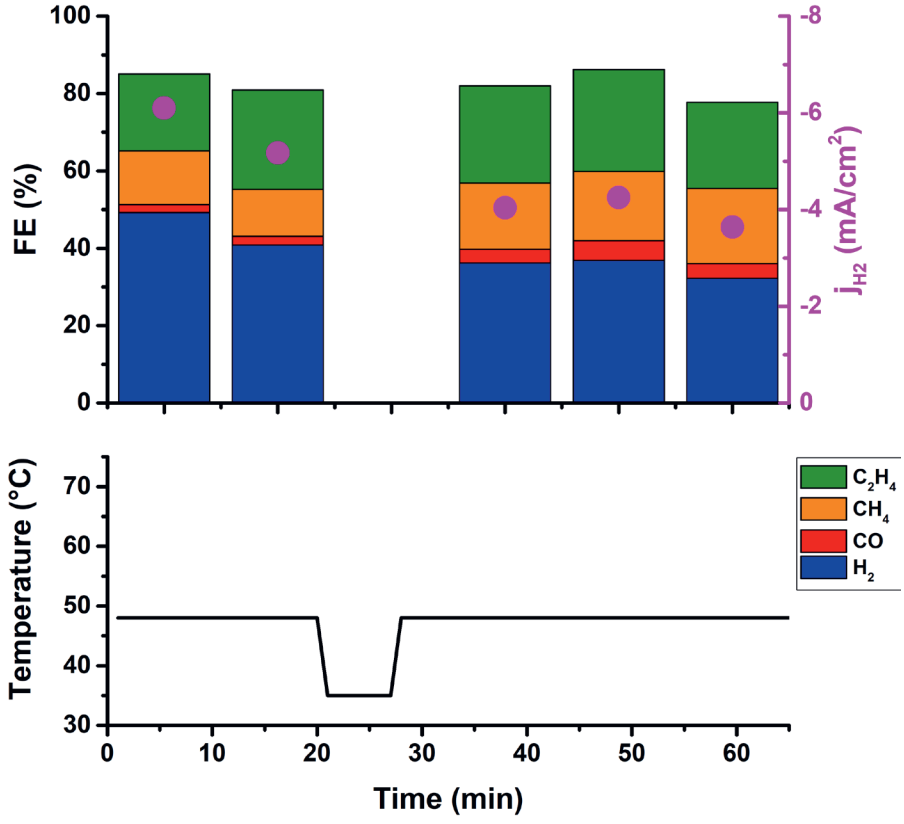


Figure B.28 Reversibility experiments, control experiment to Figure 6. The upper panel shows the Faradaic Efficiency of the gaseous products of CO2RR at -1.1V vs. RHE after 5 and 19 min at 48 °C, and after cooling down at 5, 19 and 32 min at 48 °C. The magenta dots show the patial current density towards H_2. The lower panel shows the temperature profile.

References

1. Caccia, M. *et al. Educational Note* **2**, ED3163 (2013).
2. Chernyshova, I. V, Somasundaran, P. & Ponnurangam, S. *Proceedings of the National Academy of Sciences* **115**, E9261–E9270 (2018).
3. Chang, X. *et al. Catal Sci Technol* **11**, 6825–6831 (2021).
4. Vos, R. E. & Koper, M. T. M. *ChemElectroChem* **9**, e20220023 (2022).
5. Zong, Y., Chakthranont, P. & Suntivich, J. *Journal of Electrochemical Energy Conversion and Storage* **17**, 1–7 (2020).

C

Supporting Information to Chapter 4

The temperature dependence of electrochemical CO_2 reduction on Ag and CuAg alloys

C.1 Picture and scheme of the H-cell and jacket

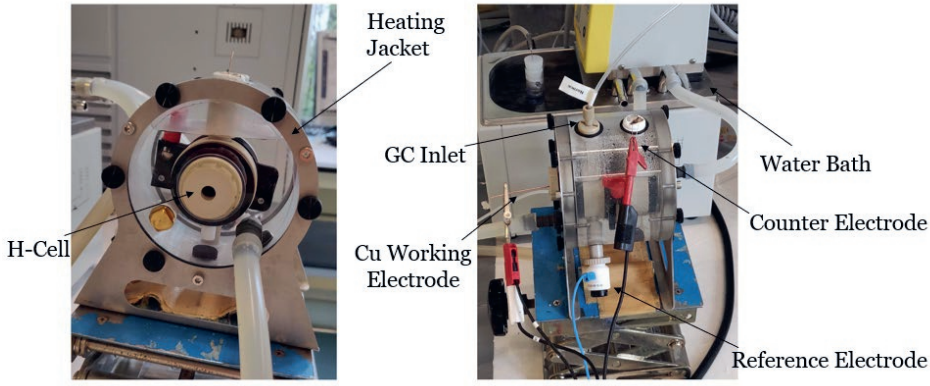


Figure C.1 Photos from the H-cell surrounded by the water jacket used to control the temperature

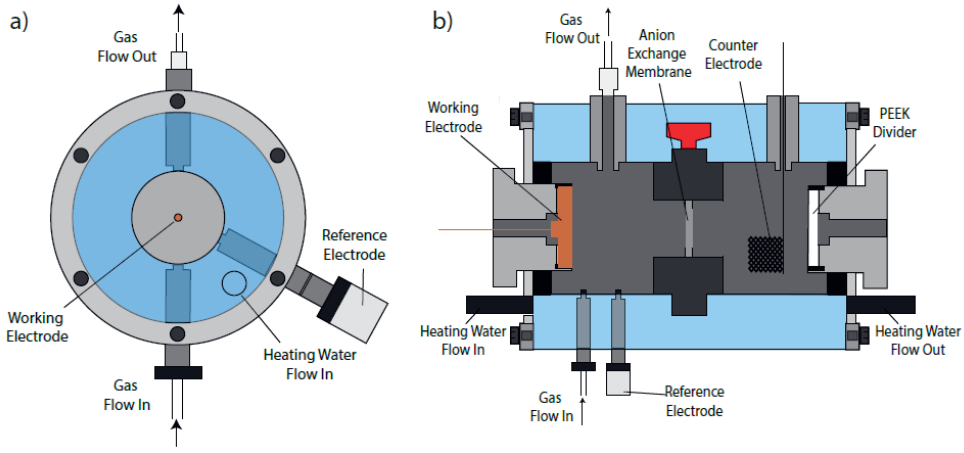


Figure C.2 Schematics of the H-cell surrounded by the water jacket used to control the temperature. a) Frontal-section of the cathodic chamber and (b) cross-section of the electrochemical H-cell with heating jacket

C.2 CO_2 concentration as function of temperature

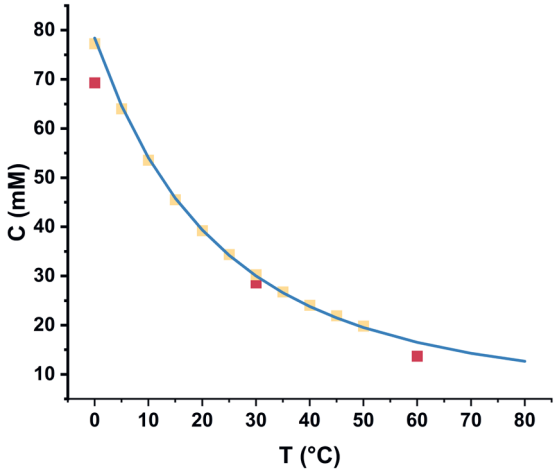


Figure C.3 the CO_2 concentration in water (yellow[1], red[2], blue[3]) as function of temperature

C.3 Partial pressure experiments

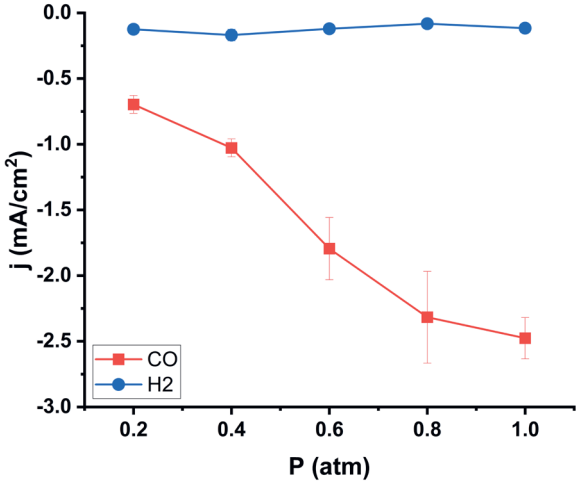


Figure C.4 Partial current densities at different partial pressures to change the bulk concentration of CO_2 at -1.1 V vs RHE at 20 °C in 0.1 M $KHCO_3$

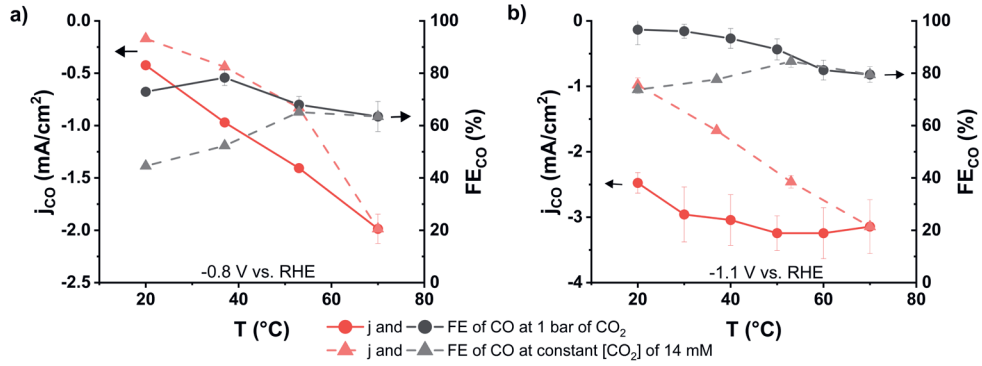


Figure C.5 Temperature effect of the partial current densities for CO and the FE for CO on Ag in 0.1 M $KHCO_3$ at constant CO_2 pressure of 1 bar for the full dark circles and at constant CO_2 concentration in electrolyte of 14 mM by changing the partial pressure accordingly in dashed light triangles at a) at -0.8 V and b) -1.1 V vs RHE

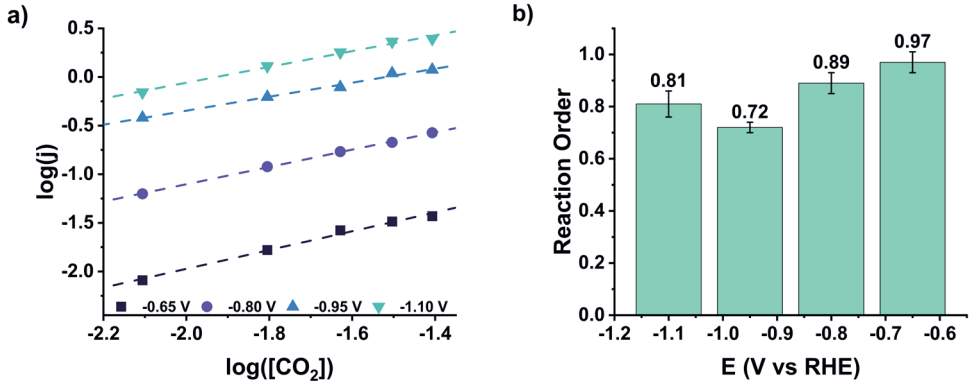


Figure C.6 Reaction order of CO_2 at different potentials in 0.1 M $KHCO_3$. From the plot in a) the reaction order in b) has been determined

C.4 Au map of temperature and potential dependence

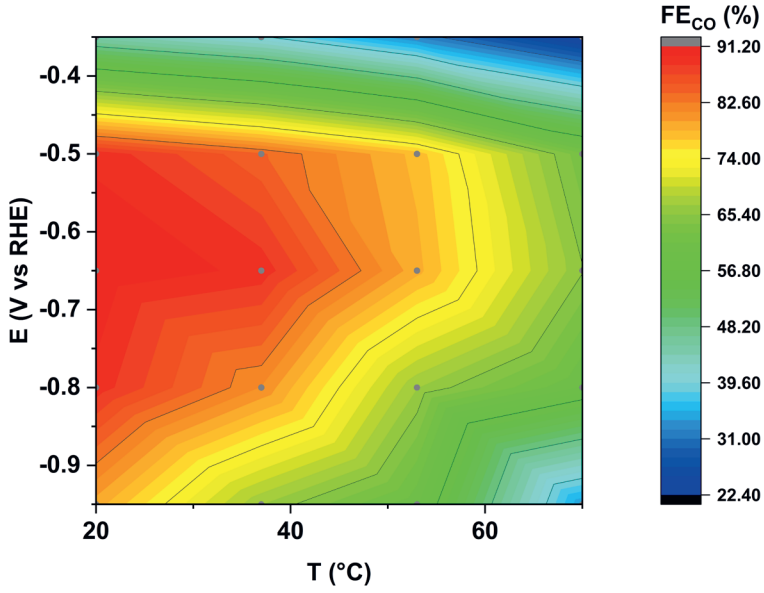


Figure C.7 Map of the Faradaic efficiency of CO on Au in the GC setup vs temperature and pressure in 0.1 M $KHCO_3$

C.5 Mass transport effect

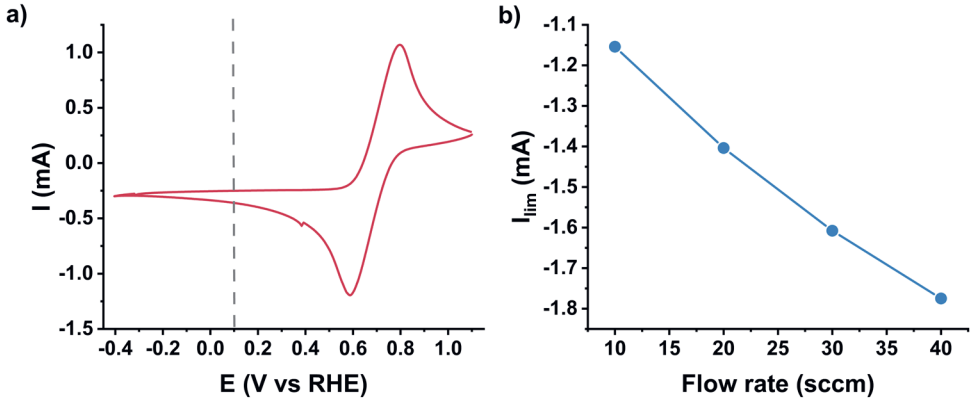


Figure C.8 a) the CV of $K_3Fe(CN)_6$ at 20 mV/s without an flow in CO_2 saturated 0.1 M $KHCO_3$ b) the limiting current of $K_3Fe(CN)_6$ at 0.1 V vs RHE in the GC cell showing that increased flow rates lead to improved mass transport

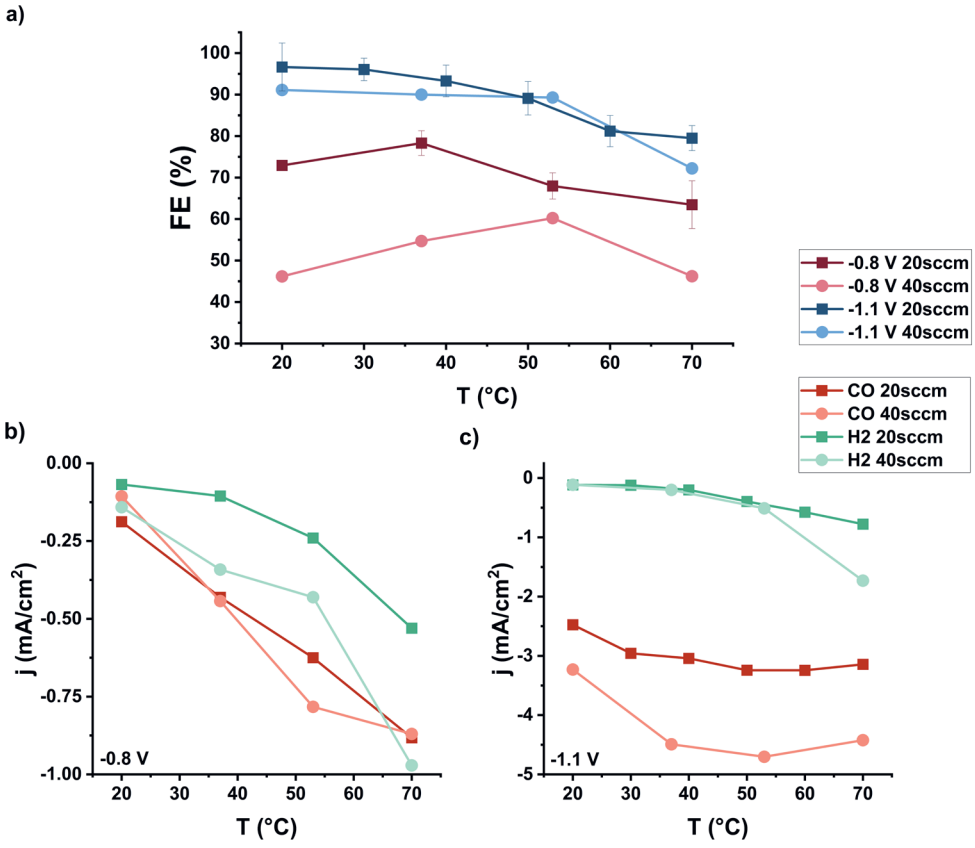


Figure C.9 Effect of mass transport on the CO_2 reduction on Ag in the GC cell in 0.1 M $KHCO_3$ on a) the Faradaic efficiency at different temperatures and the effect on the partial current densities to CO and H_2 at b) -0.8 V and c) -1.1 V vs RHE.

C.6 Different CuAg surface alloys

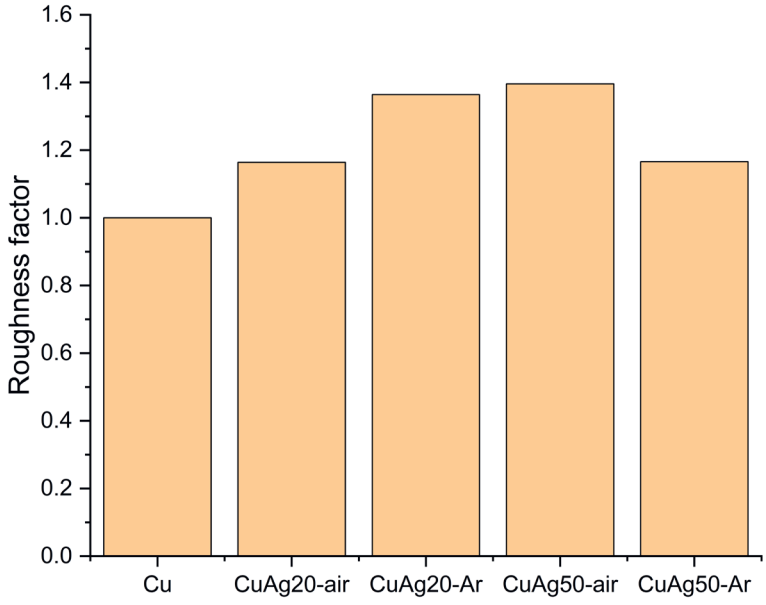


Figure C.10 Roughness factor determined from the double layer capacitance normalized to pure Cu

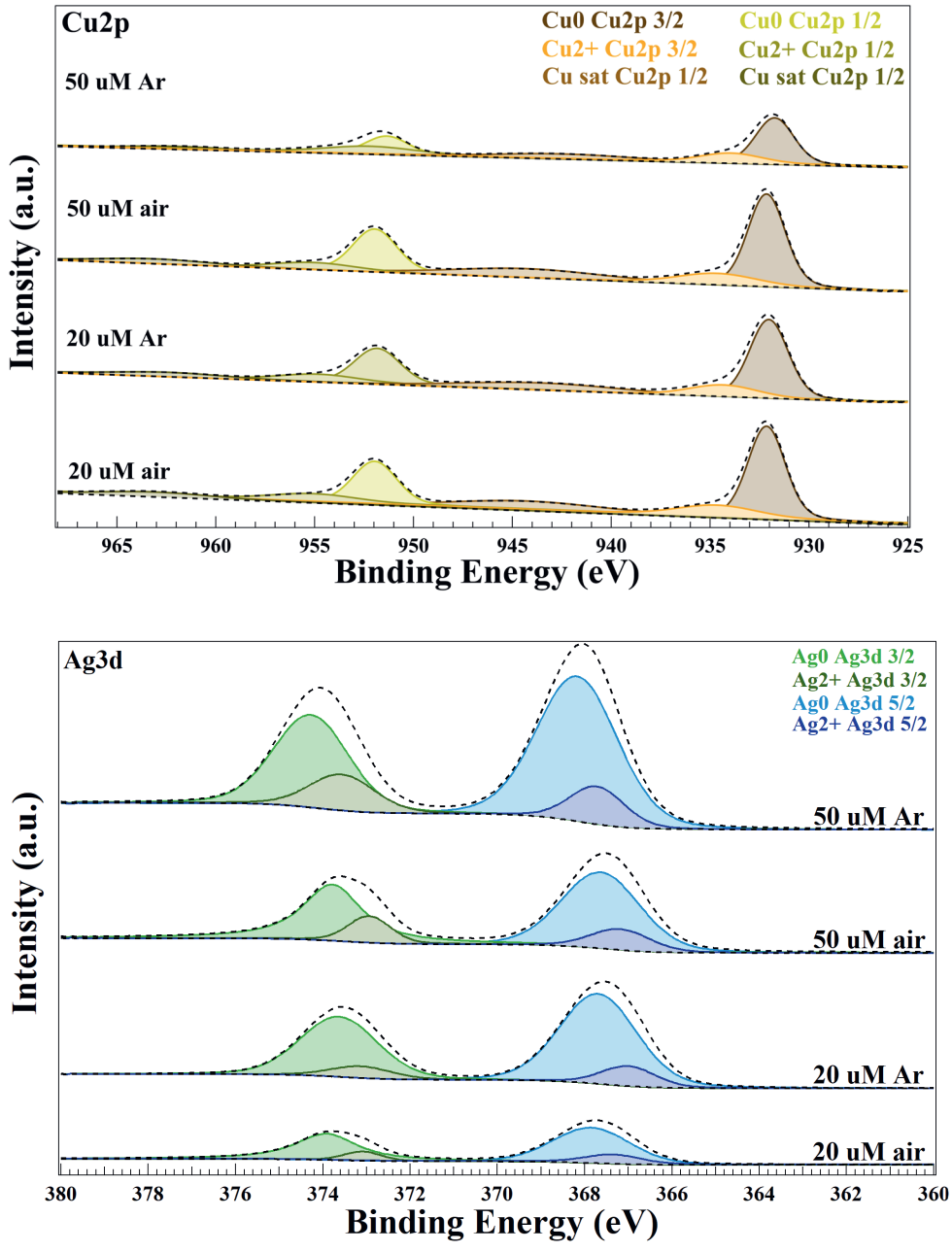
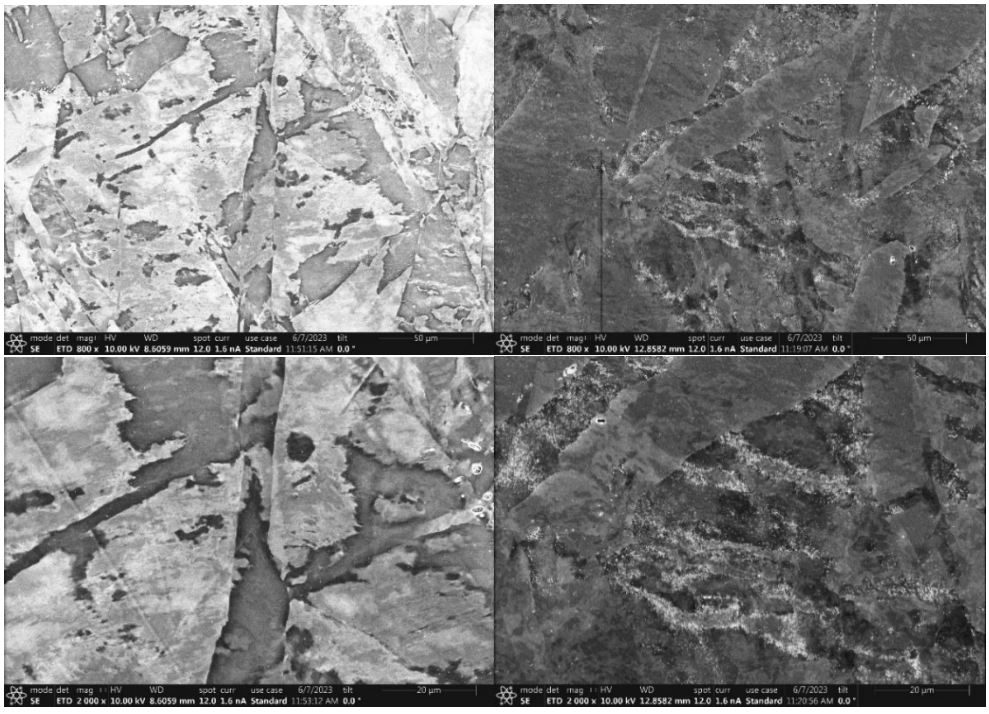


Figure C.11 the fitted Cu2p and Ag3d peaks determined with XPS

Table C.1 The area's from the Cu2p and the Ag3d peak and the calculated concentrations for the different CuAg samples

	Cu (Area)	Ag (Area)	Cu %	Ag %
20 µM $AgNO_3$ in air	8662156.76	596090.53	95.28	4.72
20 µM $AgNO_3$ in Ar	17175963.16	2665294.88	89.95	10.05
50 µM $AgNO_3$ in air	19319787.10	2429221.06	91.70	8.30
50 µM $AgNO_3$ in Ar	10443265.50	4545023.51	76.14	23.86



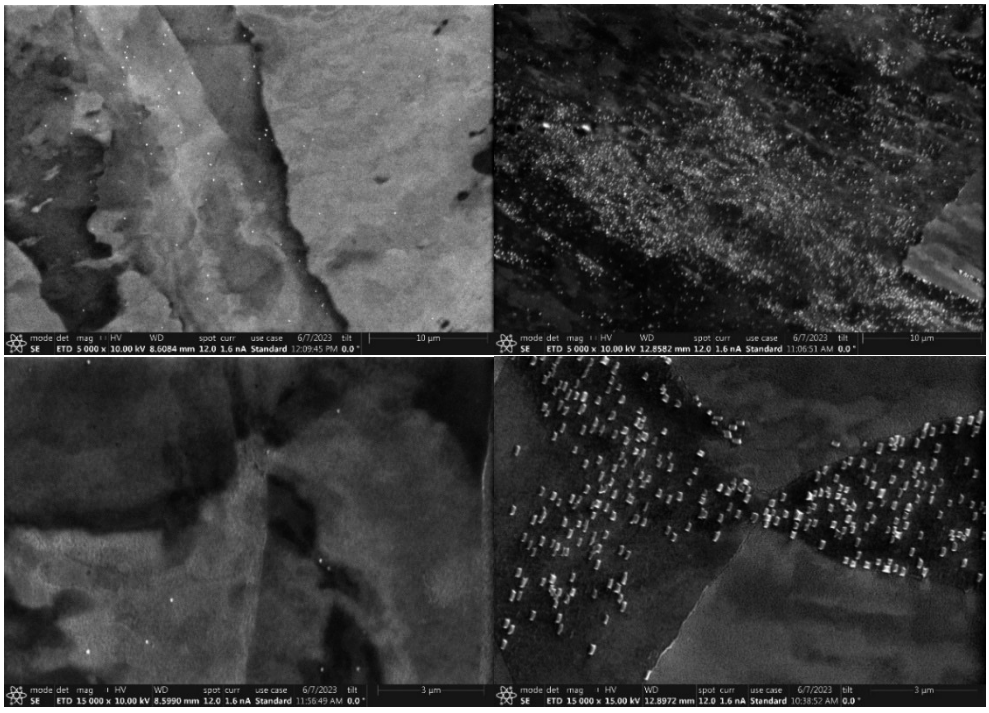


Figure C.12 SEM of CuAg20 on the left and CuAg50 on the right at different magnifications (800, 2000, 5000, 15000x)

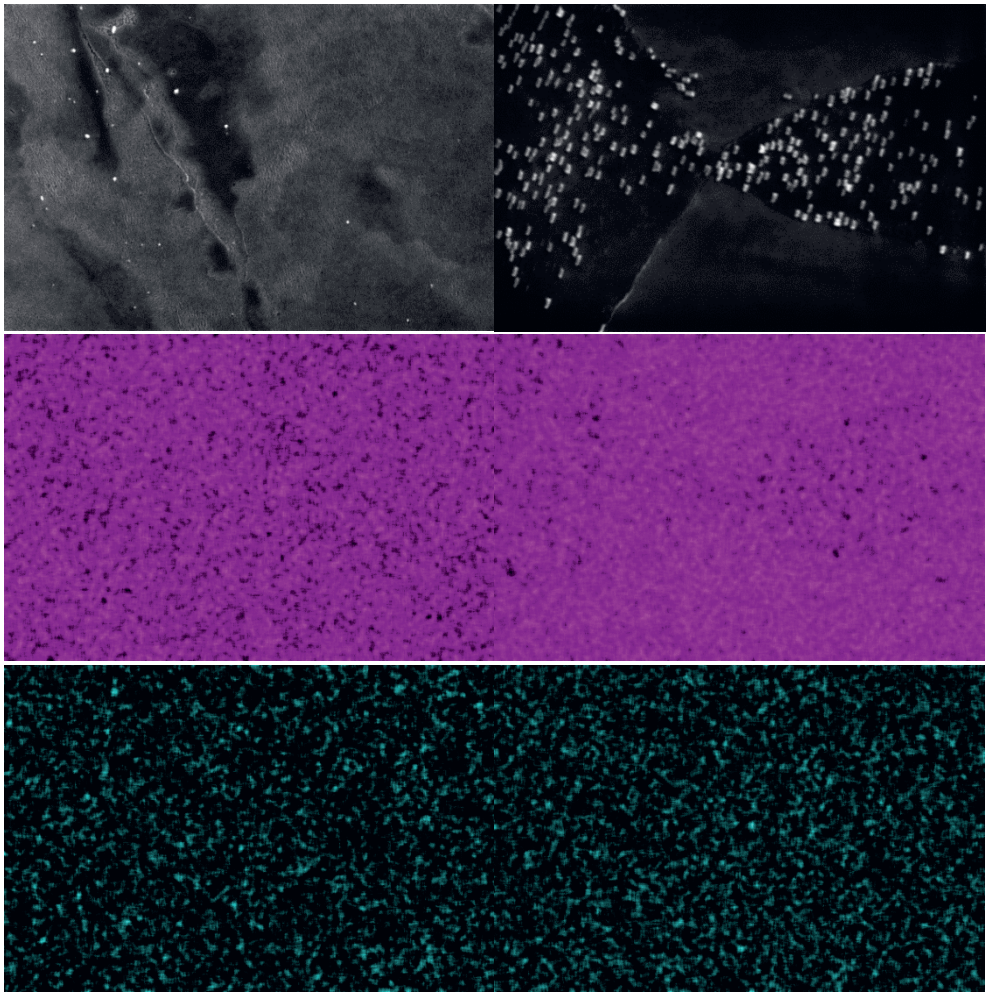


Figure C.13 EDX maps of the CuAg20 catalyst on the left and the CuAg50 catalysts on the right; pink is Cu, blue for Ag. The EDX map shows that Ag is uniformly distributed over the surface in both catalyst, as expected from galvanic exchange.

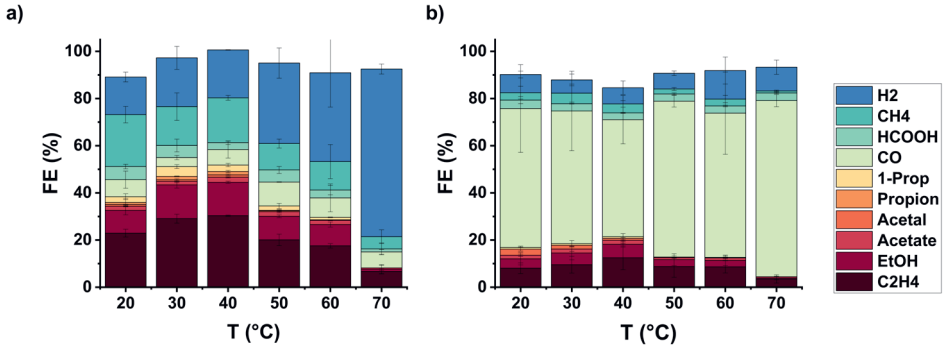


Figure C.14 Faradaic efficiencies for a) CuAg20 b) CuAg50 as function of temperature at -1.1 V vs RHE in 0.1 M $CsHCO_3$

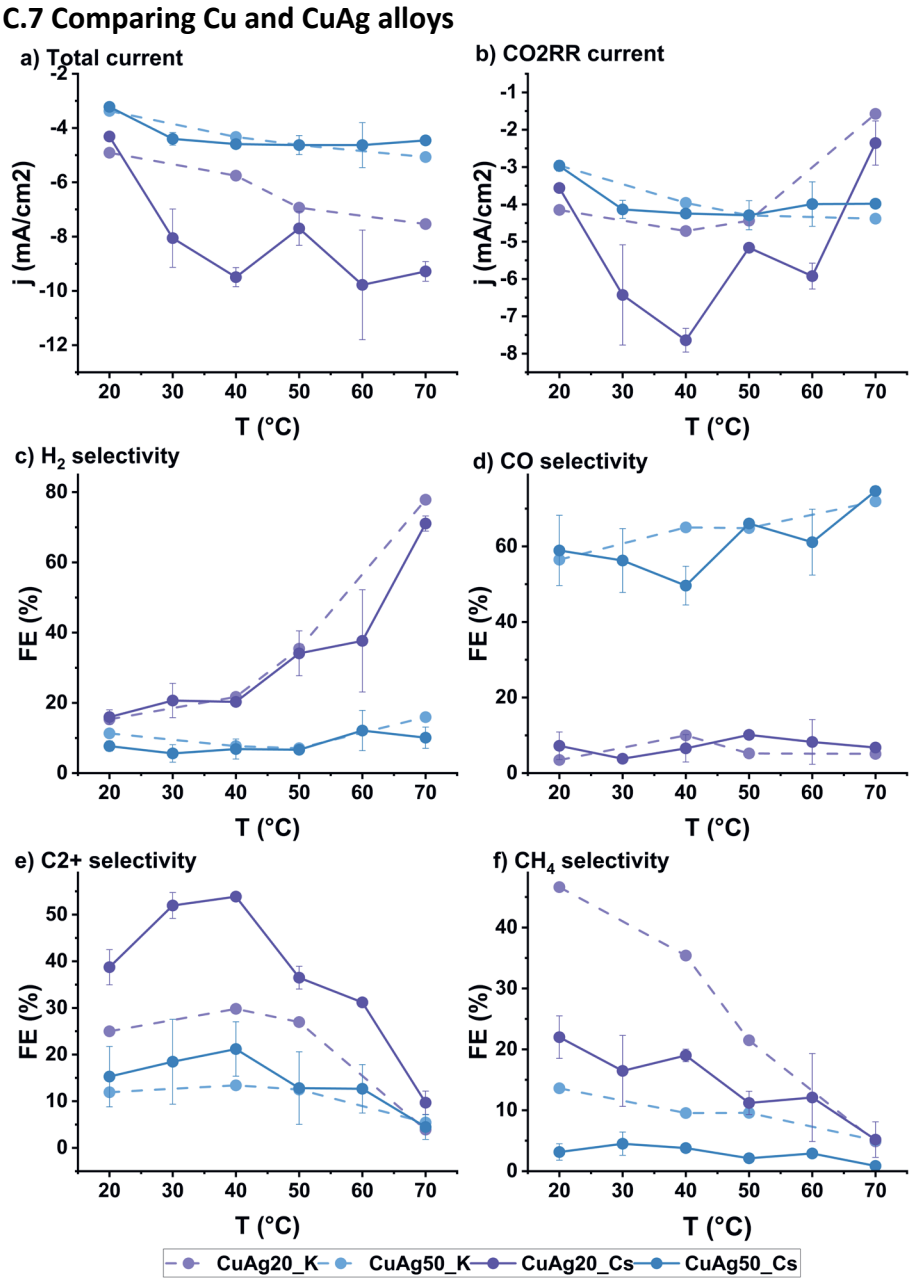


Figure C.15 a) Total current density and b) current density towards CO2RR and faradaic efficiency for c) hydrogen d) CO e) C2+ products f) CH4 for CuAg20 in purple and CuAg50 in blue at -1.1 V vs RHE in 0.1 M $KHCO_3$ (light dashed) and in 0.1 M CsHCO3 (dark full line)

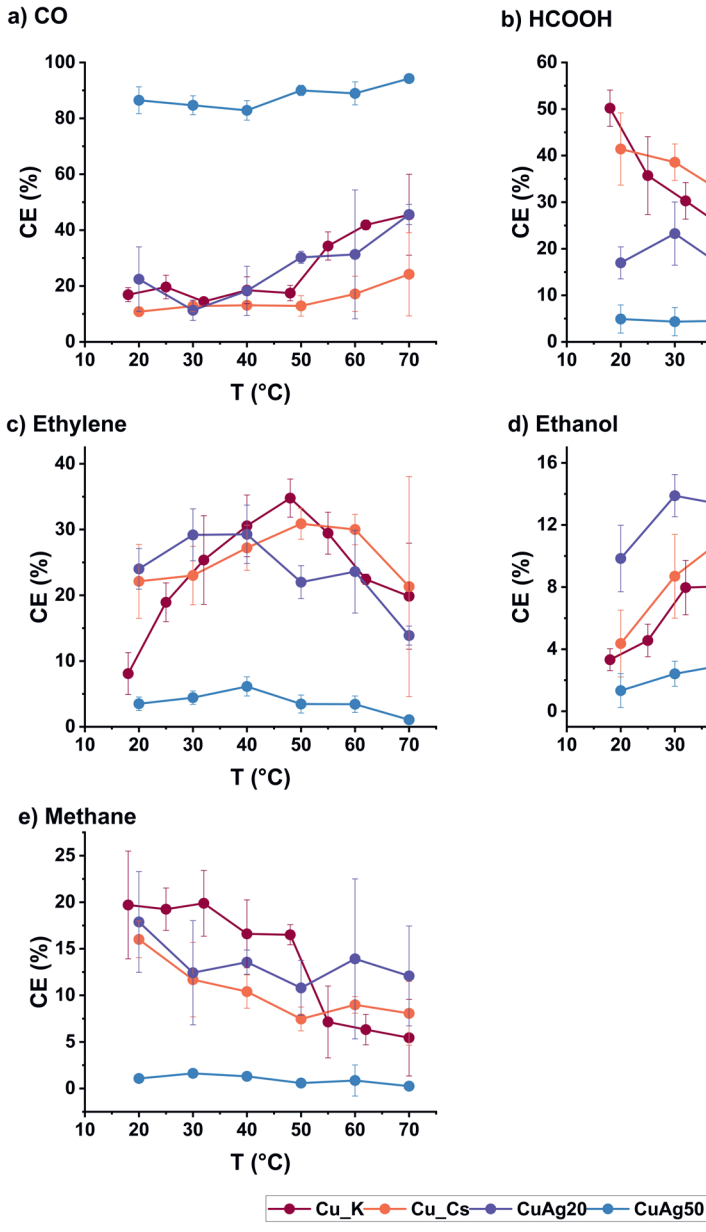


Figure C.16 Comparison of the Carbon efficiency for a) CO b) HCOOH c) ethylene d) ethanol e) methane for Cu, CuAg20 and CuAg50 at -1.1V vs RHE in 0.1 M CsHCO3 and also in 0.1 M $KHCO_3$ for Cu.

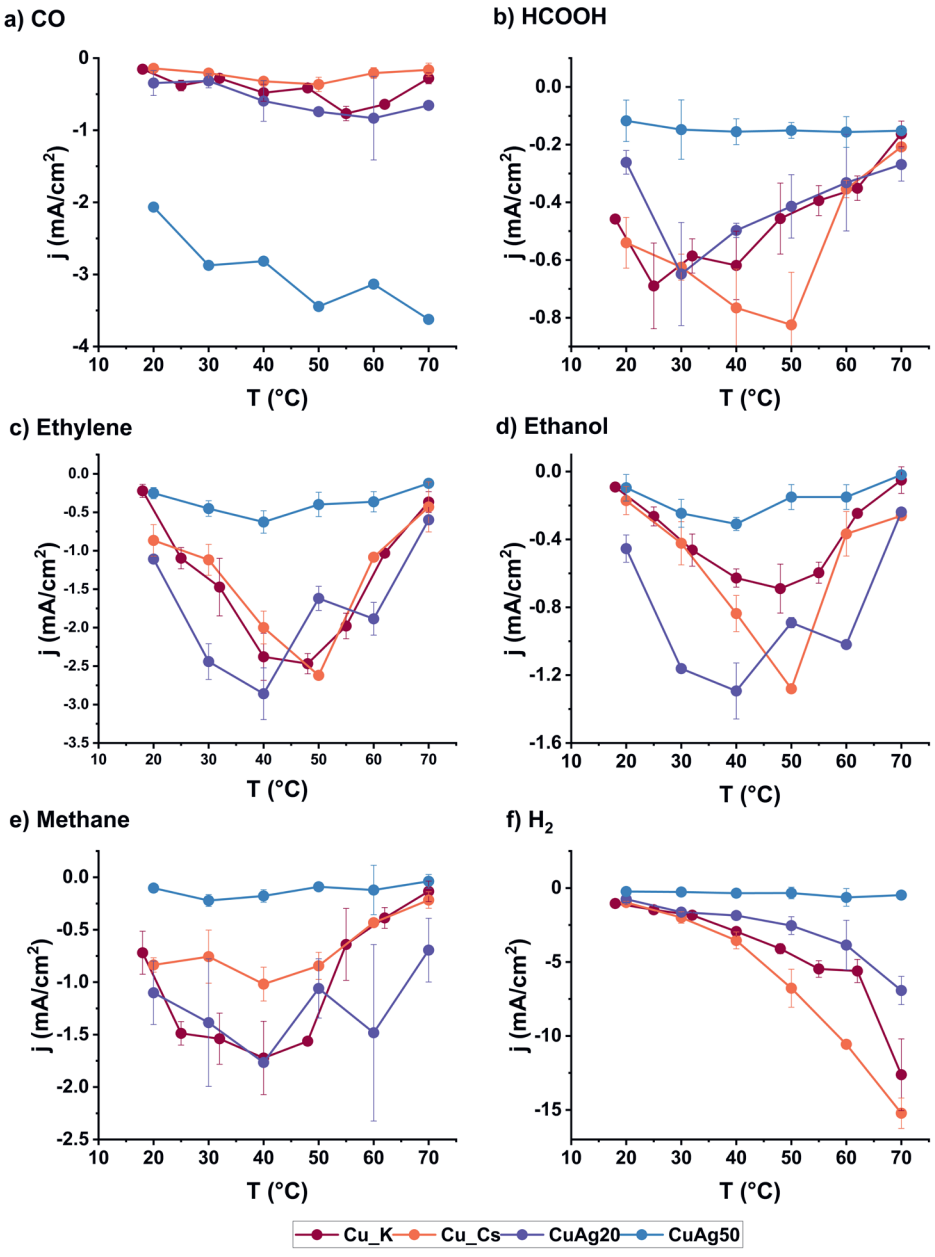


Figure C.17 Comparison of the partial current densities for a) CO b) HCOOH c) ethylene d) ethanol e) methane f) for Cu, CuAg20 and CuAg50 at -1.1V vs RHE in 0.1 M CsHCO3 and also in 0.1 M $KHCO_3$ for Cu.

C.8 Minor CO2RR products on CuAg20

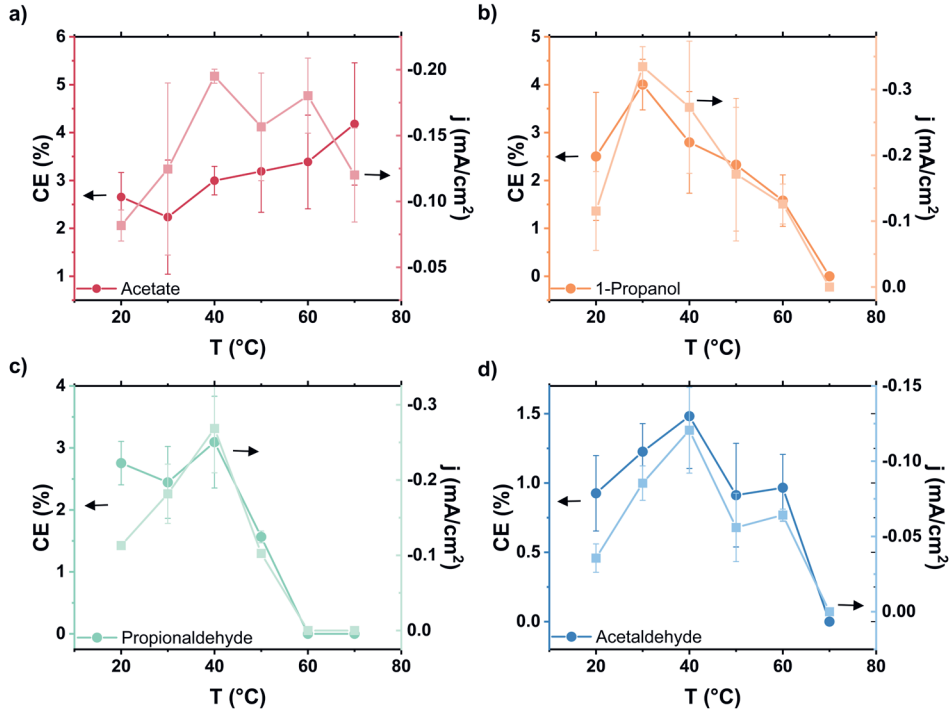


Figure C.18 Carbon efficiency and partial current density for minor liquid products on CuAg20 at -1.1 V vs RHE in $CsHCO_3$ a) acetate b) 1- propanol c) propionaldehyde and d) acetaldehyde based on the HPLC data

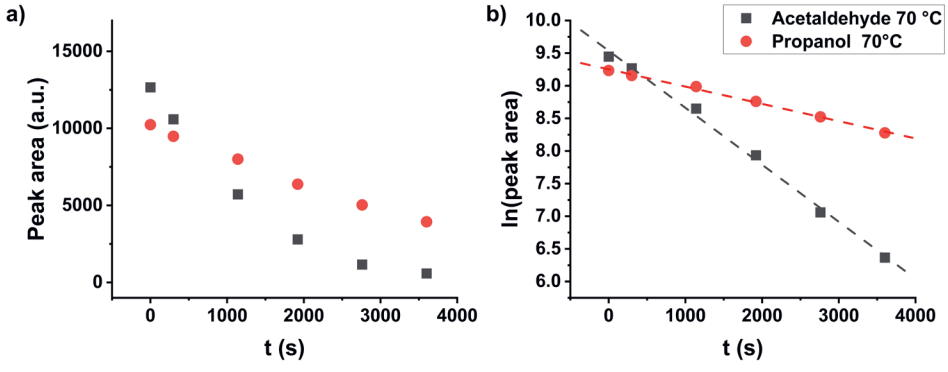


Figure C.19 Illustration of the evaporation experiments, a) the peak area and b) ln of the peak area of acetaldehyde and propanol at 70 °C vs. time

Some liquid products have low boiling points and could evaporate during the experiment, especially at elevated temperatures. To ensure this does not influence the measurements we have performed controlled evaporation studies. A solution containing 0.5 mM ethanol, 1-propanol, acetaldehyde and propionaldehyde was tested in the normal electrolysis setup, so with CO_2 flow rates of 40 sccm. After 0, 5, 19, 32, 46 and 60 min a liquid sample was taken and analyzed with HPLC. This experiment was performed at 20, 30, 40, 50, 60, 70 °C. The evaporation experiments show a 'first-order-like' behaviour, where the amount of evaporation depends on the concentration of the species in solution as can be seen in Figure C.13.

$$\text{Rate}_{\text{evaporation}} = \frac{dc}{dt} = -k_1 c \qquad \text{(S1)}$$

$$\ln(c) = -k_1 t + \ln(c_0) \qquad \text{(S2)}$$

Where c is the concentration, t is time in seconds and k_1 is the rate constant of evaporation. Equation S1 can be integrated to get equation S2, which illustrates that the rate constant can be obtained from the slope of Figure C.13b. This can be done for every product at every single temperature. If we assume the electrochemical production rate is constant over the experiment, we can define k_2 as the rate constant of the electrochemical reaction.

Then the accumulation of the product in the electrolyte is:

$$\text{Rate}_{\text{accumulation}} = \frac{dc}{dt} = -k_1 c + k_2 \qquad \text{(S3)}$$

Solving this differential equation gives

$$c(t) = \frac{k_2}{k_1} + x e^{-k_1 t} \qquad \text{(S4)}$$

Where c is the concentration, t is time in seconds and k_1 is the rate constant of evaporation, k_2 is the rate of the electrochemical reaction and x is a variable. This equation can be solved as we have 2 boundary conditions:

A: At t_0 c = 0

B: At t_{3600} c = the measured amount in the HPLC of a particular measurement

With boundary condition A we can fill in equation S4:

$$c(t) = \frac{k_2}{k_1} - \frac{k_2}{k_1} e^{-k_1 t} \qquad \text{(S5)}$$

$$k_2 = \frac{c(3600) * k_1}{1 - e^{-k_1 * 3600}} \qquad (S6)$$

And we can solve for k_2 with boundary condition B for every individual experiment and the electrochemically produced amount of the volatile liquid product is then given by: k_2 *3600

For the aldehydes, significant amounts of product evaporate. For the alcohols, only at the very high temperatures we see some evaporation, which is still very minor. Interestingly, the C3 products evaporate more than the C2 products, so propanol evaporates more than ethanol and acetaldehyde evaporates more than propionaldehyde. This is probably caused by the constant purging of the electrolyte. We also observe that without purging, hardly any of these compounds evaporate, even at 70 °C. We have corrected the graphs of the minor products from Figure C.12 and the result can be seen in Figure C.14. This correction for the evaporations does not influence the trends significantly. Only for propionaldehyde now also an optimum at 40 °C can be observed.

References

1. Harned, H. S. & Davis Jr, R. *J Am Chem Soc* **65**, 2030–2037 (1943).
2. Duan, Z. & Sun, R. *Chem Geol* **193**, 257–271 (2003).
3. Plummer, L. N. & Busenberg, E. *Geochim Cosmochim Acta* **46**, 1011–1040 (1982).

D

Supporting Information to Chapter 5

Nickel as electrocatalyst for $CO_{(2)}$ reduction; effect of temperature, potential, partial pressure and electrolyte composition

D.1 SEM-EDX images

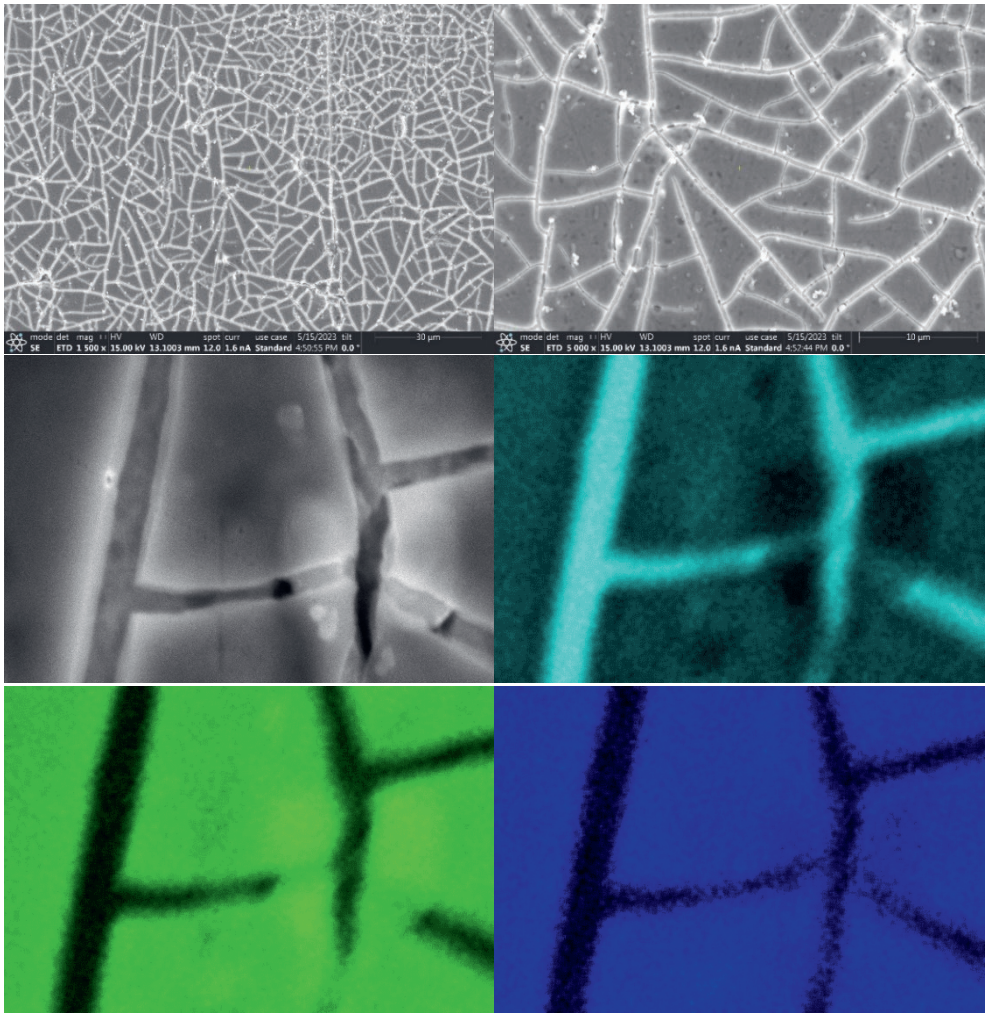


Figure D.1 SEM image of the Ni deposited electrode before CO2RR at respectively a) 1500 and b) 5000 magnification. EDX maps at 50 000 magnification showing c) the SEM image d) nickel e) oxygen f) phosphor.

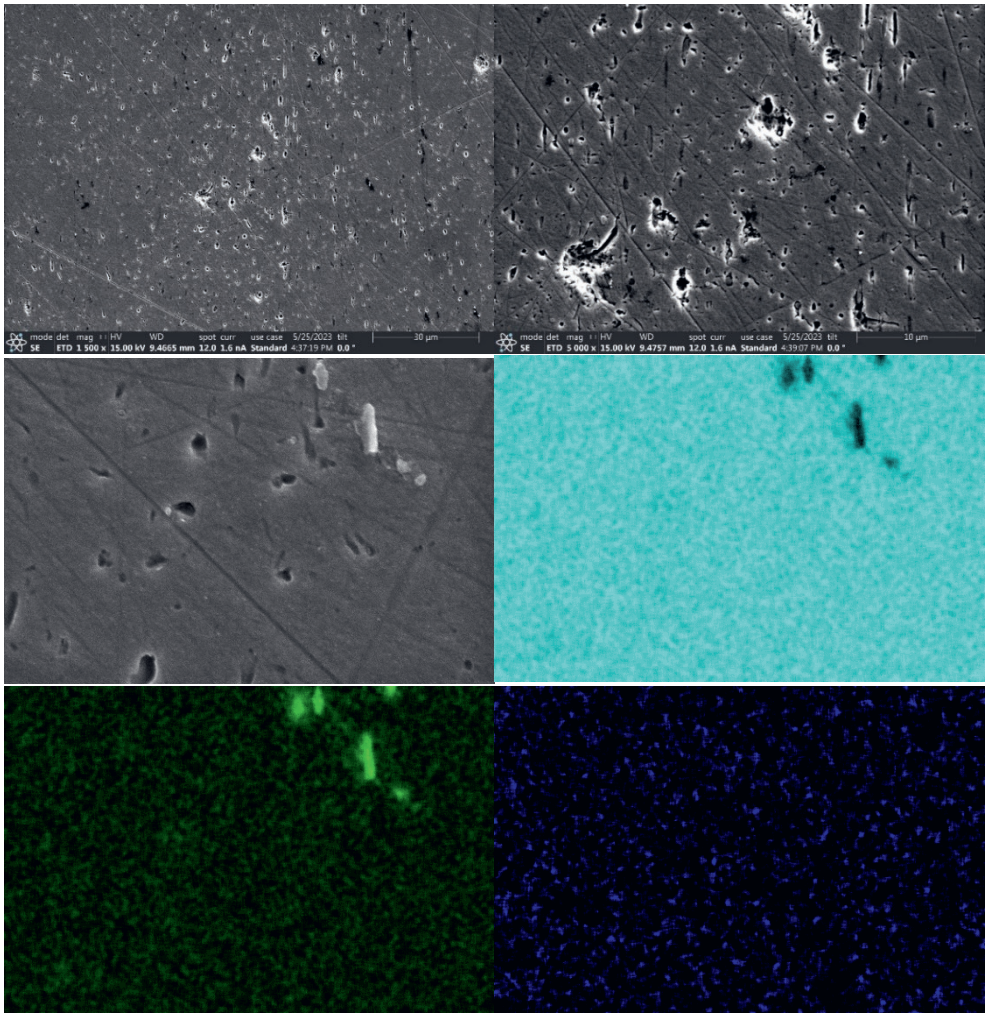


Figure D.2 SEM image of the Ni deposited electrode after CO2RR for 32 minutes at respectively a) 1500 and b) 5000 magnification. EDX maps at 50 000 magnification showing c) the SEM image d) nickel e) oxygen f) phosphor.

D.2 Effect of deposition

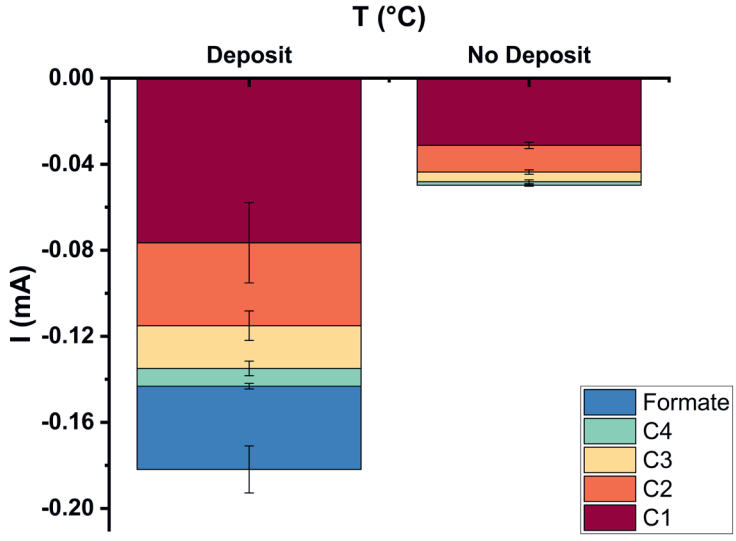


Figure D.3 Activity for CO_2 reduction on a polished polycrystalline Ni electrode with and without Ni deposition. Deposition shows higher activities at -1.175 V vs RHE at 18 °C

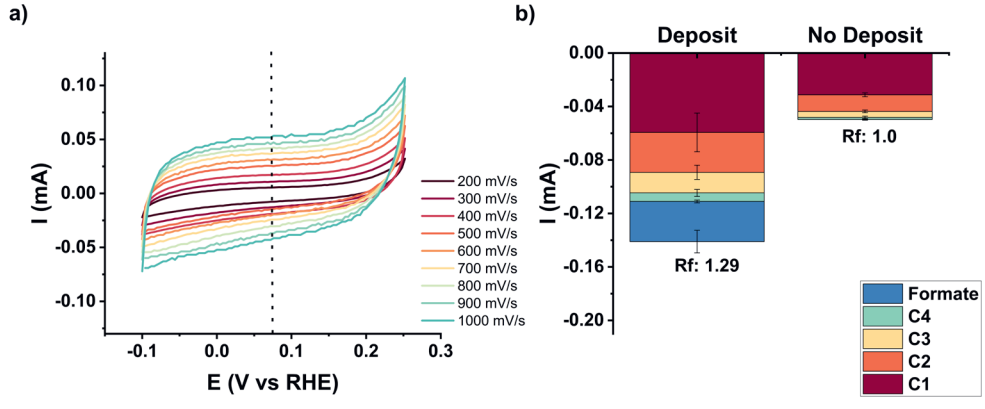


Figure D.4 a) Determination of the double layer capacitance by cyclic voltammetry. The double layer capacitance was determined at 0.075 V vs RHE and used to calculate a roughness factor (Rf). b) the roughness factor was used to normalize the deposited layer to the non-deposited catalyst, showing that the enhancement is not due to a roughness effect.

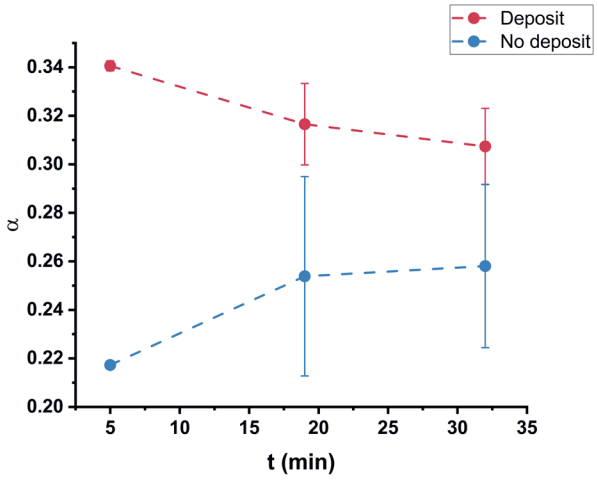


Figure D.5 Chain growth probability for CO_2 reduction on a polished polycrystalline Ni electrode with and without Ni deposition at -1.175 V vs RHE at 18 °C. Deposition shows higher chain growth probability

D.3 Anderson-Flory-Schultz plot

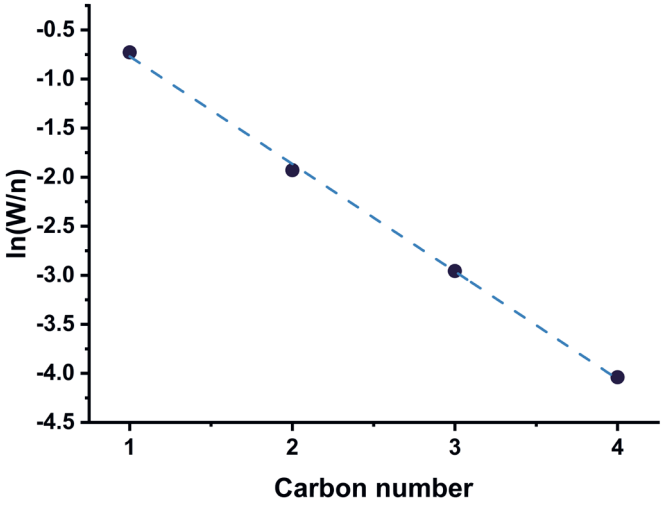


Figure D.6 Example of an Anderson-Flory plot to obtain the chain growth probability on the Ni electrode

D.4 Faradaic efficiency; temperature effect

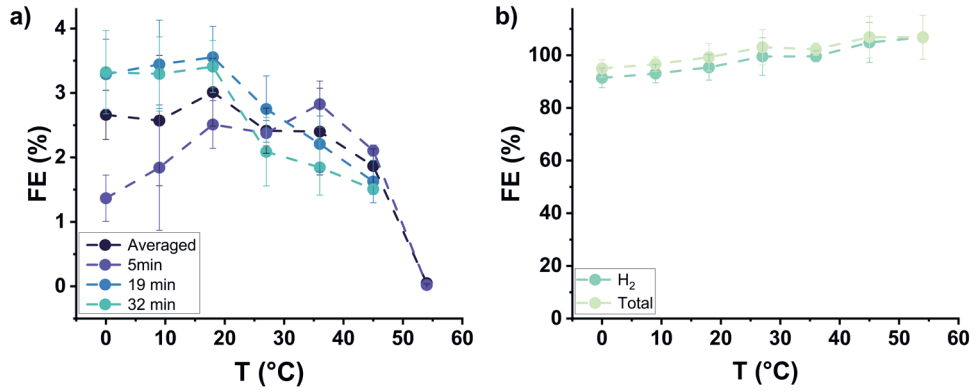


Figure D.7 Faradaic efficiency as function of temperature on Ni in 0.1 M $KHCO_3$ at -1.175 V vs RHE towards a) the total hydrocarbon formation (C1 up to C4 hydrocarbons) during CO_2 reduction both averaged and as function of time and b) towards H_2 and total FE

D.5 Deactivation by coke formation

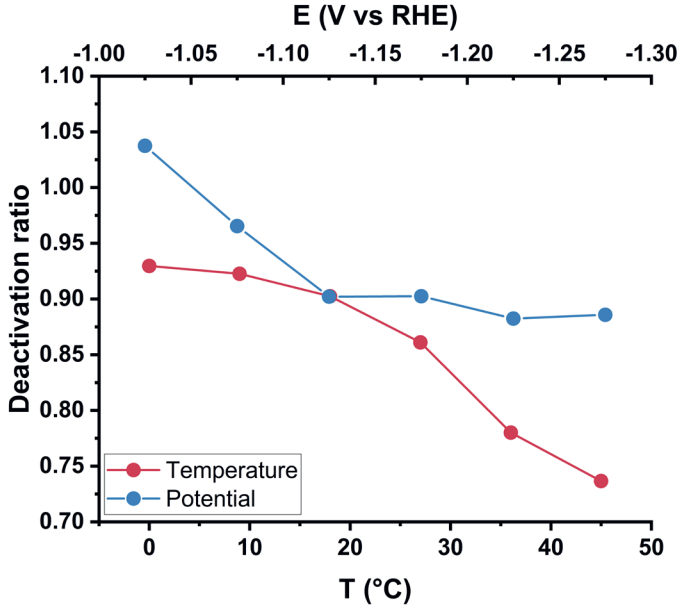


Figure D.8 Deactivation ratio as function of temperature and potential

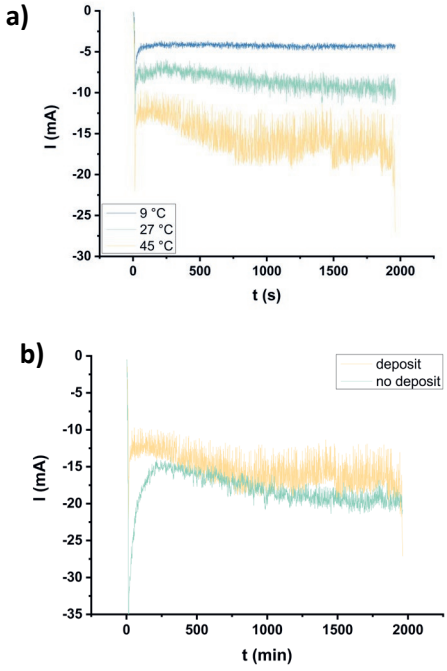


Figure D.9 a) Time dependence of current at different temperatures b) Time dependence of current at 45 °C both with the deposited electrode and the plain Ni electrode

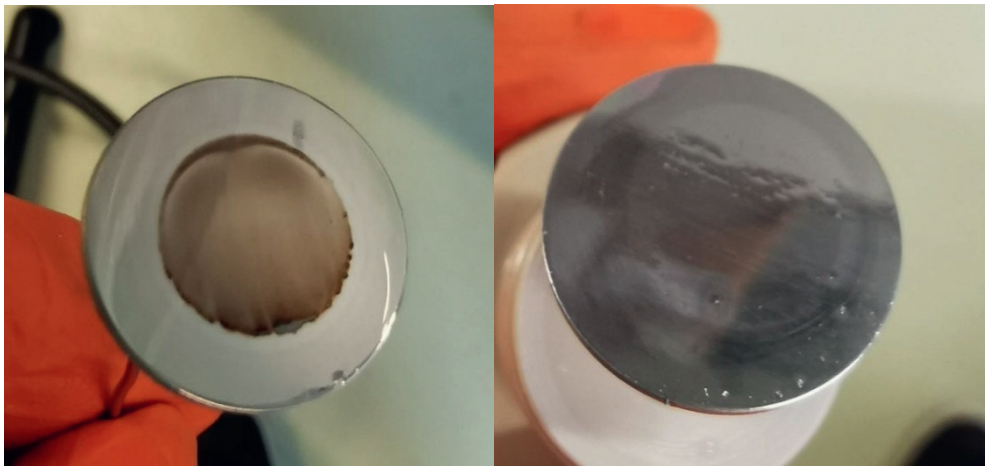


Figure D.10 Photographs of the electrode after a) CO2RR and b) HER showing that the coke only forms after CO2RR

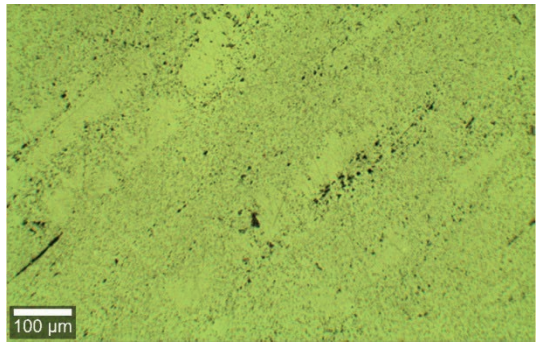


Figure D.11 Microscopy picture of the electrode after CO2RR showing the black deposits on the surface.

D.6 Faradaic efficiency; potential effect

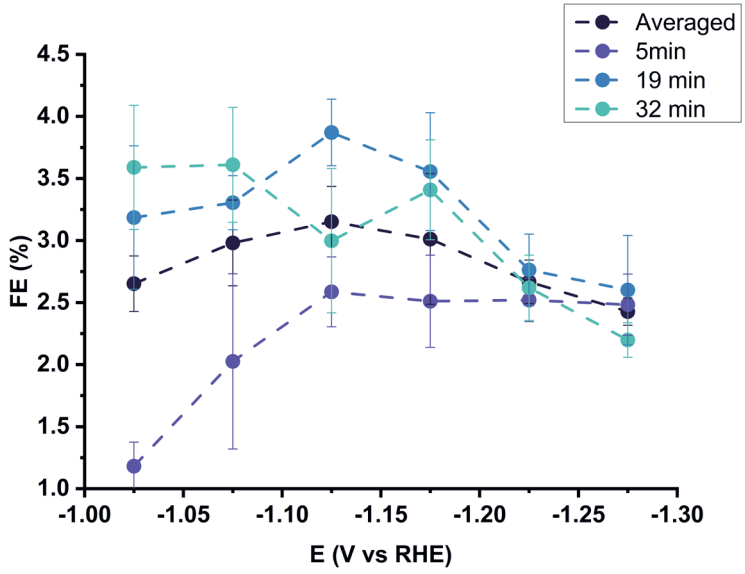


Figure D.12 Faradaic efficiency as function of potential and time on Ni in 0.1 M $KHCO_3$ at 18 °C

D.7 Comparing chain growth probabilities

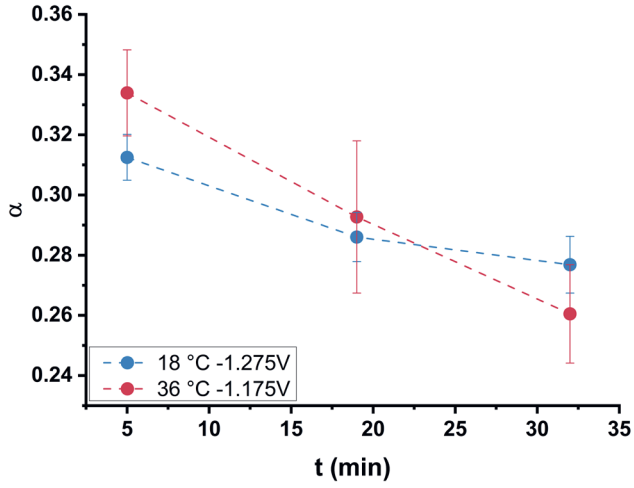


Figure D.13 Chain growth probability in time for 2 different experiments with similar activity showing that higher temperature causes deactivation of the catalyst

D.8 Cation dependence of the deactivation ratio

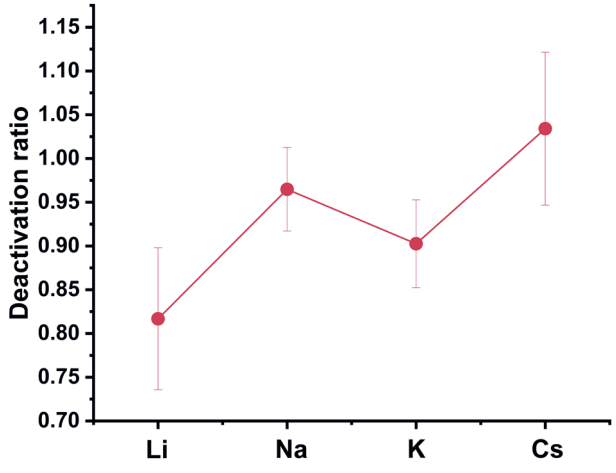


Figure D.13 Deactivation ratio as function of cation identity

D.9 Arrhenius plots

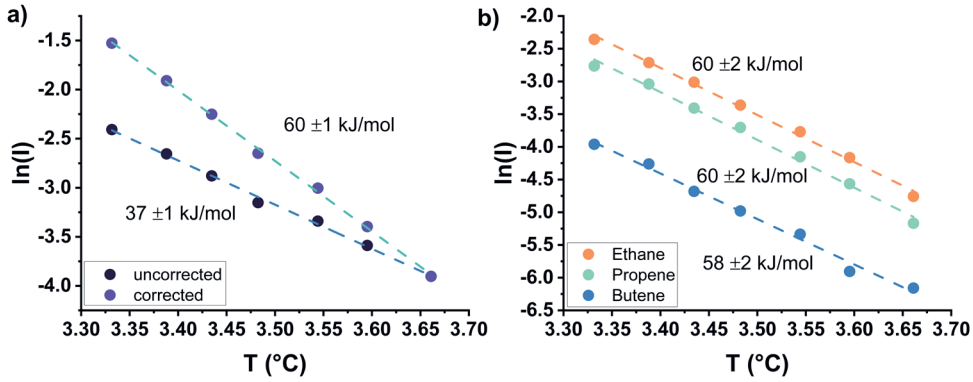


Figure D.15 a) Arrhenius plot after 5 min for methane, b) and for the other hydrocarbons which have similar activation energies

D.10 Relationship chain growth probability and activity

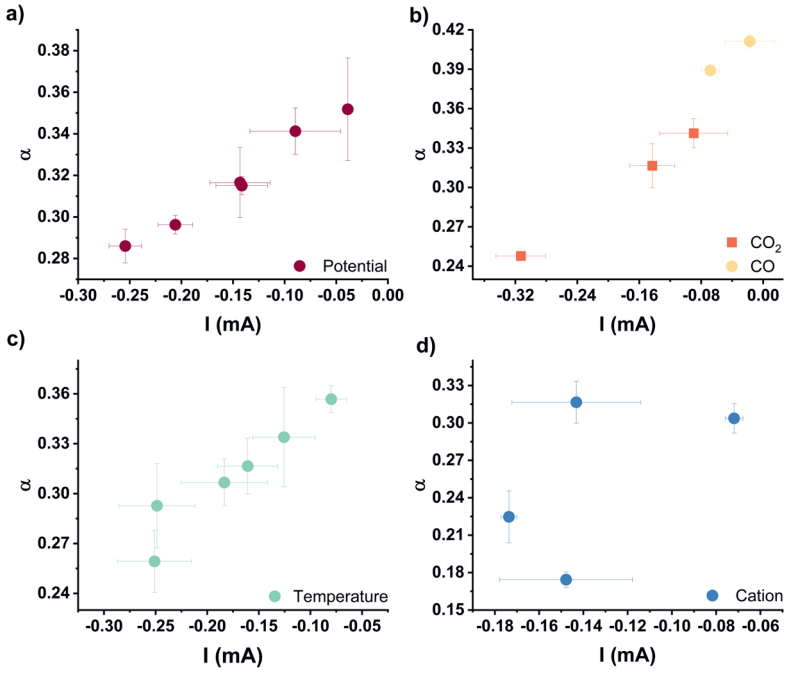


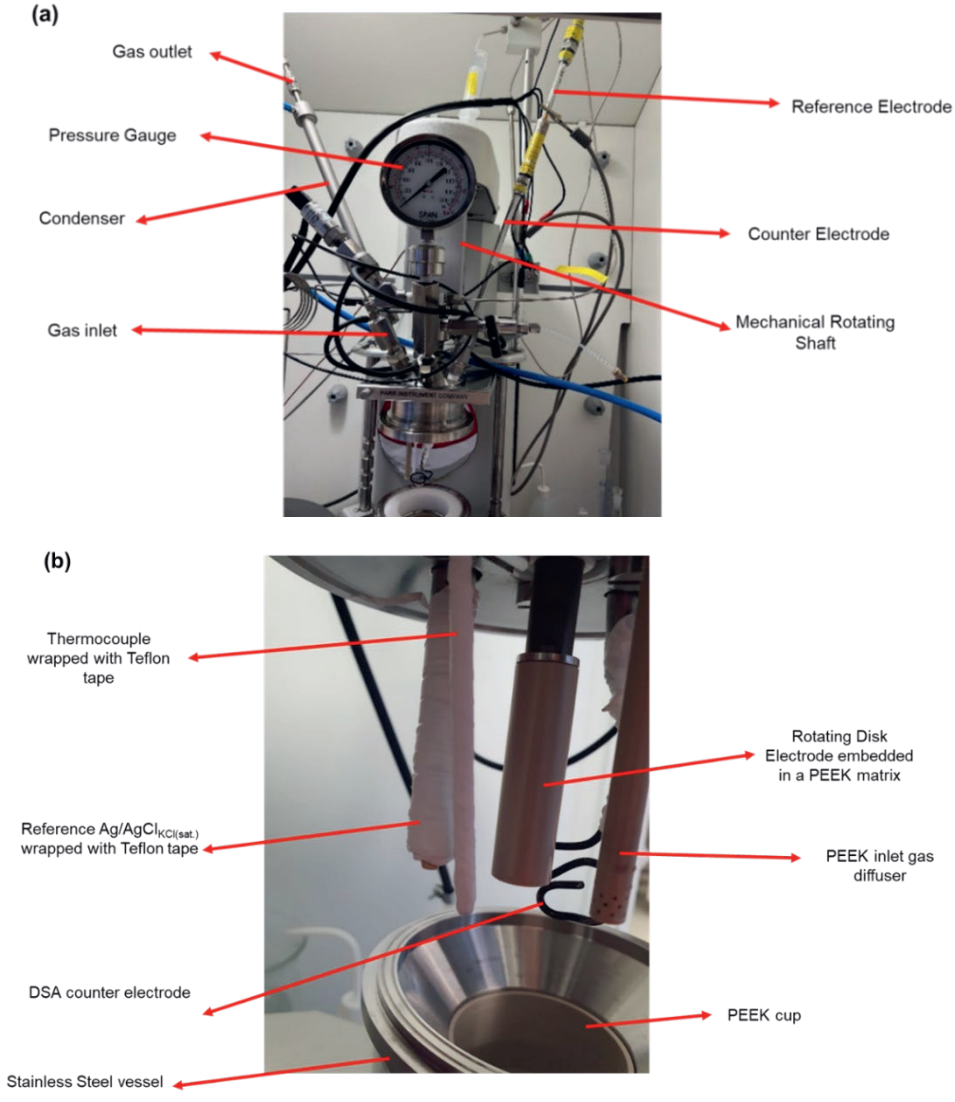
Figure D.16 chain growth probability α plotted vs the activity at different conditions: a) at different potentials (data from figure 3) b) at different anions and with CO or CO_2 as reactant (data from Figure 5) c) at different temperature (data from Figure 1) d) with different cations (data from Figure 4)

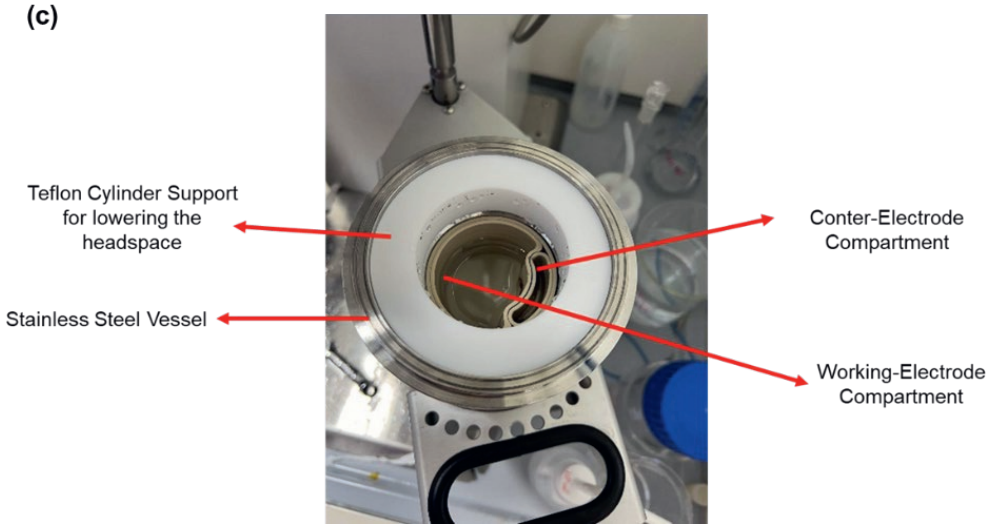
E

Supporting Information to Chapter 6

Design of a Rotating Disk Electrode setup operating under high pressure and temperature: application to CO_2 reduction on gold

E.1 High-pressure and High-temperature Rotating Disk Electrode (RDE) electrochemical cell design




(c)
Teflon Cylinder Support for lowering the headspace
Stainless Steel Vessel
Conter-Electrode Compartment
Working-Electrode Compartment


(d)

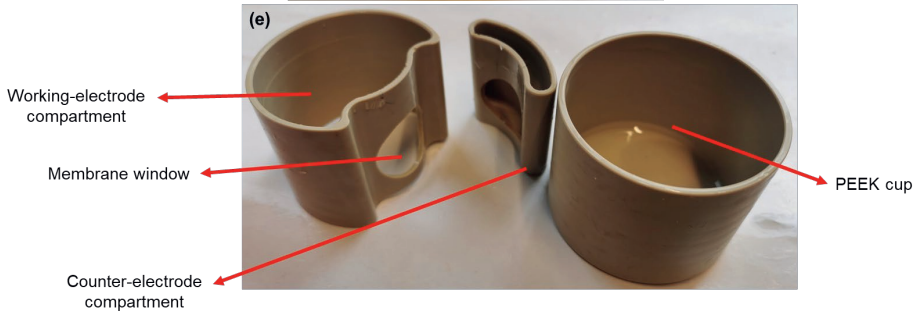

(e)
Working-electrode compartment
Membrane window
Counter-electrode compartment
PEEK cup



Figure E.1 Several pictures from the high-pressure electrochemical rotating disk electrode cell and its components (a) main mechanical parts of the high-pressure cell; (b) electrochemical parts of the high-pressure cell; (c) PEEK cup and membrane separator, and Teflon cylinder in the stainless steel vessel; (d-f) PEEK cup and membrane separator; (g) rotating disk electrode (gold); (h-i) reference electrode, thermocouple, and all other metal surface covered with Teflon tape; and (j) Teflon cylinder used to decrease headspace.

E.2 Cyclic voltammograms of Au and Pt

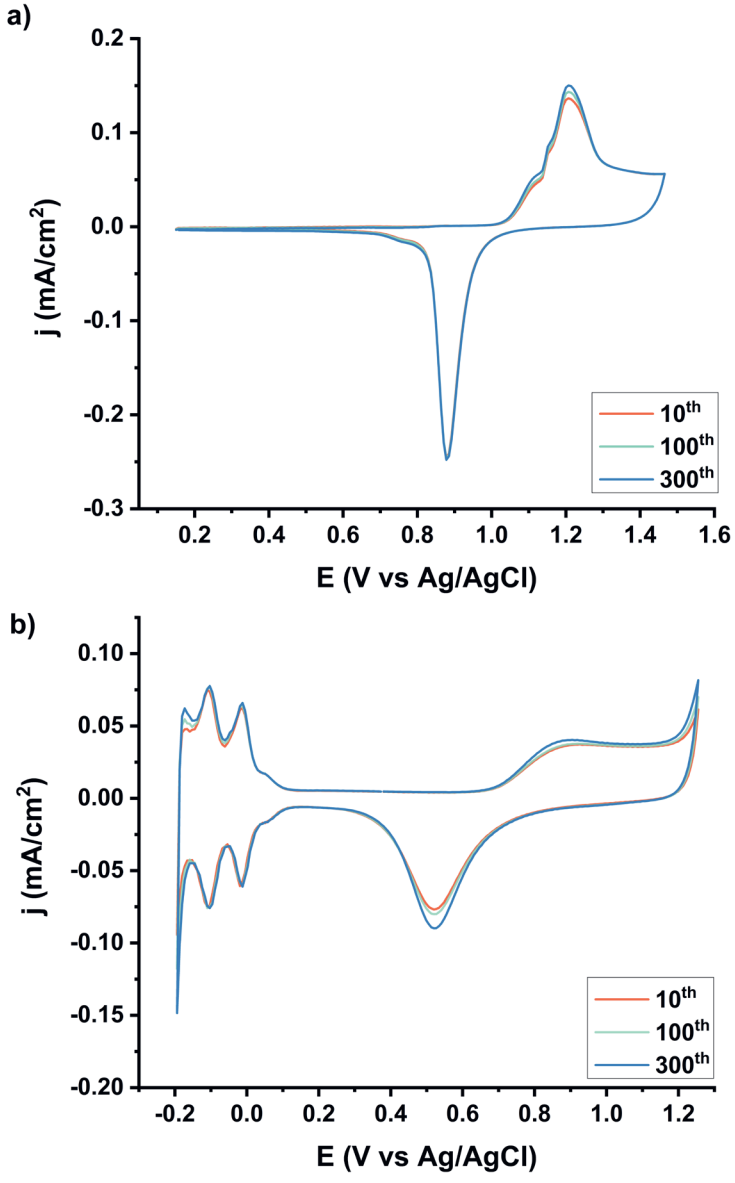


Figure E.2 Cyclic voltammograms of a) Au and b) Pt in 0.1M H_2SO_4 at scan rate of 100 mV/s, 0 barg, and 22°C.

E.3 Gold CVs at temperatures exceeding 100°C

Initially, when the temperature exceeds 100°C, an oxidative peak is observed when the potential is swept to negative potentials in the Au CVs, as shown at 1.10V (Figure E.3a). Additionally, the reduction peaks were drastically suppressed even though the oxidation peaks increased in intensity from 100°C to 145°C, indicating that phenomena other than the surface oxidation of Au were taking place. When the cell was cooled down and the temperature reached 40°C, the Au CV exhibited a marked change from the starting point (Figure E.3b), indicating a significant surface change and/or electrolyte contamination. This CV profile is very similar to the Au CV in the presence of Cl^- species, as shown in Figure E.3b, representing an Au CV recorded in 0.1M H_2SO_4 containing 100 μM KCl. These tests indicate that leakage of Cl species from the Ag/AgCl reference contaminated the electrolyte, and higher leakage is enhanced at higher temperatures.

We have identified that we can extend the operating limit up to 125°C by storing the reference electrode in 0.1 M KCl instead of saturated KCl. By rinsing the reference electrode surface thoroughly with ultrapure water and replacing the Teflon tape covering before each measurement, we did not observe electrodissolution behavior at temperatures up to 125°C. This indicates that Cl^- contamination originates from the liquid junction rather than the internal compartment of the reference electrode. However, at present, we lack sufficient information to ascertain whether very small amounts of chloride also release over time, which can potentially be a problem for long-term measurements.

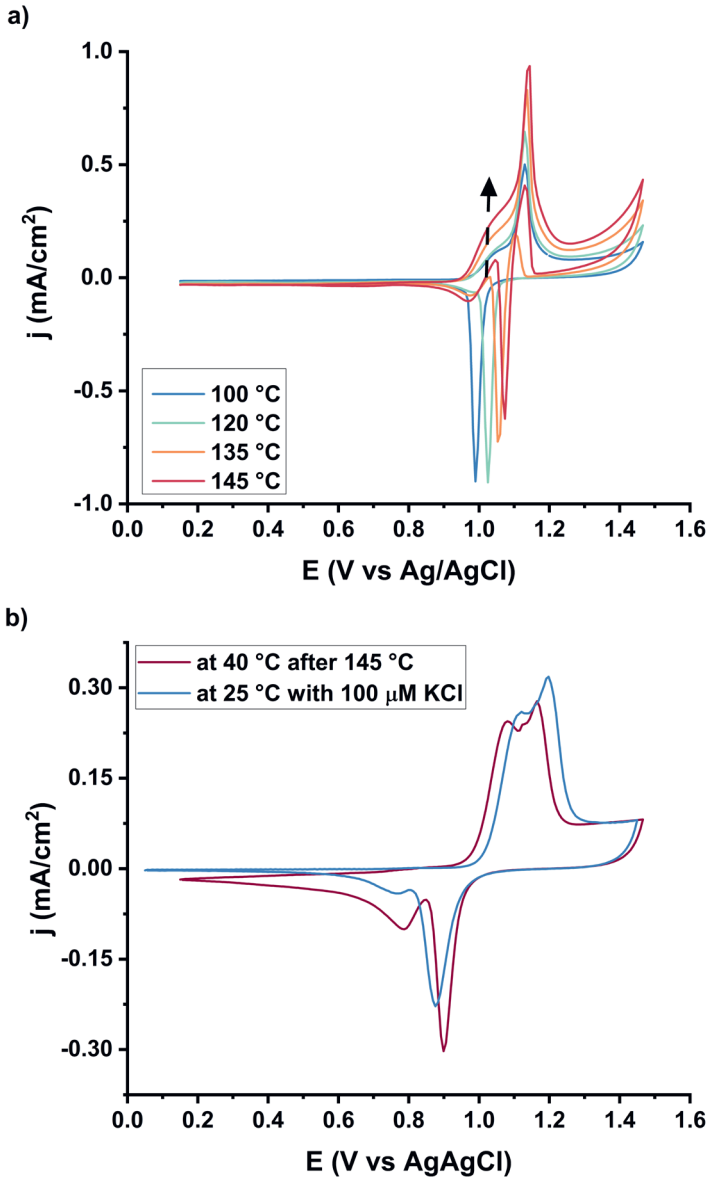


Figure E.3 Cyclic voltammograms in 0.1M H_2SO_4 at different temperatures: (a) from 30°C to 100°C; (b) at 100°C; (c) from 100°C to 145°C; (d) at 145°C; (e) after cooling the temperature down from 145°C to 40°C; (f) and at 25°C in a fresh electrolyte containing 100 µM KCl. All measurements were recorded at 0 barg and with scan rate of 100 mV/s.

E.4 Linear Sweep Voltammogram at different rotation speed

Figure E.5 shows, at different current density scales, the effect of rotation speed on the linear sweep voltammogram (LSV) of CO_2-saturated 0.1 M $KHCO_3$ electrolyte at 0 barg and room temperature for 500, 700, and 1000 rpm (data extracted from Figure 6.4a). At high current densities, the higher the rotation speed (ω), the higher the measured current (Figure E.4a and Figure 6.4a). However, at lower current densities, the opposite is observed in agreement with Goyal et al [1] as shown in Figure 6.4b. They argue that this decrease in current with rotation is due to suppression of HER by improved mass transport of OH^-. We hypothesize that the increase in current with rotation at higher current densities is due to improved bubble removal facilitated by the higher rotation speed.

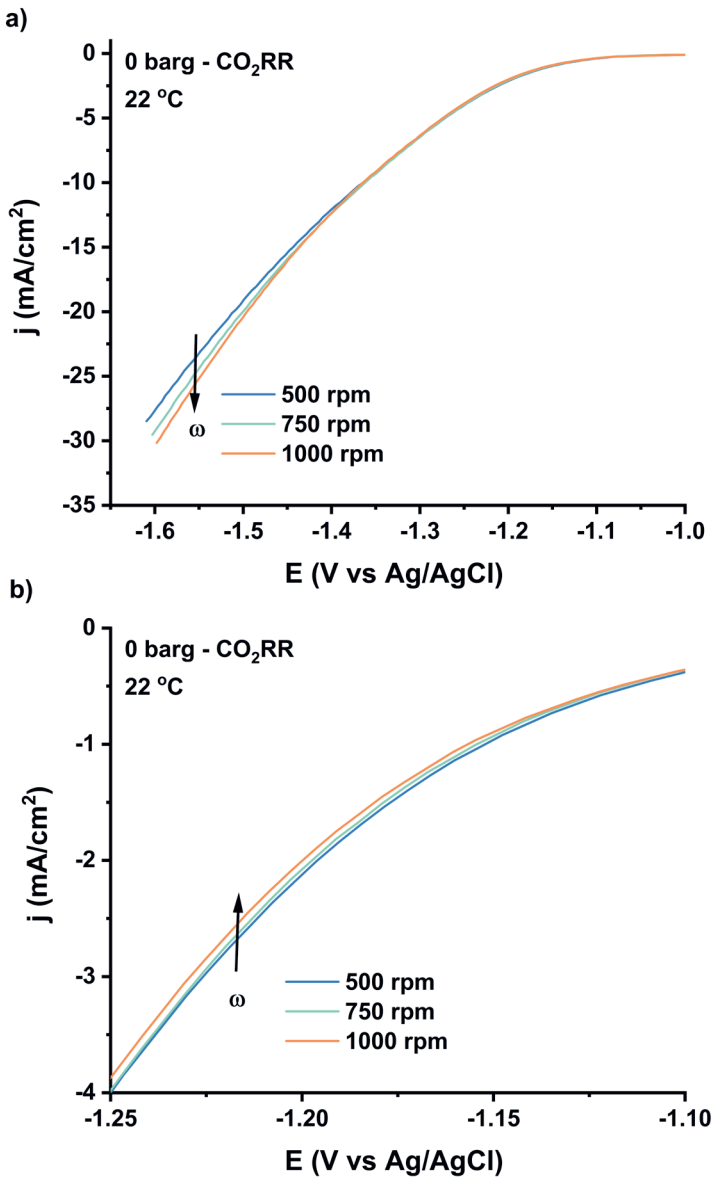


Figure E.4 Linear sweep voltammograms (LSVs) in 0.1 M $KHCO_3$ at different scan rates. b) is zoomed in of a) at lower current densities. LSVs recorded at 0 barg and 22°C.

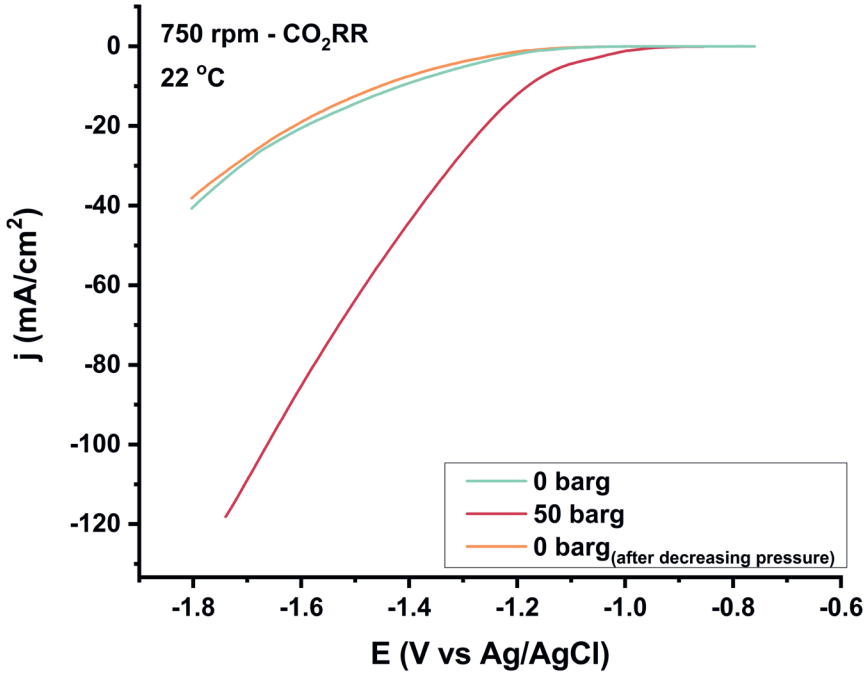


Figure E.5 Comparison of Linear sweep voltammograms (LSVs) in CO_2-saturated 0.1M $KHCO_3$ before increasing pressure, then at 50 barg, and then returning pressure to 0 barg.

Reference

1. Goyal, A., Marcandalli, G., Mints, V. A. & Koper, M. T. M. *J Am Chem Soc* **142**, 4154–4161 (2020).

F

Supporting Information to Chapter 7

Change in the C-C coupling mechanism during CO_2 electroreduction on Cu at elevated temperature and pressure

F.1 Working and reference electrode

Table F.1 Geometric electrode area based on double layer capacitance measurements. A, B, C and D are 1 mm Cu wires of different lengths, while E is a reference Cu disk (8mm diameter) with known geometric surface area

Electrode	A	B	C	D	E
C [µF]	252	139	44.3	21.1	27.8
Area [cm^2]	4.556	2.513	0.8010	0.3815	0.5027

Electrode A was used for experiments at all potentials and 25 °C, -1.3 V vs SHE up to 75 °C, -1.2 V vs SHE and 125 °C,

Electrode B was used for experiments at -1.5/-1.4 V vs SHE and 50 °C, -1.3 V vs SHE and 100 to 125 °C

Electrode C was used for experiments at -1.5 V and 75 °C, -1.4 V vs SHE and 75 to 125 °C, -1.3 V vs SHE and 150 °C

Electrode D was used for experiments at -1.5 V vs SHE above 75 °C

Table F.2 Shift of the Ag/AgCl reference with 0.1 M KCl at different temperatures, compared to SHE(T)

T [°C]	25	50	75	100	125	150
$E^{\mathrm{Ag\|AgCl}}(T)$ [mV]	230.3	214.5	195.9	174.6	151.1	125.5

F.2 Screening temperature, pressure and potential

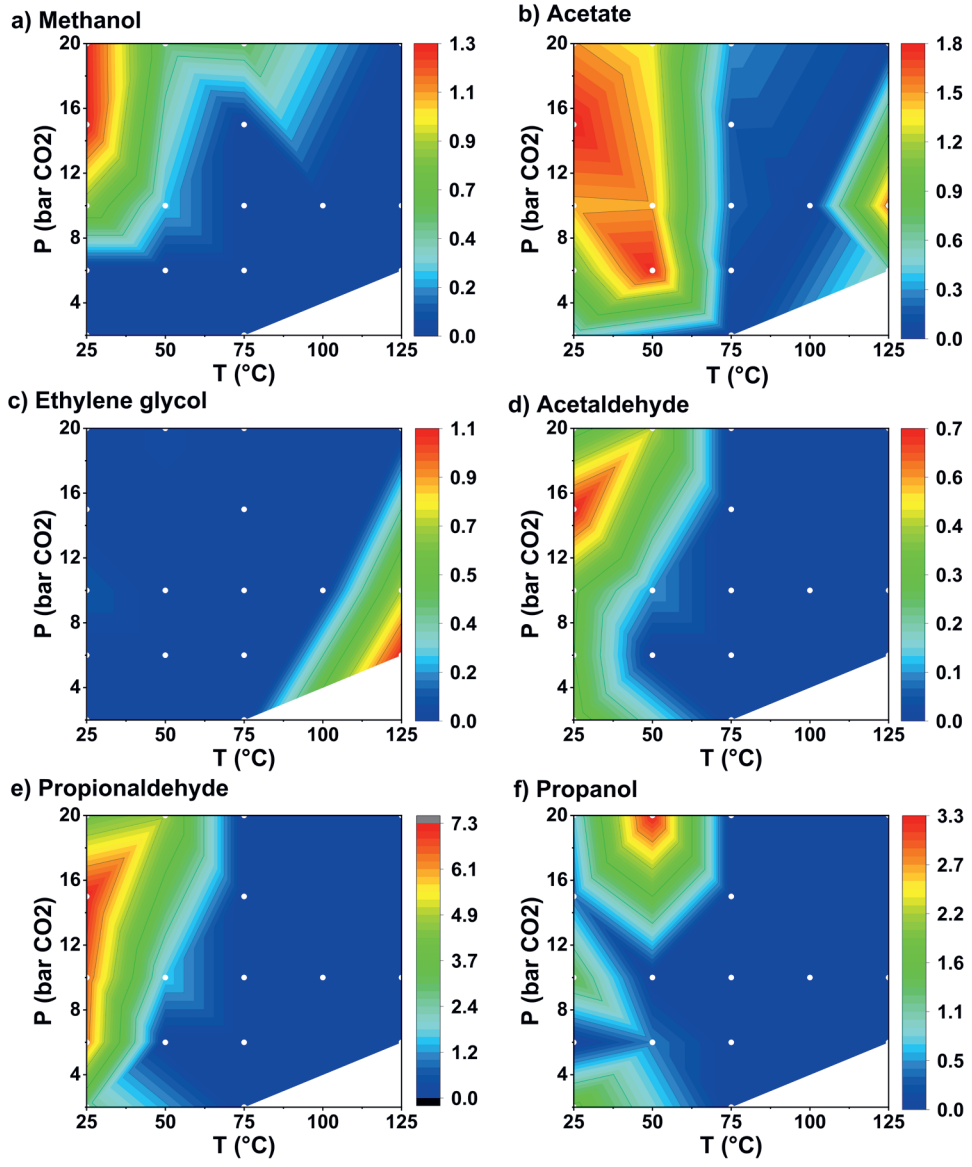


Figure F.1 Faradaic efficiency towards the minor CO2RR products as function of temperature and pressure at -1.4 V vs SHE in 0.2 M $KHCO_3$ with a 50/50 ratio of CO_2 and Ar. The white dots give the measured points and the maps are constructed via interpolation between these points. FE for a) methanol b) acetate c) ethylene glycol d) acetaldehyde e) propionaldehyde and f) 1-propanol

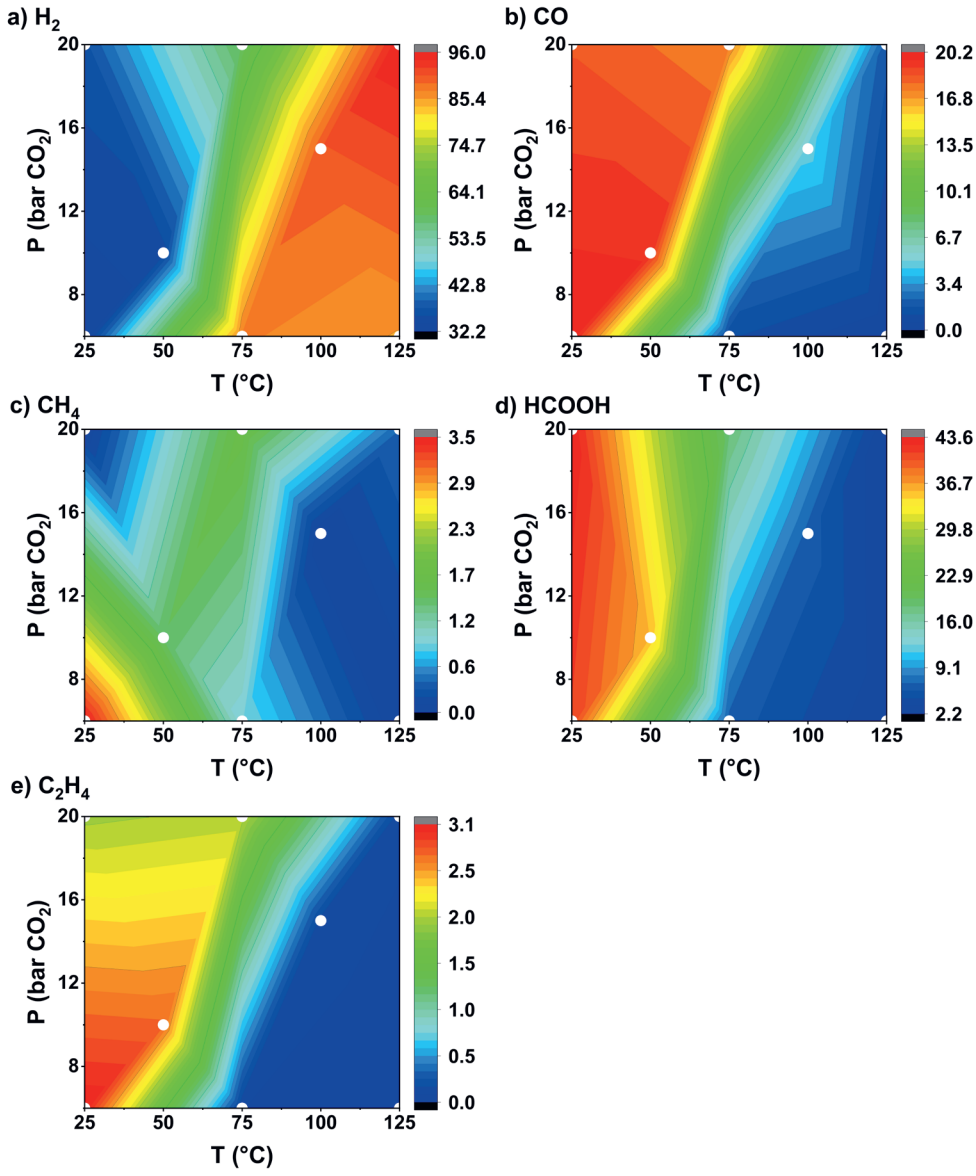


Figure F.2 Faradaic efficiency towards the main CO2RR products as function of temperature and pressure at -1.3 V vs SHE in 0.2 M $KHCO_3$ with a 50/50 ratio of CO_2 and Ar. The white dots give the measured points and the maps are constructed via interpolation between these points. FE for a) hydrogen b) carbon monoxide c) formic acid d) methane e) ethylene and f) ethanol

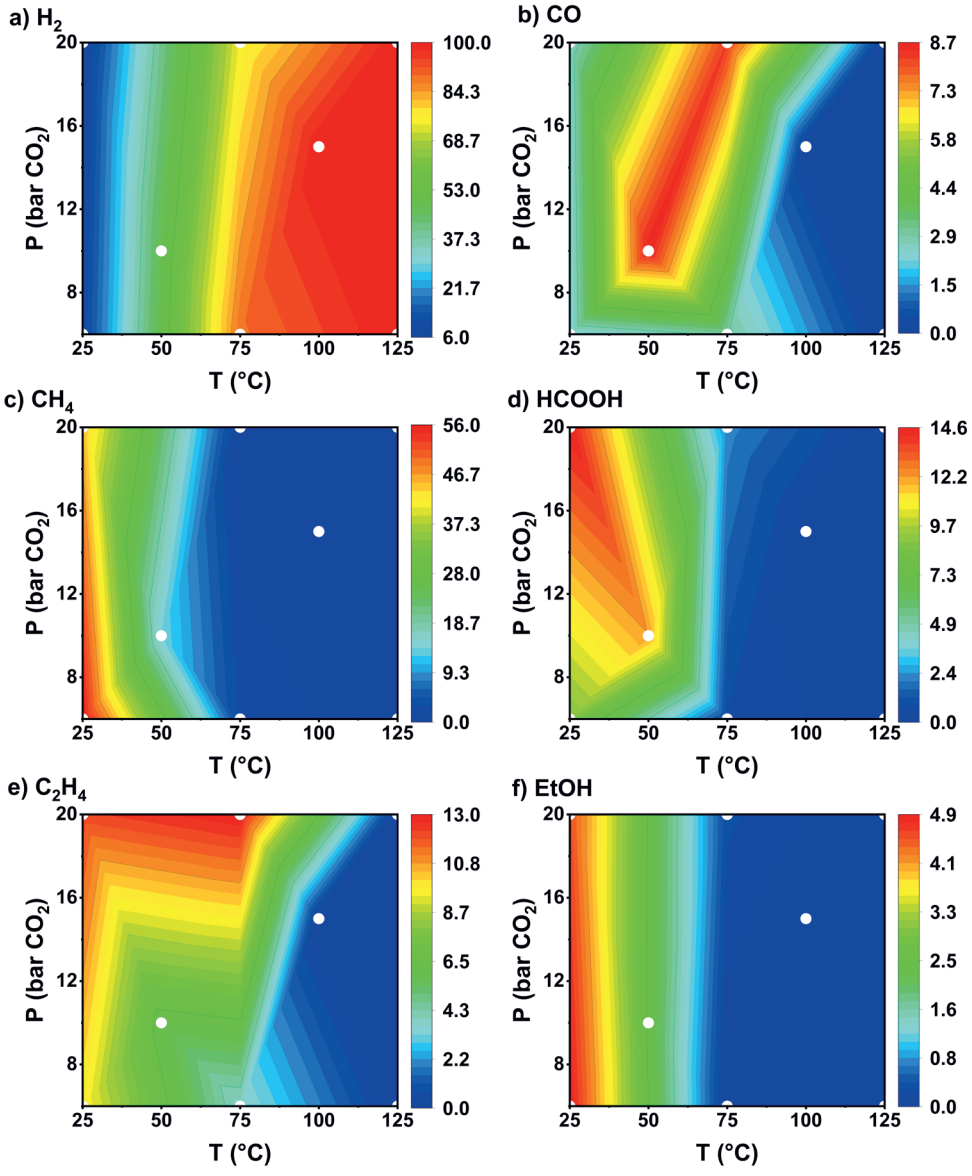


Figure F.3 Faradaic efficiency towards the main CO2RR products as function of temperature and pressure at -1.5 V vs SHE in 0.2 M $KHCO_3$ with a 50/50 ratio of CO_2 and Ar. The white dots give the measured points and the maps are constructed via interpolation between these points. FE for a) hydrogen b) carbon monoxide c) formic acid d) methane e) ethylene and f) ethanol

F.3 Instable currents at elevated temperatures

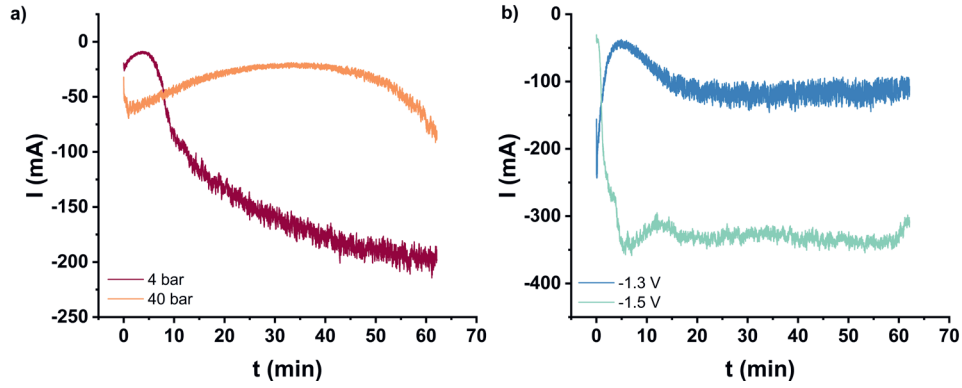


Figure F.4 Current as function of time for a) 4 and 40 bar at -1.5 V vs SHE at 75 °C and b) 24 bar at 125 °C at -1.3 V and -1.5 vs SHE. This illustrates that at elevated temperatures the current is not stable, especially at low pressures as seen in a). In b) the typical current profile at 125 °C and -1.3 V is observed, where the current is unstable in the first 20 minutes and first decreases and then increases again after which it stabilizes. It also shows the instability at higher overpotentials, where even the smallest electrode goes to currents above -300 mA, while at the start is was only -30 mA.

F.4 Switching mechanism at high pressure and high temperature

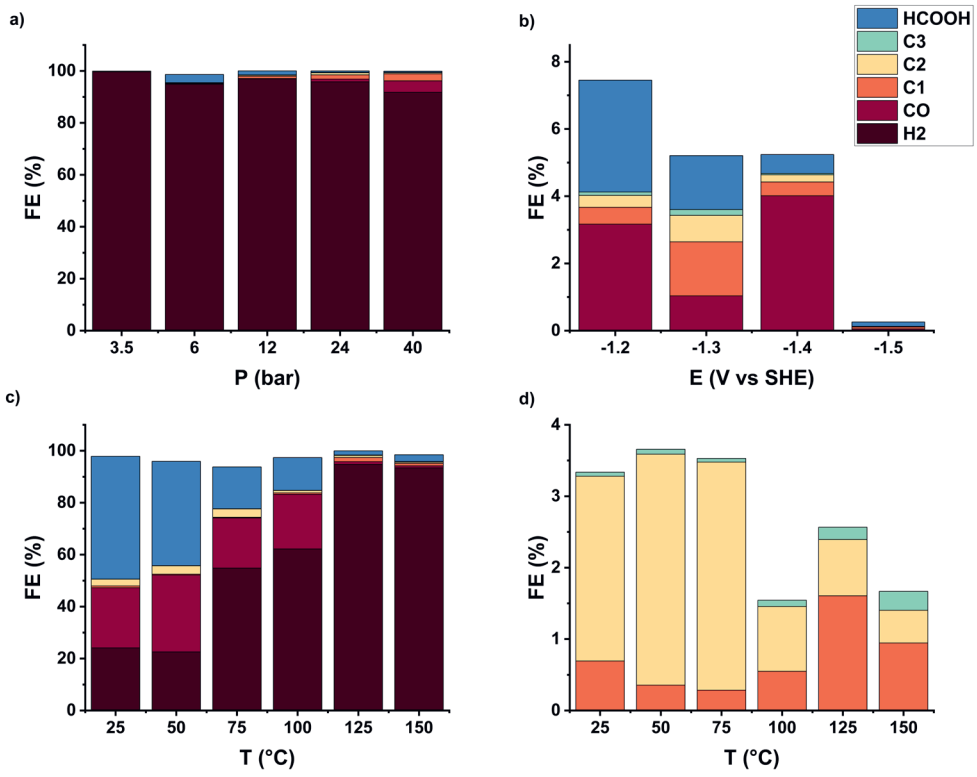


Figure F.5 Faradaic efficiencies for the CO2RR reduction as function of a) pressure at 24 bar and -1.3 V vs SHE b) potential at 24 bar and 125 °C and c and d) temperature at 24 bar and -1.3 V vs SHE. a) and c) show total FE. b) shows the CO2RR products with the remaining FE being H2 and d) shows only the hydrocarbons

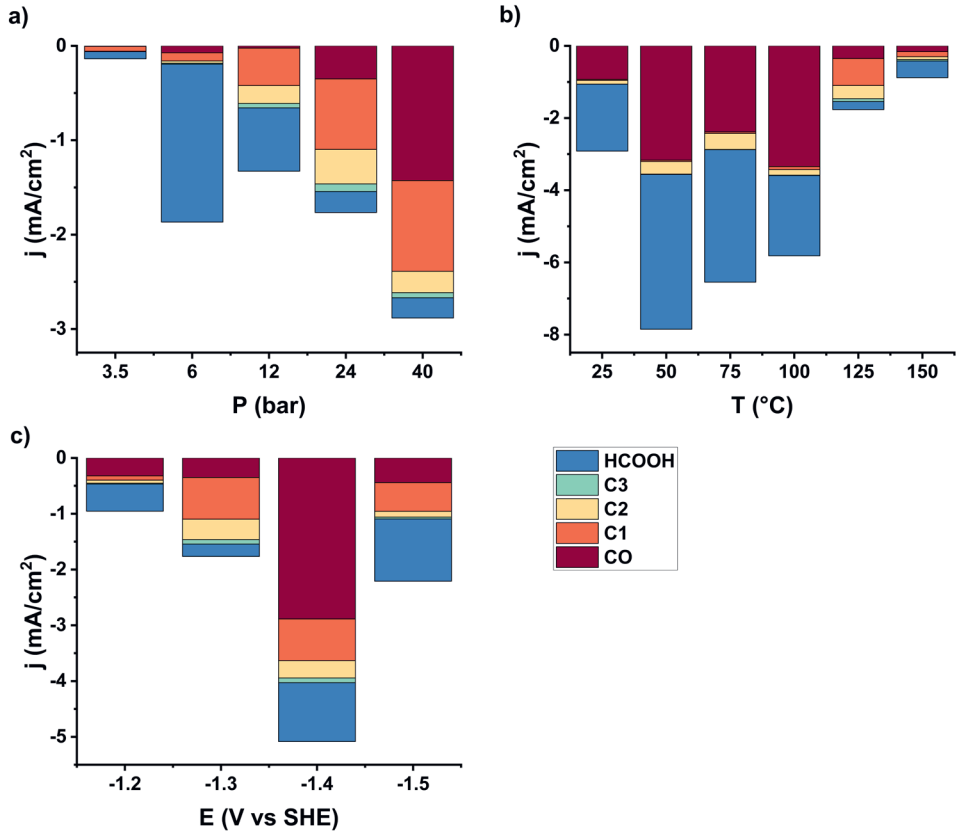


Figure F.6 Partial current density for the CO2RR products as function of a) pressure at 24 bar and -1.3 V vs SHE b) temperature at 24 bar and -1.3 V vs SHE c) potential at 24 bar and 125 °C.

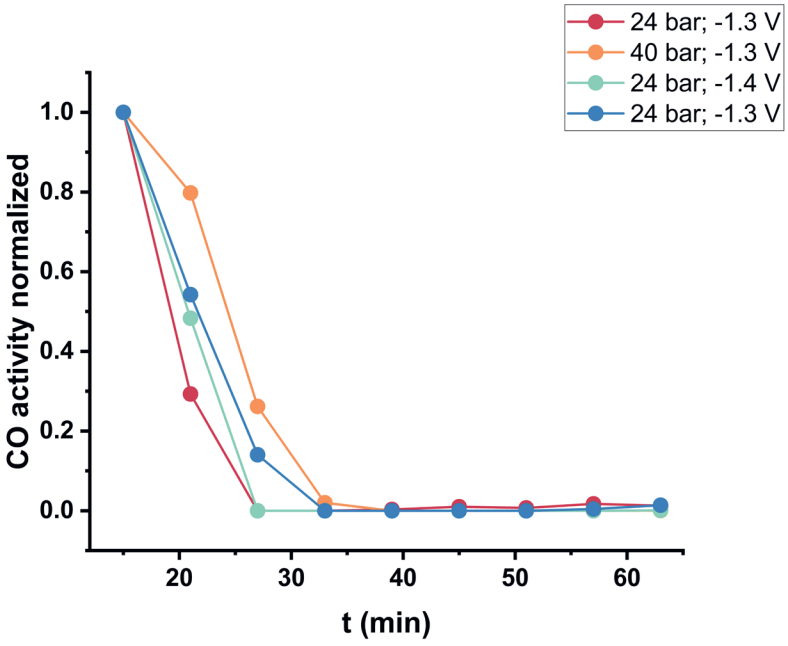


Figure F.7 The normalized CO activity as function of time for several conditions, all at 125 °C. This illustrates that CO is only produced at the start of the experiment as it decreases rapidly and from 32 min the activity is 0

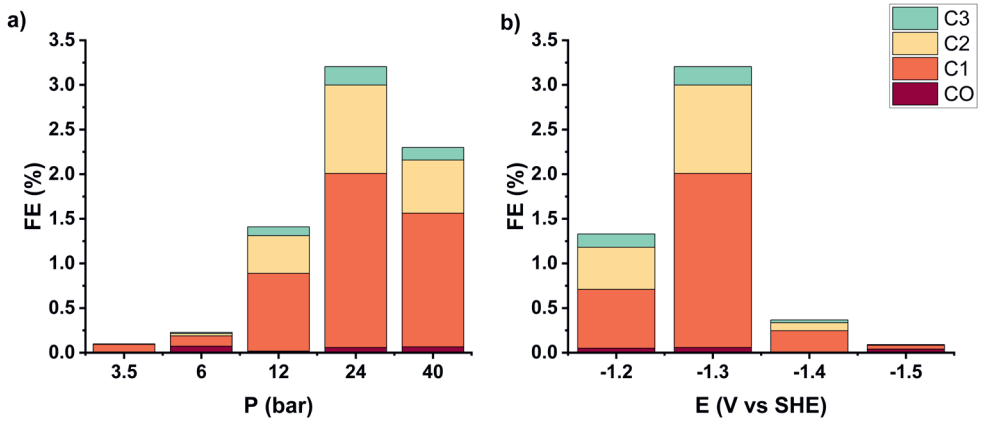


Figure F.8 Partial current density for the CO2RR products at function of as function of a) pressure at 24 bar and -1.3 V vs SHE b) temperature at 24 bar and -1.3 V vs SHE, but only taking into account the gaseous products during the last 30 minutes of the experiment.

Table F.4 Chain growth probability as function of temperature, pressure and potential

Temperature (°C)	Pressure (bar)	Potential (V vs SHE)	Chain growth probability
75	24	-1.3	0.22
100	24	-1.3	0.30
125	24	-1.3	0.33
150	24	-1.3	0.41
125	12	-1.3	0.35
125	40	-1.3	0.30
125	24	-1.2	0.41
125	24	-1.4	0.34
125	24	-1.5	0.31

F.5 Effect of temperature on the CO2RR at -1.5 V vs SHE

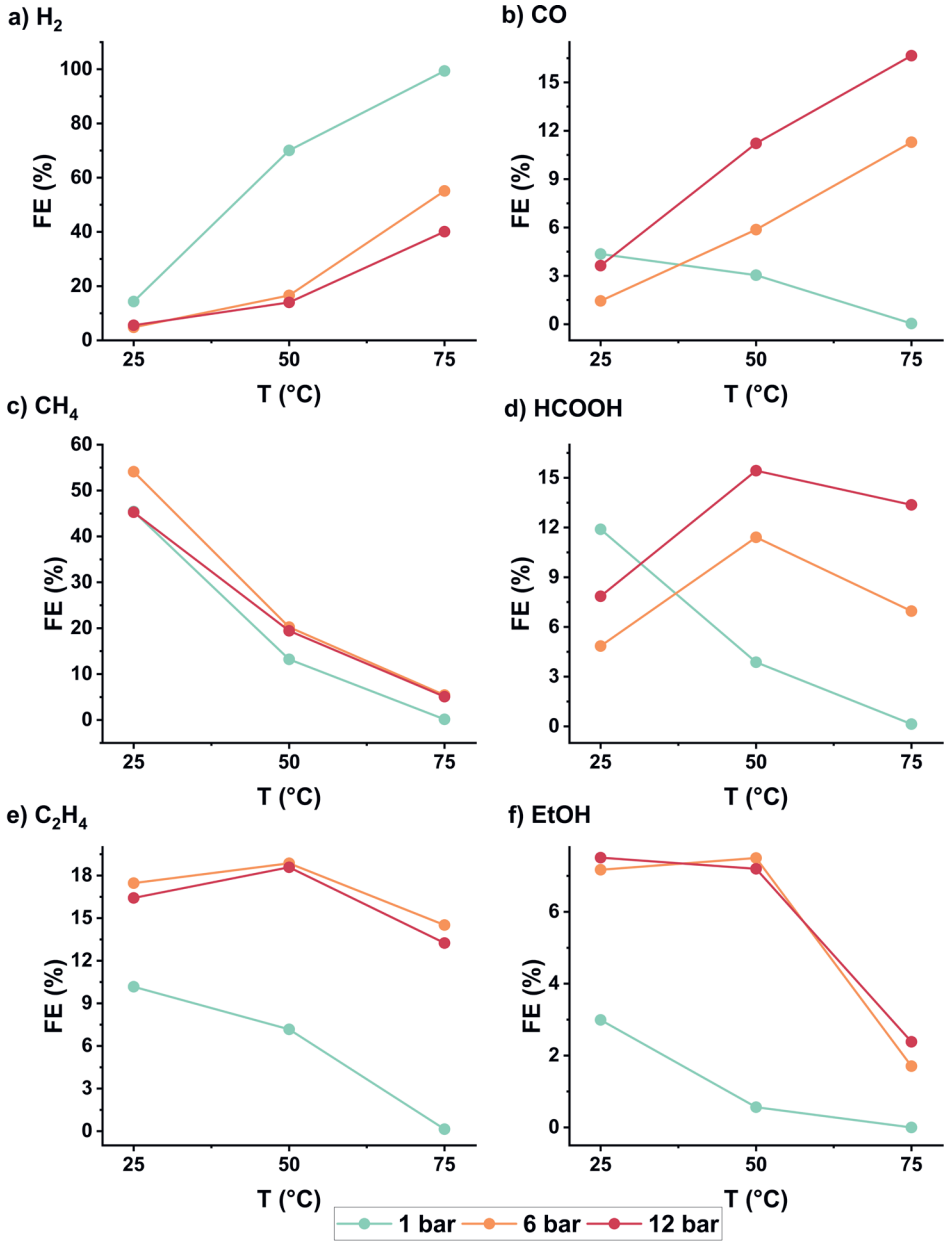


Figure F.9 Faradaic efficiency towards the main CO2RR products at different pressures as function of temperature at -1.5 V vs SHE in 0.2 M $KHCO_3$. FE for a) hydrogen b) carbon monoxide c) formic acid d) methane e) ethylene and f) ethanol

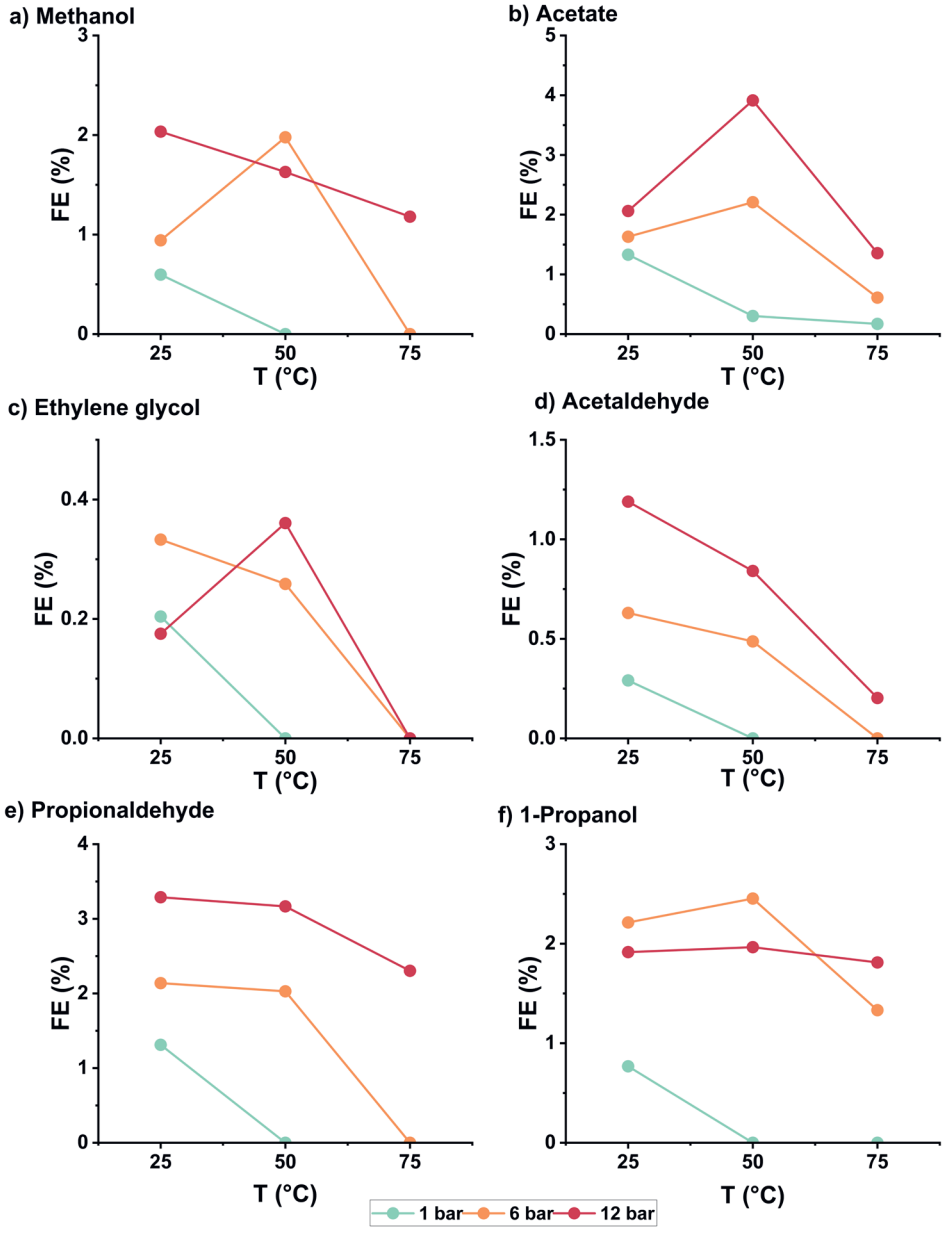


Figure F.10 Faradaic efficiency towards the minor CO2RR products at different pressures as function of temperature at -1.5 V vs SHE in 0.2 M $KHCO_3$. FE for a) methanol b) acetate c) ethylene glycol d) acetaldehyde e) propionaldehyde f) 1-Propanol

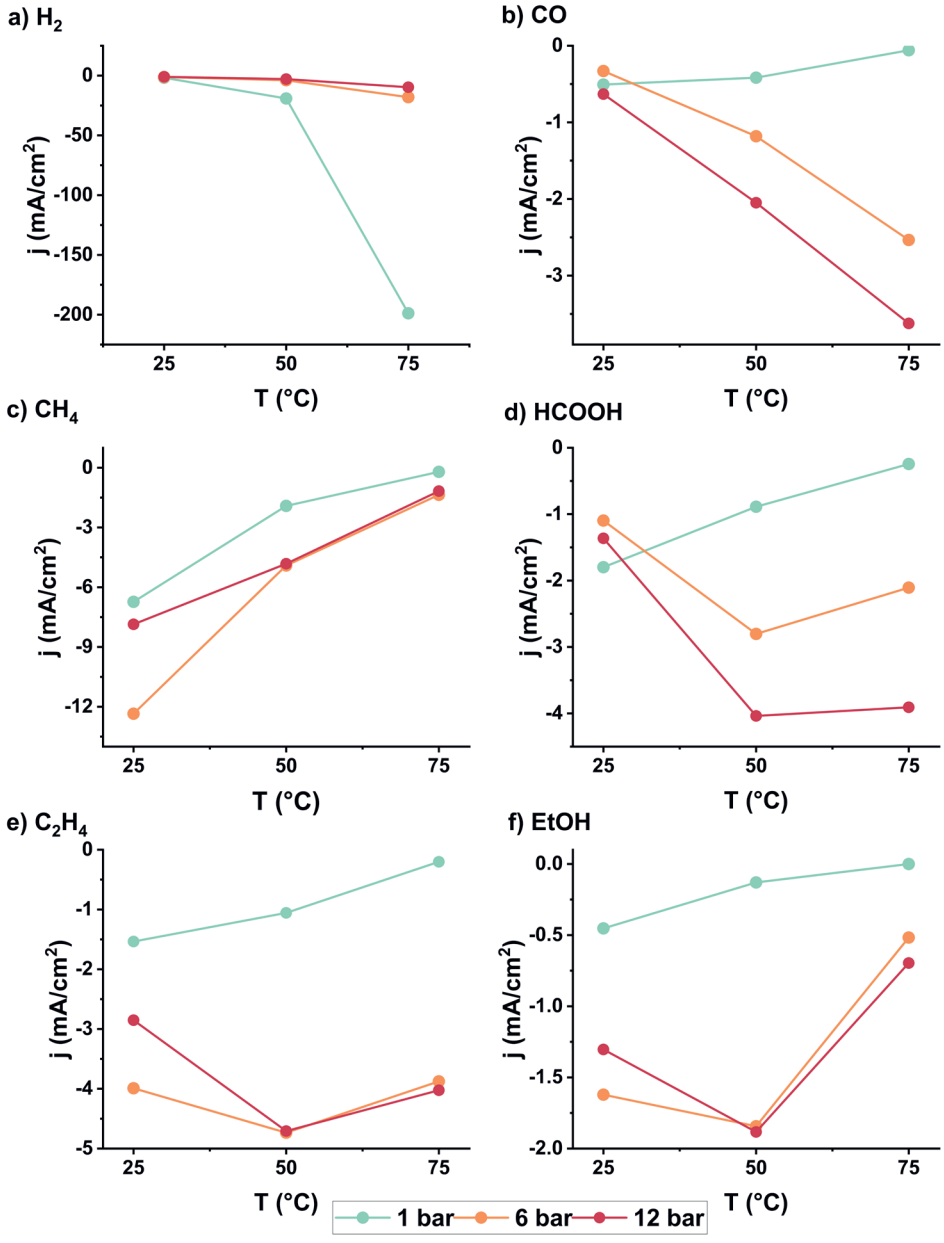


Figure F.11 Partial current density towards the main CO2RR products at different pressures as function of temperature at -1.5 V vs SHE in 0.2 M $KHCO_3$. FE for a) hydrogen b) carbon monoxide c) formic acid d) methane e) ethylene and f) ethanol

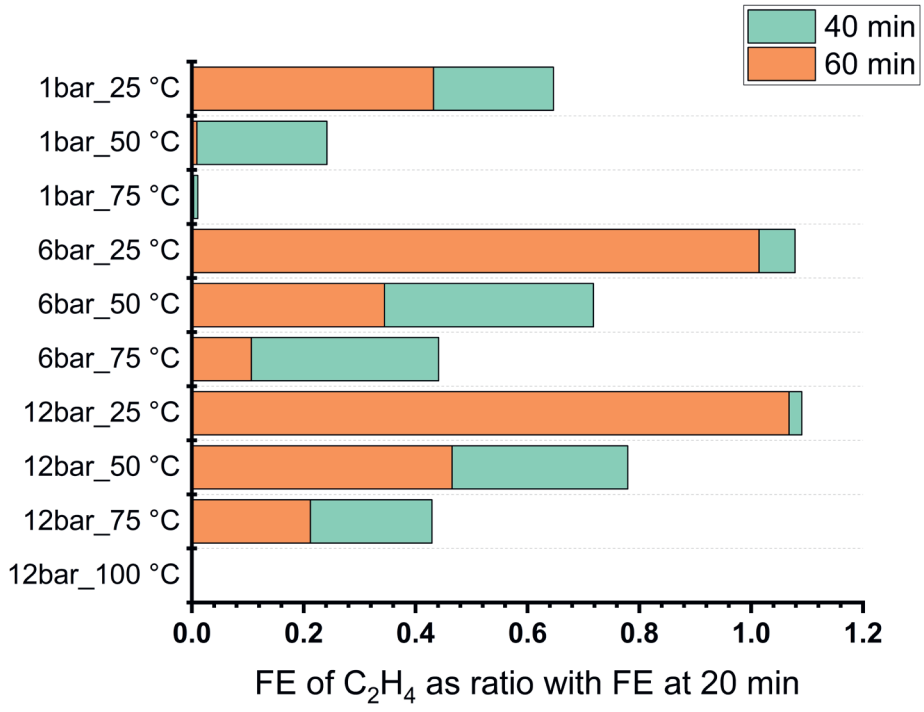


Figure F.12 Stability as function of temperature and pressure. Stability is here defined as the FE that remains after 40 and 60 minutes compared to the FE at 20 minutes at a certain condition.

F.6 Effect of pressure on the CO2RR at -1.5 V vs SHE

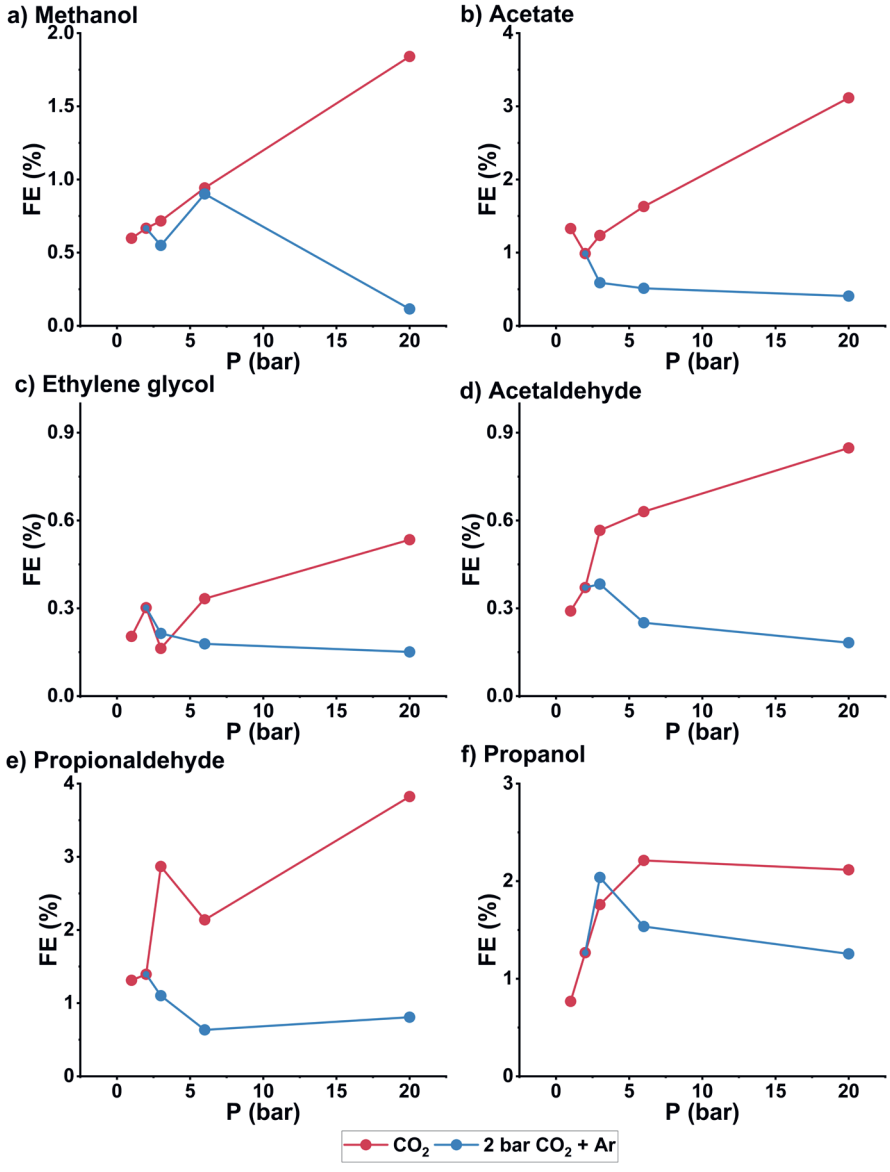


Figure F.13 Faradaic efficiency towards the minor CO2RR products as function of CO_2 and total pressure at -1.5 V vs SHE in 0.2 M $KHCO_3$ at 25 °C. Red lines are performed in pure CO_2 and blue lines are at 2 bar of CO_2 and pressure is increased with Ar. FE for a) methanol b) acetate c) ethylene glycol d) acetaldehyde e) propionaldehyde and f) 1-propanol

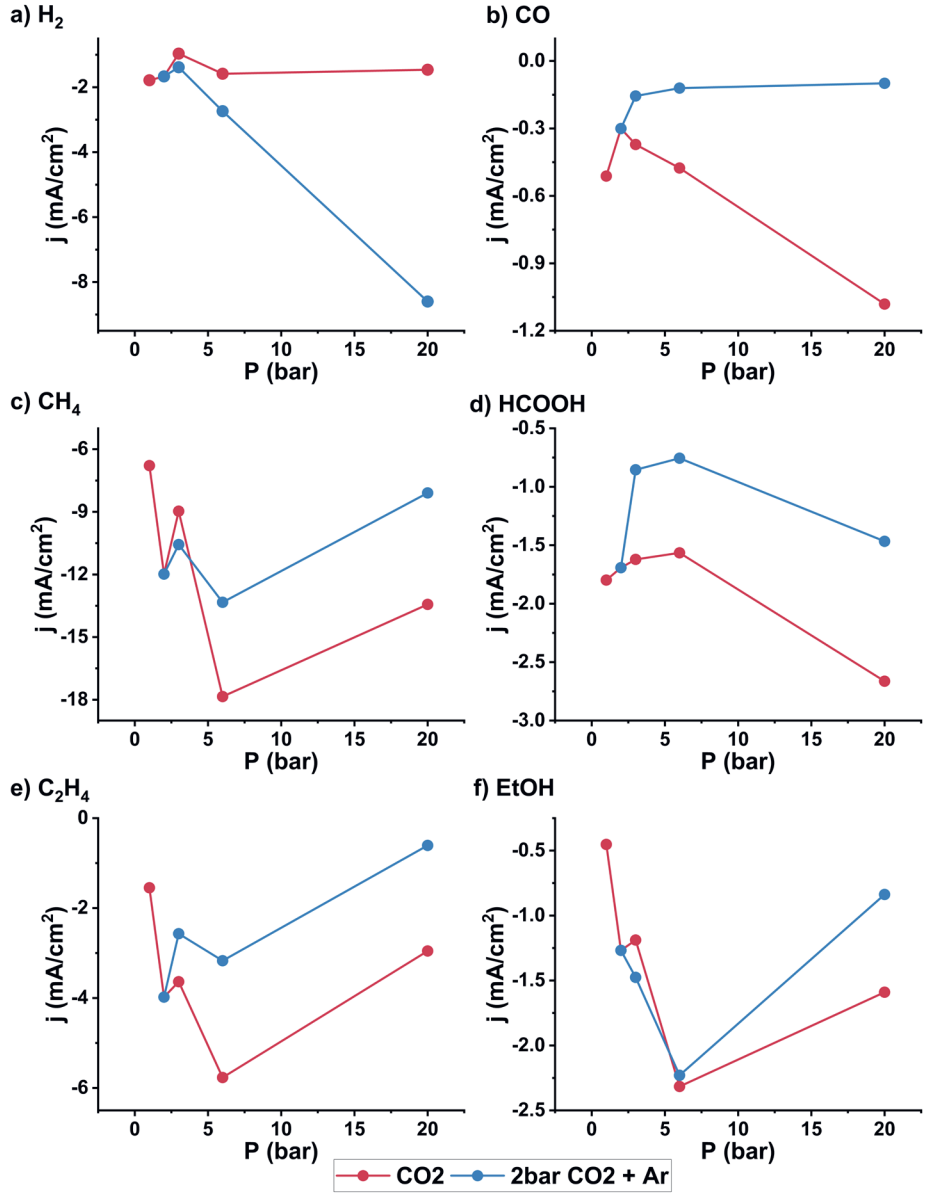


Figure F.14 Partial current density towards the main CO2RR products as function of CO_2 and total pressure at -1.5 V vs SHE in 0.2 M $KHCO_3$ at 25 °C. Red lines are performed in pure CO_2 and blue lines are at 2 bar of CO_2 and pressure is increased with Ar. FE for a) hydrogen b) carbon monoxide c) formic acid d) methane e) ethylene and f) ethanol

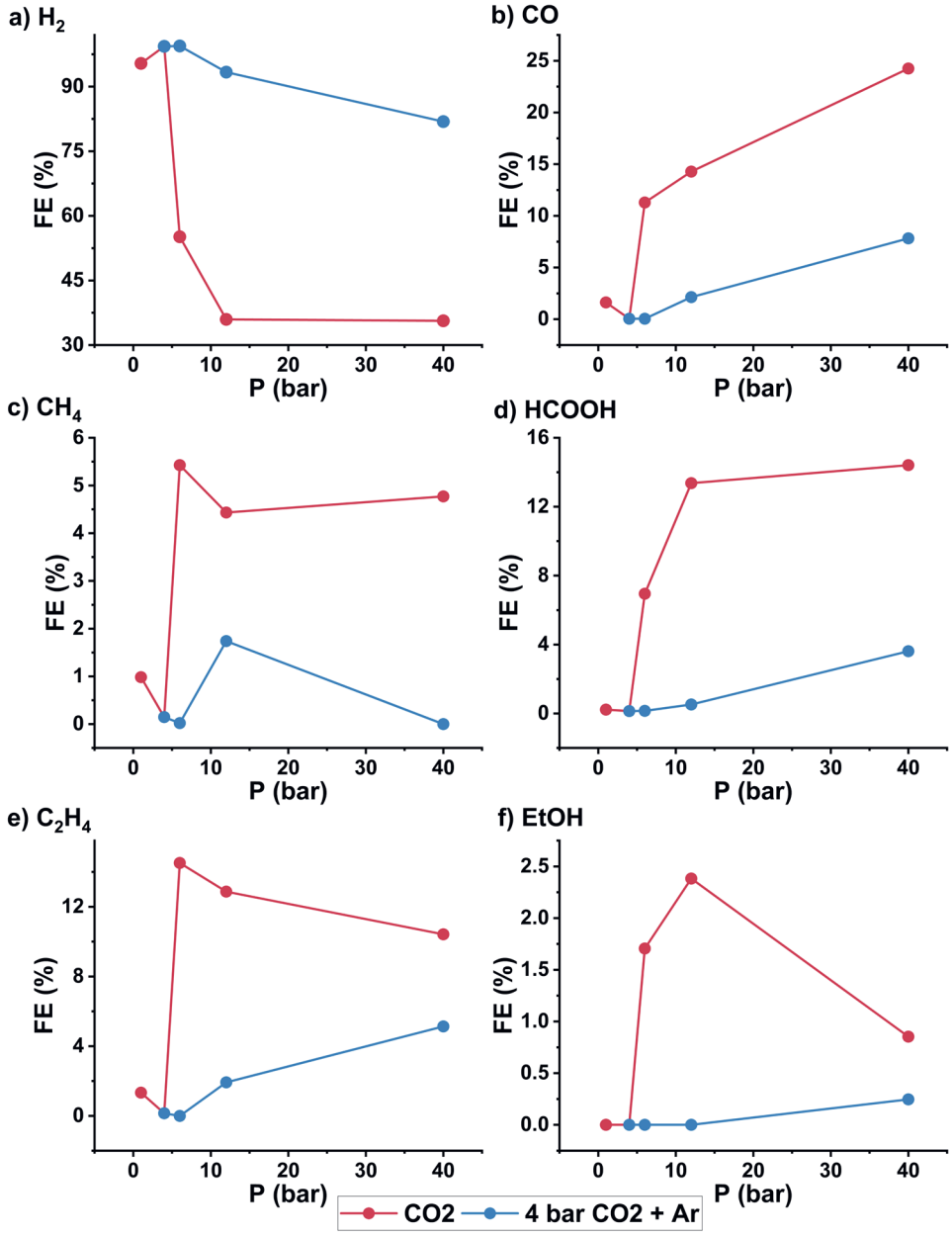


Figure F.15 Faradaic efficiency towards the main CO2RR products as function of CO_2 and total pressure at -1.5 V vs SHE in 0.2 M $KHCO_3$ at 75 °C. Red lines are performed in pure CO_2 and blue lines are at 2 bar of CO_2 and pressure is increased with Ar. FE for a) hydrogen b) carbon monoxide c) formic acid d) methane e) ethylene and f) ethanol

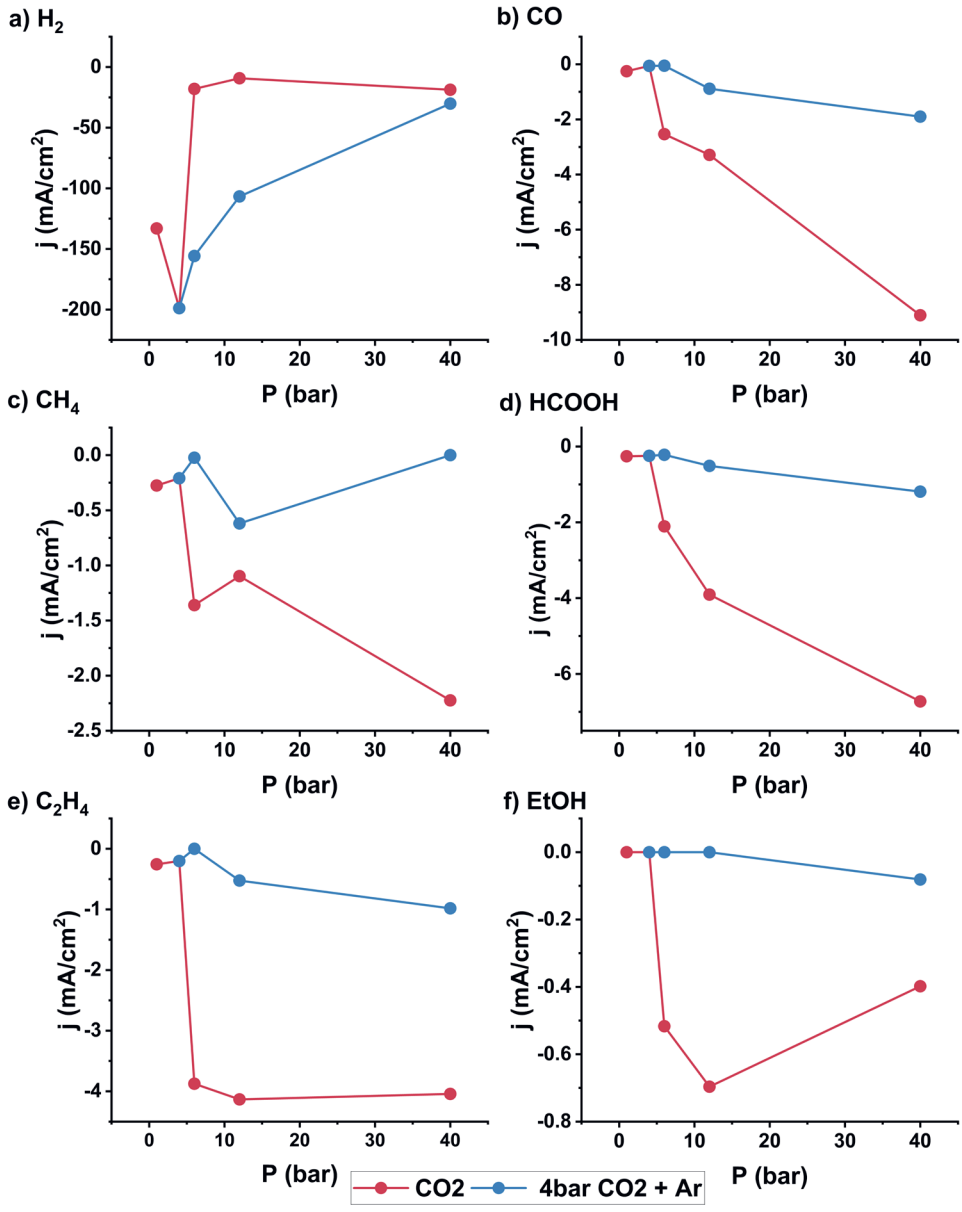


Figure F.16 Partial current densities towards the main CO2RR products as function of CO_2 and total pressure at -1.5 V vs SHE in 0.2 M $KHCO_3$ at 75 °C. Red lines are performed in pure CO_2 and blue lines are at 2 bar of CO_2 and pressure is increased with Ar. FE for a) hydrogen b) carbon monoxide c) formic acid d) methane e) ethylene and f) ethanol

The behavior of CO2RR with increasing CO_2 pressure at 75 °C as shown in Figure F.15 is similar for the C2+ products as at room temperature (Figure 7.5). An initial increase in pressure is needed as at low pressures and high temperatures no significant C2+ products are observed due to the instability of the Cu as discussed above. At 6 bar there is a sharp rise in C2+ activity (Figure S16) and selectivity, which slowly decreases with further increase of pressure. For the simple C1 products CO and HCOOH, the behavior at 75 °C is a bit different than at 25 °C, as the FE towards these products increases with increasing CO_2 pressure. At 25 °C, the FEs first decrease, but at 75 °C this is not possible as they already start near 0 at low pressures. Moreover, for most CO2RR products, the selectivity increases even when the pressure is increased with only Ar, contrary to the case at 25 °C.

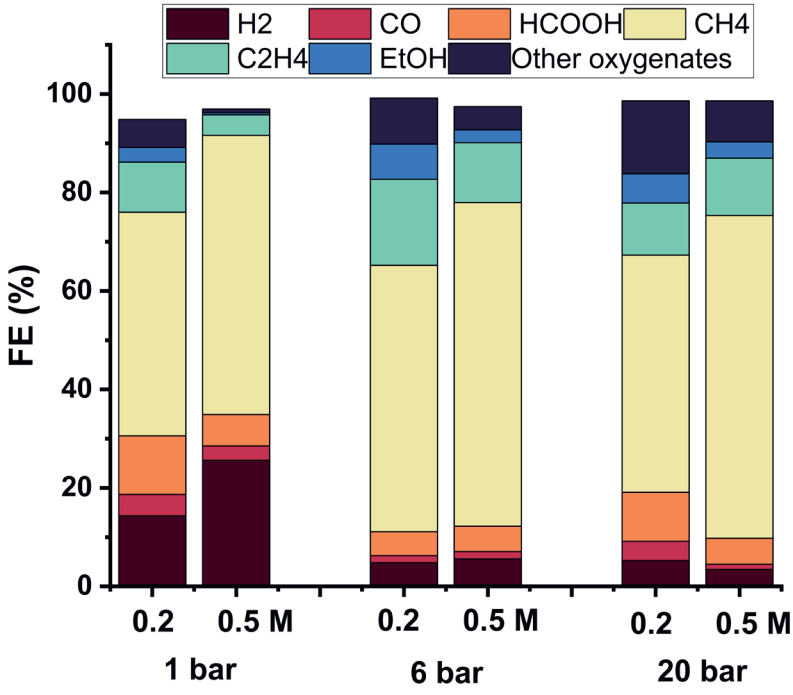
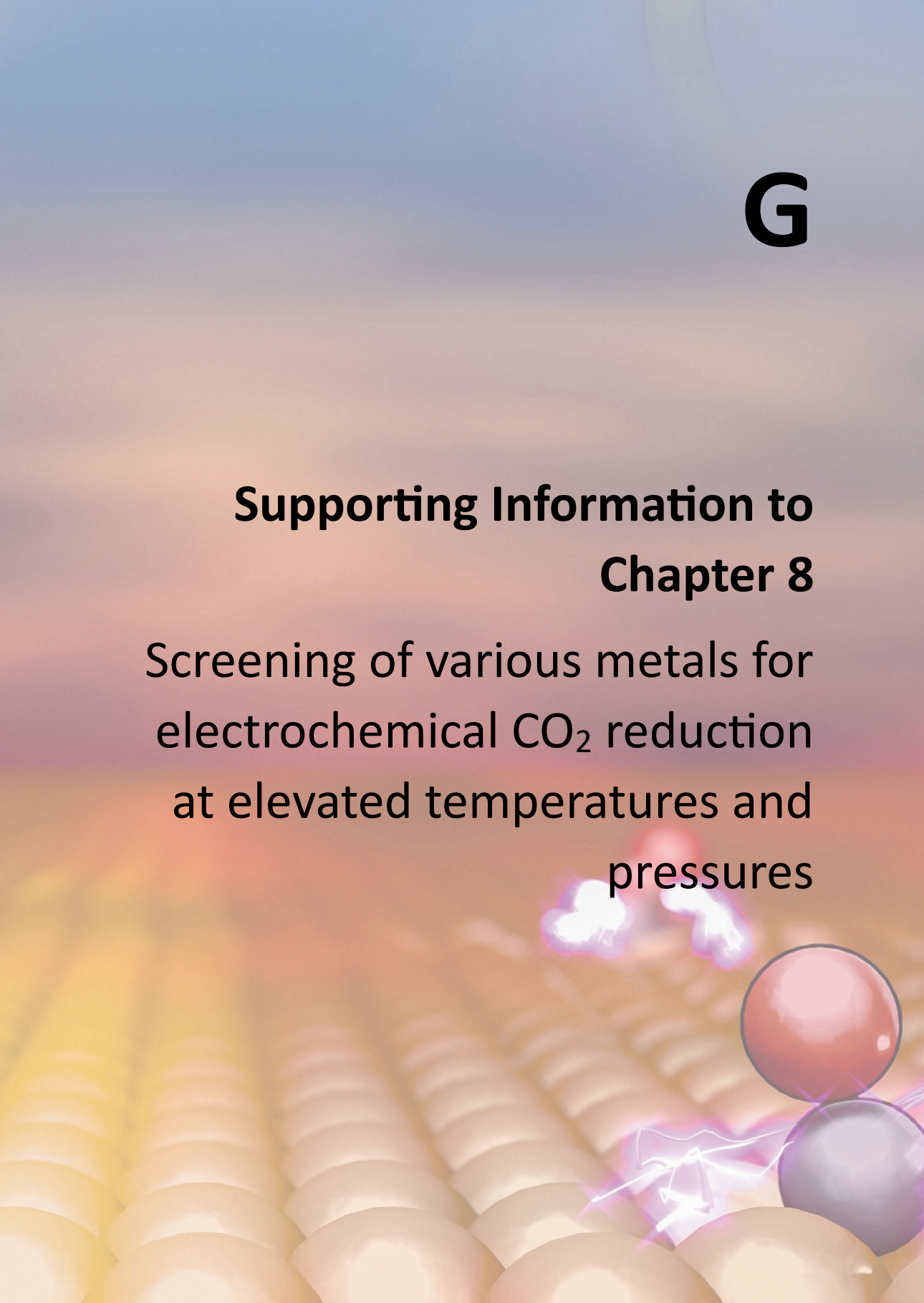


Figure F.17 Faradaic efficiency as function of pressure and electrolyte concentration at room temperature and -1.5 V vs SHE.

G

Supporting Information to Chapter 8

Screening of various metals for electrochemical CO_2 reduction at elevated temperatures and pressures



G.1 Catalyst overview

Table G.1 Overview of metal wires used with suppliers and purity

Metal	Supplier	Purity
Ti	Thermo Fischer	99.99
Zr	Mateck	99
Cr	Mateck	99.95
W	Mateck	99.95
Fe	Mateck	99.99
Ru	Mateck	99.95
Co	Mateck	99.995
Rh (0.5 mm diameter)	Goodfe llow	99.9
Ir	Mateck	99.9
Ni	Mateck	99.99
Pd	Mateck	99.9
Pt	Mateck	99.99
Cu	Mateck	99.99
Ag	Mateck	99.99
Au	Mateck	99.99
Zn	Mateck	99.999
Cd	Mateck	99.999
In	Mateck	99.99
Sn	Mateck	99.9
Pb	Thermo Fischer	99.998

Table G.2 Shift of the Ag/AgCl reference with 0.1 M KCl at different temperatures, compared to SHE(T)

T [°C]	25	50	75	100	125	150
$E^{\mathrm{Ag\|AgCl}}(T)$ [mV]	230.3	214.5	195.9	174.6	151.1	125.5

Table G.3 Overview with some of the highest reported Faradaic Efficiencies towards the CO2RR products in literature for the metals studied in this study. Only metal wires and foils in aqueous electrolyte in an H-cell configuration have been considered as these are comparable to this study.

Catalyst	Product	Efficiency	Conditions	Ref
Ti	HCOOH	4.6%	-1.57 V vs Ag/AgCl, 0.1 M $KHCO_3$, 30 bar	1
Zr	CO	32.5%	-1.73 V vs Ag/AgCl, 0.1 M $KHCO_3$, 30 bar	1
	HCOOH	7.6%	-1.73 V vs Ag/AgCl, 0.1 M $KHCO_3$, 30 bar	1
Cr	CO	11.8%	-1.49 V vs Ag/AgCl, 0.1 M $KHCO_3$, 30 bar	1
	HCOOH	8.2%	-1.49 V vs Ag/AgCl, 0.1 M $KHCO_3$, 30 bar	1
W	HCOOH	31.9%	-1.61 V vs Ag/AgCl, 0.1 M $KHCO_3$, 30 bar	1
Fe	CO	10.0%	-1.63 V vs Ag/AgCl, 0.1 M $KClO_4$, 30 bar	2
	HCOOH	59.6%	-1.61 V vs Ag/AgCl, 0.1 M $KClO_4$, 30 bar	1
	CH4	2.0%	-1.63 V vs Ag/AgCl, 0.1 M $KHCO_3$, 30 bar	1
Ru	MeOH	30.5%	-0.8 V vs SCE, 0.5 M $NaHCO_3$, *RuOx	3
Co	CO	15.8%	-1.54 V vs Ag/AgCl, 0.1 M $KHCO_3$, 30 bar	1
	HCOOH	21.9%	-1.54 V vs Ag/AgCl, 0.1 M $KHCO_3$, 30 bar	1
	CH4	3.1%	-1.54 V vs Ag/AgCl, 0.1 M $KHCO_3$, 30 bar	1
Rh	CO	61.0%	-1.41 V vs Ag/AgCl, 0.1 M $KHCO_3$, 30 bar	1
	HCOOH	19.5%	-1.41 V vs Ag/AgCl, 0.1 M $KHCO_3$, 30 bar	1
Ir	CO	17.5%	-1.55 V vs Ag/AgCl, 0.1 M $KHCO_3$, 30 bar	1
	HCOOH	22.3%	-1.55 V vs Ag/AgCl, 0.1 M $KHCO_3$, 30 bar	1
Ni	CO	33.5%	-1.59 V vs Ag/AgCl, 0.1 M $KHCO_3$, 30 bar	1
	HCOOH	31.3%	-1.59 V vs Ag/AgCl, 0.1 M $KHCO_3$, 30 bar	1
	CH4	1.78%	-1.8 V vs Ag/AgCl, 0.1 M $KHCO_3$, 60 bar	4
Pd	CO	46.1%	-1.56 V vs Ag/AgCl, 0.1 M $KHCO_3$, 30 bar	1
	HCOOH	44.0%	-1.76 V vs Ag/AgCl, 0.1 M $KHCO_3$, 30 bar	1
Pt	CO	6.1%	-1.48 V vs Ag/AgCl, 0.1 M $KHCO_3$, 30 bar	1
	HCOOH	50.4%	-1.48 V vs Ag/AgCl, 0.1 M $KHCO_3$, 30 bar	1
Cu	CO	47.5%	-1.45 V vs Ag/AgCl, 0.1 M $KHCO_3$, 30 bar	5
	HCOOH	53.7%	-1.64 V vs Ag/AgCl, 0.1 M $KHCO_3$, 30 bar	1
	CH4	56.7%	-1.59 V vs Ag/AgCl, 0.1 M $KHCO_3$, 30 bar	5
	C2H4	25.5%	-1.44 V vs NHE, 0.1M $KHCO_3$	6
Ag	CO	81.5%	-1.37V vs NHE, 0.1M $KHCO_3$	6
	HCOOH	20.5%	-2.2V vs SCE, 0.05 M $KHCO_3$, 0 °C	7
Au	CO	87.1%	-1.14V vs NHE, 0.1M $KHCO_3$	6
	HCOOH	11.8%	-1.30 V vs Ag/AgCl, 0.1 M $KHCO_3$, 30 bar	1
Zn	CO	79.4%	-1.54V vs NHE, 0.1M $KHCO_3$	6
	HCOOH	40.5%	-1.70 V vs Ag/AgCl, 0.1 M $KHCO_3$, 30 bar	1
Cd	CO	3.7%	-2.2V vs SCE, 0.05 M $KHCO_3$, 0 °C	7

	HCOOH	55.9%	-2.2V vs SCE, 0.05 M $KHCO_3$, 0 °C	7
In	CO	14.7%	-2.2V vs SCE, 0.05 M $KHCO_3$, 20 °C	7
	HCOOH	94.9%	-1.55V vs NHE, 0.1M $KHCO_3$	6
Sn	CO	8.0 %	-1.39 V vs Ag/AgCl, 0.1 M $KHCO_3$, 30 bar	1
	HCOOH	92.3%	-1.39 V vs Ag/AgCl, 0.1 M $KHCO_3$, 30 bar	1
Pb	HCOOH	97.4%	-1.63V vs NHE, 0.1M $KHCO_3$	6

Table G.2 shows an overview of the highest efficiencies to CO2RR products found in literature at the different metals studied in this study. To keep this table representative of our study, we only included studies which are performed with similar systems. The studies that are included in this table are in aqueous electrolyte with no unusual cation or anions. If we would include more exotic electrolytes, other products could be included, such as 44% FE towards oxalate on Pb in 0.1M NH_4Cl [8] or 95% FE towards CO on Zn with a CTAB cation[9]. All experiments in this table have been performed in H-cell configuration; with GDE setups sometimes better results can be obtained such as 33% FE toward CO, 35% towards CH_4 and 2.3% for ethanol on Pt at 30 bar pressure [10]. Moreover, we only included pure metals wires and foils in this table. So for example alloys, oxides, carbides and phosphides are not included (there are studies in literature producing for example long chain hydrocarbons on phosphate derived Ni[11]). Moreover, we have only reported products with a reported FE above 1% FE. Very minor products such as methanol and methane have been observed on metals as Ag, Au and Zn [12,13]. Also long chain hydrocarbons have been observed before in very small amounts on many metal catalysts [14].

G.2 Focused screening extra data

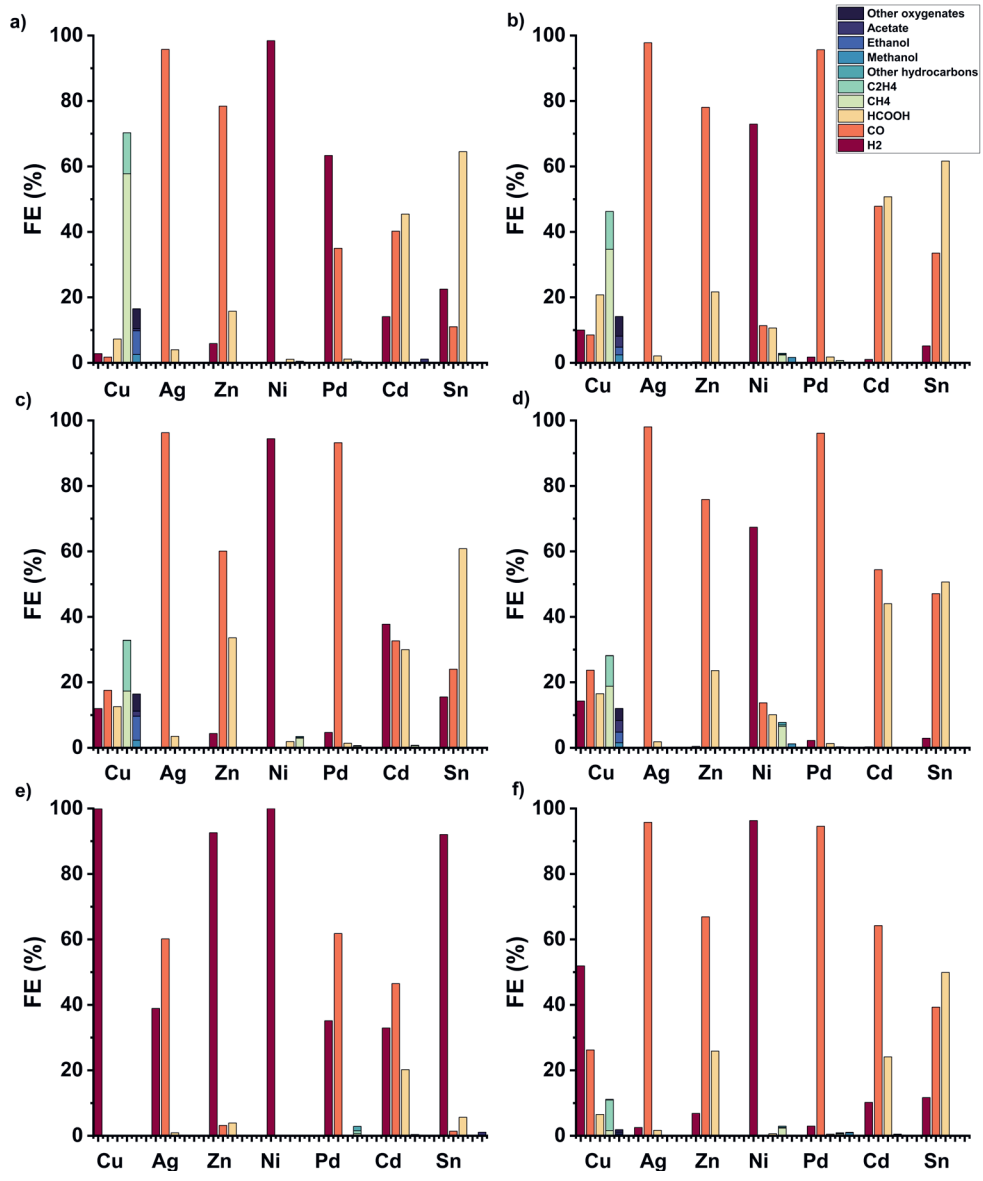


Figure G.1 Faradaic efficiency at six different conditions for Cu, Ag, Zn, Ni, Pd, Cd and Sn at -1.5 V vs SHE in 0.1 M $KHCO_3$ as shown in Figure 1 but categorized per condition a) 25 °C and 1 bar b) 25 °C and 30 bar c) 50 °C and 5 bar d) 50 °C and 30 bar e) 100 °C and 5 bar f) 100 °C and 30 bar

G.3 Broad screening extra data

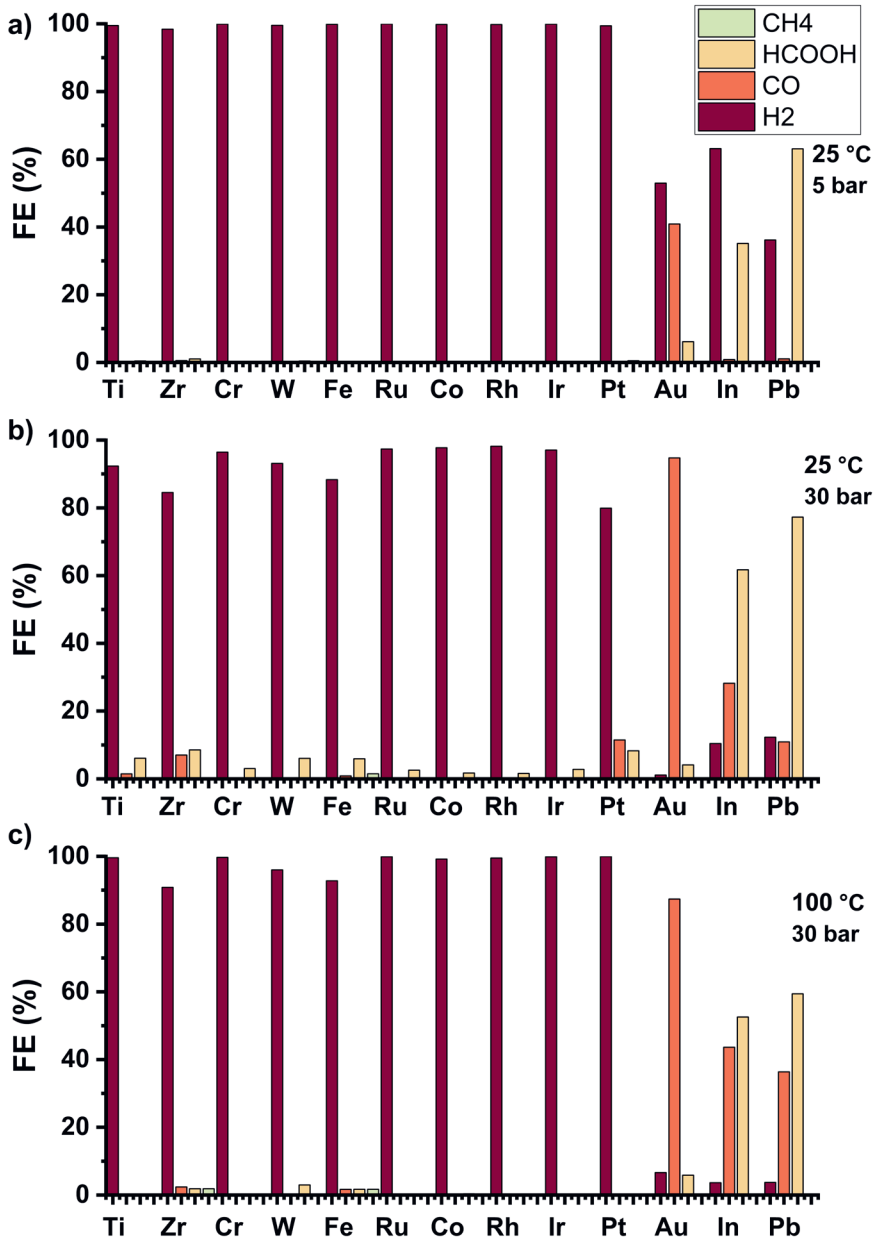


Figure G.2 Faradaic efficiency at the 3 main conditions for a variety of products at -1.5 V vs SHE in 0.1 M $KHCO_3$ as shown in Figure 4 but categorized per condition a) 25 °C and 1 bar b) 25 °C and 30 bar c) 100 °C and 30 bar

G.4 Stability

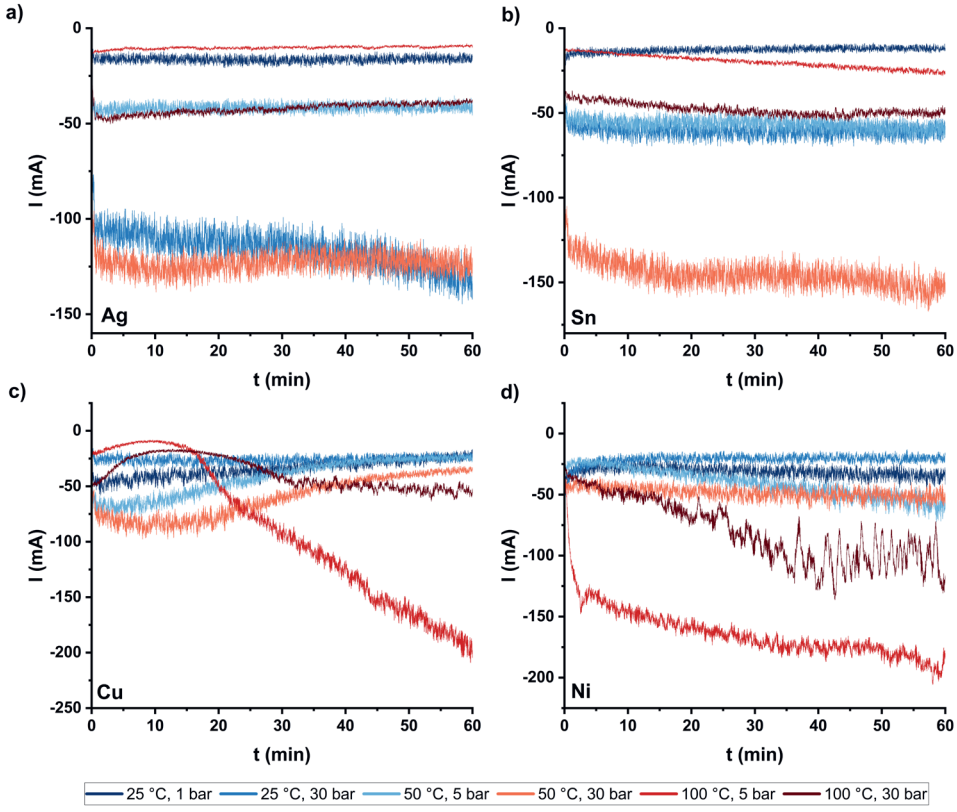


Figure G.3 Current vs time for the different conditions for a) Ag b) Sn c) Cu d) Ni. Higher temperatures lead to more unstable currents, especially on Cu and Ni.

G.5 Comparison to literature

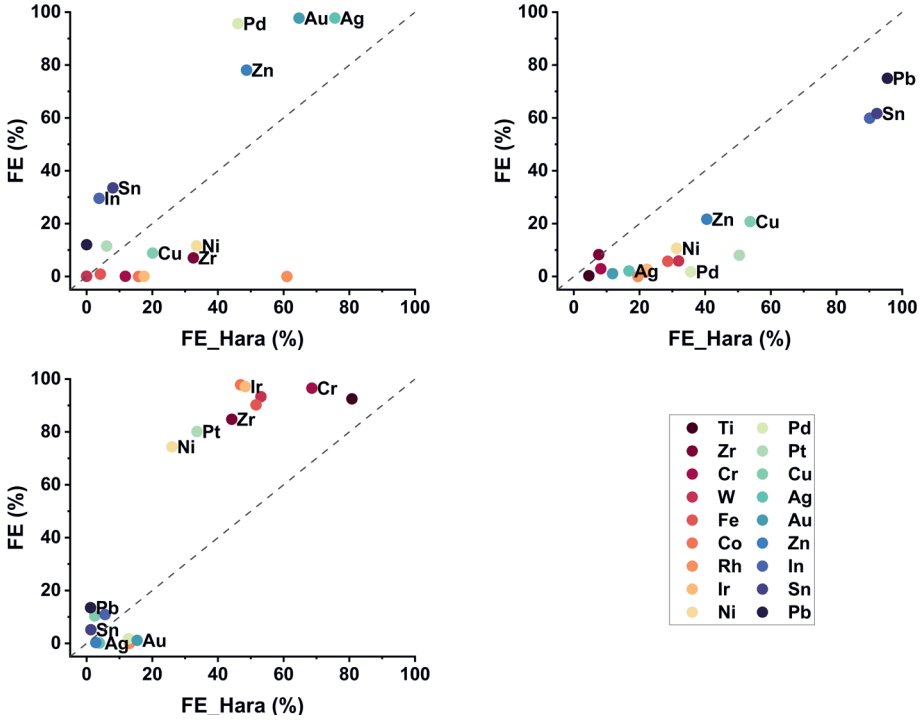


Figure G.4 Comparison of Faradaic efficiency at 30 bar and room temperature between this study and the study of Hara et al.[1] The dotted line shows the same efficiency; above this line, our study has higher efficiencies and below this line, the study of Hara shows higher efficiencies. a) shows the Faradaic efficiency towards CO, b) towards HCOOH and c) towards H_2.

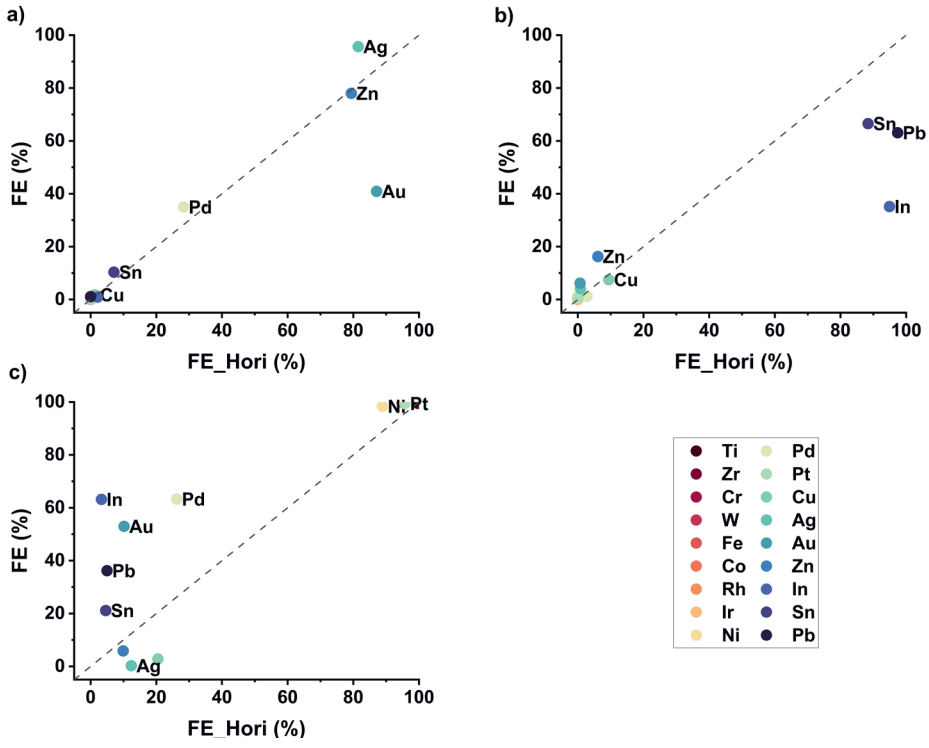


Figure G.5 Comparison of Faradaic efficiency at 1 bar and room temperature between this study and the study of Hori et al.[6] The dotted line shows the same efficiency; above this line, our study shows higher efficiencies, and below this line, the study of Hori shows higher efficiencies. a) shows the Faradaic efficiency towards CO, b) towards HCOOH and c) towards H_2.

G.6 Activity

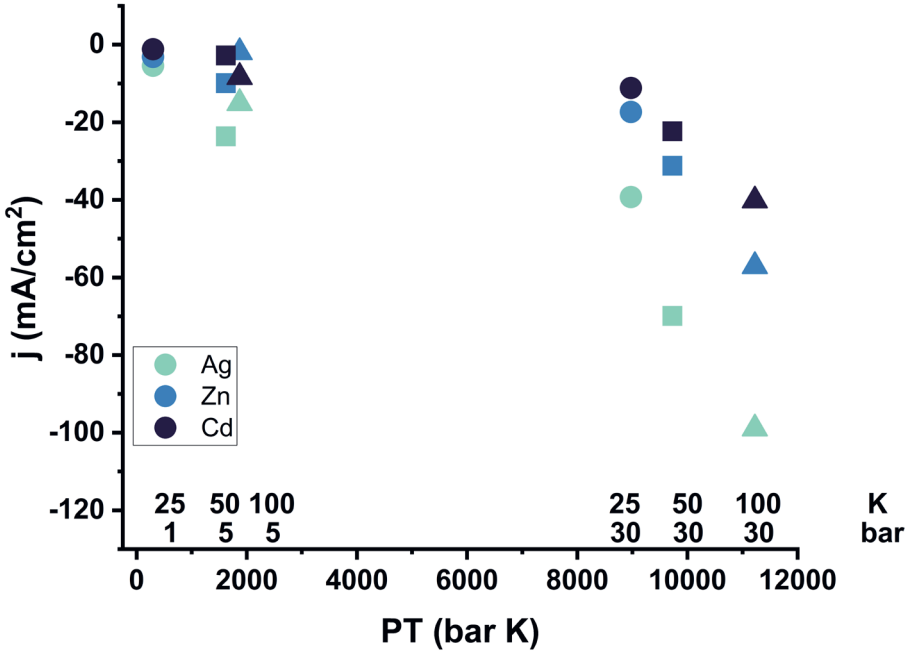


Figure G.6 The partial current density for CO2RR as function of pressure and temperature for Ag, Zn and Cd. Both temperature and pressure increase the CO2RR current density, except when high temperatures are used at low pressures

G.7 Selectivity

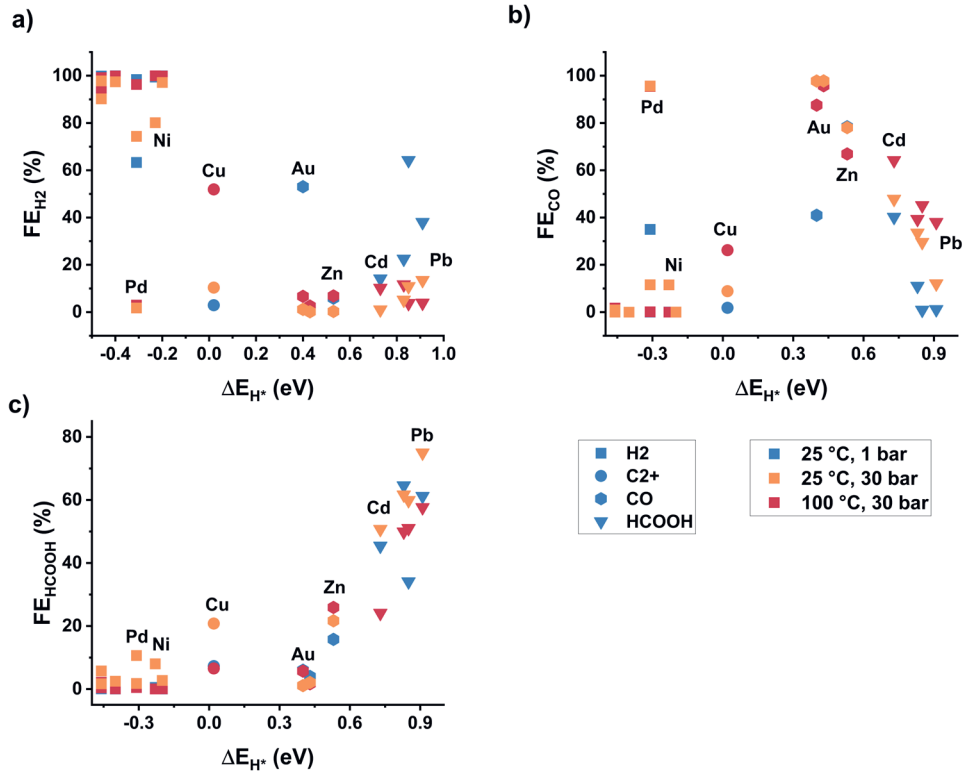


Figure G.7 The Faradaic efficiency at different experimental conditions for all metals tested as function of the binding energy determined by Bagger et al.[15] a) hydrogen b) CO and c) HCOOH. The symbol illustrates to which group the metal is typically classified.

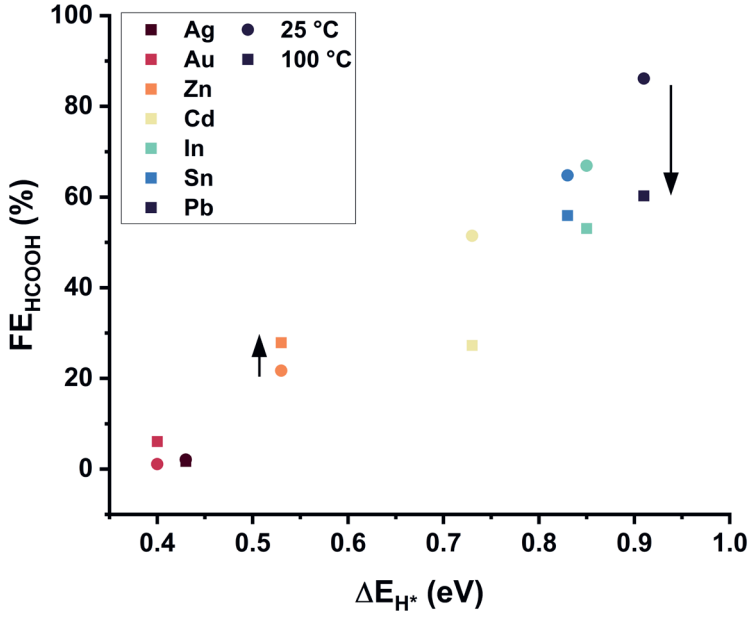


Figure G.8 Trend of formic acid efficiency with increasing temperature at 30 bar plotted vs hydrogen binding energy.

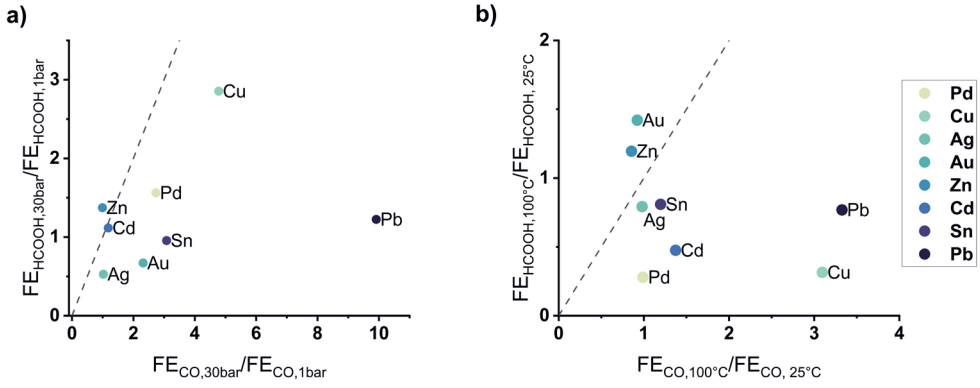


Figure G.9 The ratio between the Faradaic efficiency for HCOOH plotted against the ratio between Faradaic efficiency for CO to illustrate if relatively more CO or HCOOH is produced. The dotted line shows where both CO and HCOOH increase with the same amount; below the line CO increases stronger and above the line HCOOH increases stronger. a) shows the effect of pressure at 25 °C and b shows the effect temperature at 30 bar.

G.8 Hydrocarbon and methanol production

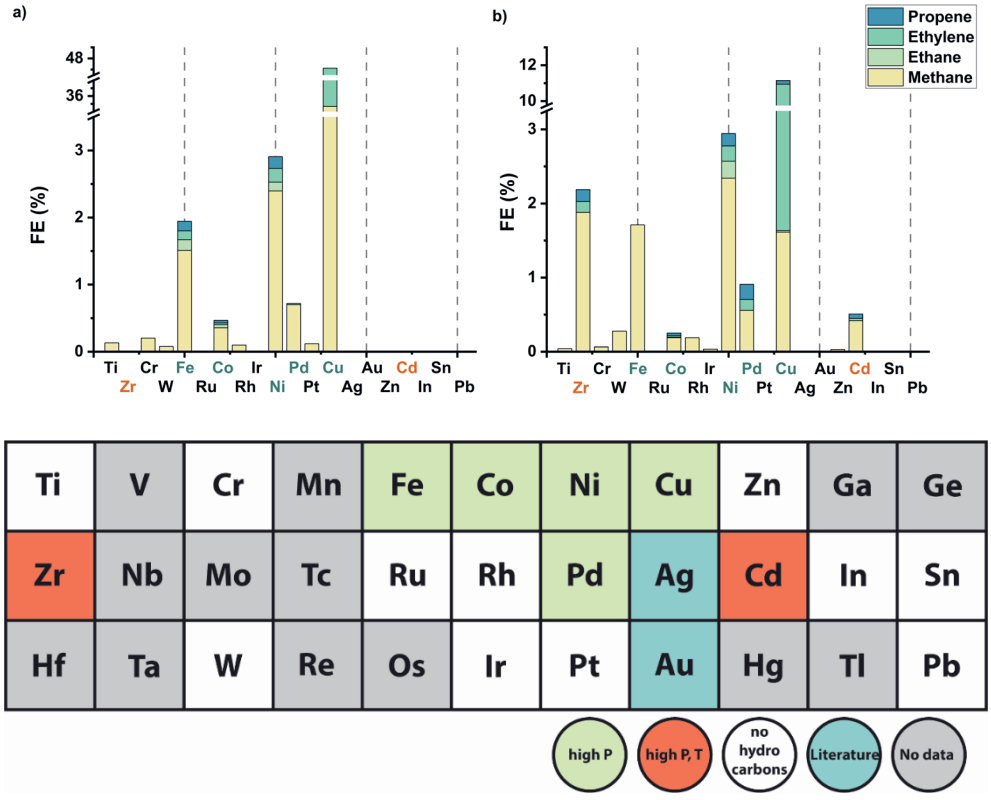


Figure G.10 Hydrocarbon production for all metals studied at a) 30 bar and 25 °C and b) 30 bar and 100 °C. The metals in green can produce longer hydrocarbons already at 25 °C, while the orange metals only produce these at higher temperatures. For the metals in blue hydrocarbons have been found in literature with more than 0.1% FE [14], for the metals in gray no hydrocarbons longer than methane have been observed in this study at – 1.5V vs SHE in 0.1 M $KHCO_3$

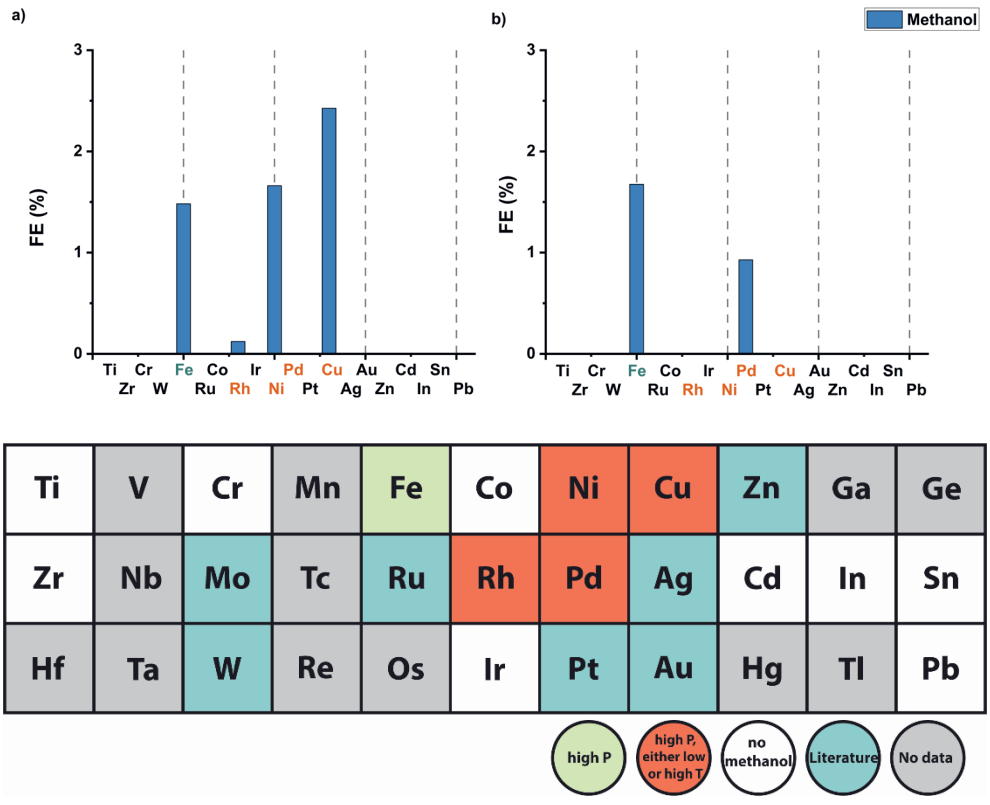


Figure G.11 Methanol production for all metals studied at a) 30 bar and 25 °C and b) 30 bar and 100 °C. The metals in green can produce methanol both at low (25 °C) and high temperature (100 °C), while the orange metals only produce methanol at either high or low temperatures. For the metals in blue methanol has been detected in literature[3,8,13], while in gray no methanol has been detected in this study or in literature.

G.9 How the periodic table in Figure 5 was constructed

For the top figure with the FE of CO2RR vs HER, we looked at the total FE towards CO2RR products and categorized this in 5 different categories. Excellent CO2RR catalysts with efficiencies over 90%, good catalysts with efficiencies between 40 and 90%, intermediate catalysts with efficiencies between 10 and 40%. Poor catalysts with efficiencies lower than 10% and non-active catalysts with efficiencies lower than 1%.

For the bottom figure, we categorized the selectivity towards CO2RR products. If the catalyst was non-active, i.e. less than 1% FE towards CO2RR, we classified it as H_2. Then we look at only the CO2RR products and if the catalyst could produce hydrocarbons over 20% FE (excluding H_2), we categorize it as CH_4. This is to show the unique ability to produce hydrocarbons, where 20% is significant, but also quite the limit without further optimization. The remaining catalysts were categorized in CO or HCOOH depending on their dominant product. However, if the activity towards one of these products was not more than two times larger than the activity towards the other one, we categorized it as mixed products.

References

1. Hara, K., Kudo, A. & Sakata, T. *Journal of Electroanalytical Chemistry* vol. 391 (1995).
2. Hara, K., Kudo, A. & Sakata, T. *Journal of Electroanalytical Chemistry* **386**, 257–260 (1995).
3. Popic, J. P., Avramov, M. L. & Vukovic, N. B. *Journal of Electroanalyticai Chemistry* **421**, 105–110 (1997).
4. Kudo, A., Nakagawa, S., Tsuneta, A. & Sakata, T. *J. Electrochem. Soc* **140**, 1541–1545 (1993).
5. Hara, K., Tsuneto, A., Kudo, A. & Sakata, T. *J Electrochem Soc* **141**, 2097–2103 (1994).
6. Hori, Y., Wakebe, H., Tsukamoto, T. & Koga, O. *Electrochim Acta* **39**, 1833–1839 (1994).
7. Azuma, M., Hashimoto, K., Watanabe, M. & Sakata, T. *Journal of Electroanalytical Chemistry* **294**, 299–303 (1990).
8. Jitaru, M., Lowy, D. A., Toma, M., Toma, B. C. & Oniciu, L. *J Appl Electrochem* **27**, 875–889 (1997).
9. Pan, H., Wang, F., Zhang, Z. & Min, S. *Sustain Energy Fuels* **6**, 2149–2154 (2022).
10. Hara, K., Kudo, A., Sakata, T. & Watanabe, M. *J. Electrochem. Soc.* **42**, L57–L59 (1995).
11. Zhou, Y. *et al. Nat Catal* **5**, 545–554 (2022).
12. Hatsukade, T., Kuhl, K. P., Cave, E. R., Abram, D. N. & Jaramillo, T. F. *Physical Chemistry Chemical Physics* **16**, 13814–13819 (2014).
13. Kuhl, K. P. *et al. J Am Chem Soc* **136**, 14107–14113 (2014).
14. Hwang, S. Y. *et al. Nano Energy* 109881 (2024) doi:10.1016/j.nanoen.2024.109881.
15. Bagger, A., Ju, W., Varela, A. S., Strasser, P. & Rossmeisl, J. *ChemPhysChem* **18**, 3266–3273 (2017).